SYNTHESIS AND CHARACTERIZATIONS OF $YBa_2Cu_3O_{7-\delta}$ SUPERCONDUCTOR WITH ADDED Al_2O_3 NANOPARTICLES VIA CITRATE-NITRATE AUTO-COMBUSTION REACTION

MOHD SHAHADAN BIN MOHD SUAN

THESIS SUBMITTED IN FULFILMENT
OF THE REQUIREMENTS FOR
THE DEGREE OF DOCTOR OF PHILOSOPHY

FACULTY OF ENGINEERING
UNIVERSITY OF MALAYA
KUALA LUMPUR

2014

UNIVERSITI OF MALAYA

ORIGINAL LITERARY WORK DECLARATION

Name of Candidate: Mohd Shahadan Bin Mohd Suan

Registration/ Matrix No.: KHA 100026

Name of Degree: The Degree of Doctor of Philosophy

Title of Project Paper/ Research Report/ Dissertation/ Thesis (“this Work”): Synthesis and characterizations of $YBa_2Cu_3O_{7-\delta}$ superconductor with added Al_2O_3 nanoparticles via citrate-nitrate auto-combustion reaction.

Field of Study: Superconductor Material

I do solemnly and sincerely declare that:

(1) I am the sole author/ writer of this Work;

(2) This work is original;

(3) Any use of any work in which copyright exists was done by way of fair dealing and for permitted purposes and any excerpt or extract from, or reference to or reproduction of any copyright work has been disclosed expressly and sufficiently and the title of the work and its authorship have been acknowledged in this Work;

(4) I do not have any actual knowledge nor do I ought reasonably to know that the making of this work constitutes an infringement of any copyright work;

(5) I hereby assign all and every rights in the copyright to this Work to the University of Malaya (“UM”), who henceforth shall be owner of the copyright in this Work and any reproduction or use in any form or by any means whatsoever is prohibited without the written consent of UM having been first had and obtained;

(6) I am fully aware that if the course of making this Work I have infringed any copyright whether intentionally or otherwise, I may be subject to legal action or any other action as may be determined by UM.

Candidate’s Signature Date

Subscribed and solemnly declared before,

Witness’s Signature Date

Name:

Designation

ABSTRACT

Superconductor materials are renowned to conduct electricity at zero resistance and capable to expel magnetic flux. It can be used in developing efficient wire cables, magnetic energy storage and levitation technologies. Thus, the high temperature superconductor $YBa_2Cu_3O_{7-\delta}$ with added Al_2O_3 nanoparticles was synthesized via citrate-nitrate auto-combustion reaction process. The novelty of this research work is the citrate-nitrate auto-combustion reaction method consumed less energy and time compared with other conventional synthesis methods for processing of composite superconductor oxides and produced well distribution of Al_2O_3 nanoparticles in $YBa_2Cu_3O_{7-\delta}$ superconductor. The auto-combustion reaction transformed the formulated precursor citrate-nitrate gel into very fine ashes. It yielded Al_2O_3 and $YBa_2Cu_3O_{7-\delta}$ phases after calcination process which was further heat treated to achieve superconductivity. The reactions during synthesis processes were investigated through the thermal evaluations. The effects of different concentration of Al_2O_3 nanoparticles on the structure, superconducting, magnetic and mechanical properties of $YBa_2Cu_3O_{7-\delta}$ were investigated and appraised. The sustained orthorhombic structure in each sample contributed to consistency in superconducting transition temperature while the flux pinning forces provided by the non-superconducting nanoparticles improved the critical current density. Furthermore, the mechanical hardness of the samples was also influenced by the addition of nanoparticles. This work shows that the citrate-nitrate auto-combustion reaction is an effective method to introduce Al_2O_3 as nanoparticles homogeneously distributed in the $YBa_2Cu_3O_{7-\delta}$ superconductor.

SINTESIS DAN PENCIRIAN SUPERKONDUKTOR $YBa_2Cu_3O_{7-\delta}$ DITAMBAH ZARAH NANO Al_2O_3 MELALUI TINDAK BALAS PEMBAKARAN - AUTOMATIK SITRAT-NITRAT.

ABSTRAK

Bahan-bahan superkonduktor telah diketahui dapat mengalirkan arus elektrik pada rintangan sifar dan menyingkir fluks magnet. Ia boleh digunakan dalam membangunkan teknologi wayar kabel efisien, penyimpanan tenaga dan pengapungan magnet. Oleh itu, superkonduktor suhu tinggi $YBa_2Cu_3O_{7-\delta}$ terkandung zarah nano Al_2O_3 telah disintesis melalui tindak balas pembakaran-automatik sitrat-nitrat. Keaslian kerja penyelidikan ini ialah kaedah sintesis ini lebih menjimatkan tenaga dan masa berbanding kaedah lama dalam penghasilan komposit superkonduktor oksida dan dapat menghasilkan serakan seragam zarah nano Al_2O_3 dalam superkonduktor $YBa_2Cu_3O_{7-\delta}$. Pembakaran-automatik telah menukarkan gel sitrat-nitrat yang telah diformulasi kepada abu-abu yang sangat halus. Ianya menjadi fasa-fasa Al_2O_3 dan $YBa_2Cu_3O_{7-\delta}$ setelah dikalsin sebelum dirawathaba bagi mencapai kesuperkonduksian. Setiap tindak balas yang berlaku semasa proses sintesis ini diperincikan melalui kaedah penilaian terma. Segala kesan akibat penggunaan kepekatan berbeza zarah nano Al_2O_3 terhadap struktur, sifat kesuperkonduksian, kemagnetan dan sifat mekanikal $YBa_2Cu_3O_{7-\delta}$ dikaji dan ditaksirkan. Struktur ortorombik setiap sampel menyumbang kepada suhu peralihan kesuperkonduksian yang konsisten manakala daya pengepin yang diperolehi daripada zarah nano bukan superkonduktor telah menambahbaik ketumpatan arus genting. Selain itu, kekerasan mekanikal sampel-sampel juga telah terpengaruh dengan penambahan zarah nano ini. Kajian ini menunjukkan bahawa kaedah pembakaran-automatik sitrat-nitrat merupakan kaedah berkesan untuk menghasilkan Al_2O_3 sebagai bahan zarah nano tertabur secara seragam dalam superkonduktor $YBa_2Cu_3O_{7-\delta}$.

ACKNOWLEDGMENT

Foremost I wish to express my sincere appreciation to my supervisor, Dr. Mohd Rafie Johan for his consistent guidance, teaching and supervision during the process of working this research. His advice and comments have helped me significantly in moving forward and completing this thesis report on time. I could not have imagined having better supervisor and mentor during my PhD study.

I would also thank Dr. Yoichi Kamihara from Keio University, Japan for offering me an internship opportunity to work in his research group in Hiyoshi, Japan. This internship program has enlighten me and allowed me to work on diverse exciting project. To my friends in Keio University, you have made my stay in Japan a memorable one.

Besides, I would like to thank my friends in Nanomaterials Group of Advanced Materials lab, Mechanical Engineering of University of Malaya. I thank them for their continuous support and assistance provided whenever I needed a helping hand. A special thanks to Mr. Nazarul Zaman, Mr. Said Sakat and Mrs. Norzirah, a big contribution and assistances from them are very great indeed.

Last but not least, my deepest gratitude goes to my beloved parents, Mohd Suan Tulis and Shariah Dahol and all my siblings, for their endless love and encouragement. I will not be who I am today without their encouragement. Not to forget endless support and understanding from my wife, Vizy Nazira Riazuddin and my little prince, Muhammad Eusoff Muzaffar. To those who indirectly contributed in this research, your kindnesses are highly appreciated. Thank you very much.

TABLE OF CONTENTS

LIST OF FIGURES

LIST OF TABLES

LIST OF SYMBOLS AND ABBREVIATIONS

Symbol	**Description**
a	lattice constant at x direction
A	cross section of the sample
b	lattice constant at y direction
B_a	applied magnetic field
B_C	critical magnetic field
B_i	interior magnetic field
B_r	remnant flux density
c	lattice constant at z direction
c/n	citrate to nitrate ratio
SSP	solid-state processing
$C\mathrm{p}$	heat capacity
CP	co-precipitation
d	grain size
D	thickness of slab
δ	oxygen deficiency
DTA	differential thermal analysis
E	electric field
EDX	energy dispersive X-ray
$\mathrm{E_F}$	fermi energy
emf	electromotive force
FESEM	field emission scanning electron microscope
F_L	Lorentz force

F_n	free energy at normal state
F_p	pinning force
f_p	basic pinning force
F_s	free energy at superconducting state
H (P)	heat required by products
H (R)	heat required by reactants
B_C, H_C	critical magnetic field
$B_\mathrm{C2,}$ H_C2	upper critical applied magnetic field
$\mathrm{H_V}$	Vickers hardness
J_C	critical current density
J_s	density of superconducting current
k_B	Boltzmann’s constant
l	length of superconductor slab
L	Phase transformation entalphy
m	mass of electron
MO	metal oxide
MOH	metal hydroxide
MPMS	magnetic properties measurement system
n_i	stoichiometry ratio of reactants coefficient
n_j	stoichiometry ratio of products coefficient
n_n	number of normal electron
n_o	average number of electrons
N_p	pinning center density
n_s	number of superconducting electron
P_j	products
Φ_o	flux quantum

R	resistance
R_i	reactants
RT	room temperature
SQUIDs	superconducting Quantum Interference Devices
t	width of superconductor slab
T_0	initial temperature
T_ad	adiabatic temperature
T_C	superconductor critical temperature
T_com	combustion temperature
TGA	thermogravimetric Analysis
T_ig	ignition temperature
U_o	flux creep potential
U_p	flux pinning potential
V_f	volume fraction of pinning center
v_s	velocity of superconducting electron
x_mol	concentration of Al_2O_3 nanoparticles in the sample
XRD	X-ray diffraction
YSZ	yttrium stabilized zirconia
$\Delta \mathrm{E}$	energy gap of Cooper pair fluid
ΔH	heat needed for ignition
$\Delta \mathrm{M}$	magnetization gap
$\Delta \mathrm{Q}$	heat loss
λ	penetration depth
μ_r	relative permeability

ξ	superconductors coherence length
ξ_{ab}	coherence length parallel to *a*-*b* plane
ξ_c	coherence length parallel to *c* plane
ξ_o	intrinsic coherence length
ρ	resistivity
σ	conductivity
τ	crystallite size
ψ	superconducting order parameter
κ	Ginzburg-Landau parameter

CHAPTER 1

INTRODUCTION

1.1 Research background

Superconductivity is a promising technology to prevent energy losses attributed from electrical resistivity. This technology attracts much attention to the researches due to two main reasons: the electricity can be conducted at zero resistivity and the magnetic flux can be totally repelled out from the body of superconducting material. Since discovered in 1911, superconductivity was only been found in elements and alloys where the critical temperature (T_C) of these materials are very low (Onnes, 1991). In 1986, the lanthanum cuprate was found to be the first compound material to exhibit superconductivity (Muller and Bednorz, 1986). This breakthrough was followed by discovery of yttrium barium copper oxide ($YBa_2Cu_3O_{7-\delta}$) superconducting compound in 1987 which brought a great excitement within the scientific community because this material can conduct electricity without having resistivity at temperatures above 77 K. This is the temperature at which nitrogen liquefies, thus $YBa_2Cu_3O_{7-\delta}$ changed the perspective of the applications of superconductivity and opened up the possibility for numerous advancements of technologies (Wu et al., 1987).

Categorized as type II superconductor, $YBa_2Cu_3O_{7-\delta}$ shows perfect diamagnetism at below lower critical fields (H_{C1}), allows penetration of quantized magnetic flux (vortex) at higher fields, and loss superconductivity at above higher critical fields (H_{C2}). It means that the coherence of superconducting state is preserved even in the presence of weak currents and magnetic fields below H_{C2}, and makes it practical to be used in stronger magnetic fields compared with conventional superconductors.

1.2 Problems statement

Theoretically, $YBa_2Cu_3O_{7-\delta}$ has excellent ability to carry higher critical current density (J_C) due to having very high H_{C2} compared with H_{C1}. However, when electrical current is flowed in applied magnetic field of $H_{C1} < H < H_{C2}$, the interaction between vortex and current flow results in the motion of vortex due to Lorentz force which can cause energy loss. At this point, only a small density of current limits by J_C is permitted to flow through this superconductor before losing energy. Generally the J_C can be increased if the vortex is prevented from moving. This can be achieved by pinning them with suitable non-superconducting point as known as pinning centre materials. Pinning centre materials in $YBa_2Cu_3O_{7-\delta}$ can be created either by inducing defects through irradiation techniques and chemical doping or by introducing second phase particles having nanometer size. In chemical doping, elements such as calcium (Ca), potassium (K), silver (Ag) and aluminium (Al) are diffused into $YBa_2Cu_3O_{7-\delta}$ structure (Giri et al., 2005, Celebi et al., 2000, Sen et al., 1990 and Zhang et al., 1995). These elements locally modify the crystallinity of the structure and generate defects such as twins, tweed, and inhomogeneous micro-defects to pin the vortices. The J_C can be improved by chemical doping but in return this method may reduce the T_C, since the orthorhombicity of $YBa_2Cu_3O_{7-\delta}$ is being altered; hence, decreased.

Thus for some reasons, introduction of nanoparticles in $YBa_2Cu_3O_{7-\delta}$ has generated a great interest among researchers. This method represents an easy controlled, non-destructive and efficient tool for improving the mechanical, structural and superconducting properties of $YBa_2Cu_3O_{7-\delta}$ compounds. Various nanometer particles; such as, silicon carbide (SiC), zirconia (ZrO_2), yttrium oxide (Y_2O_3), cerium dioxide (CeO_2), tin oxide (SnO_2) and aluminum oxide or Alumina (Al_2O_3) has been reported to add into $YBa_2Cu_3O_{7-\delta}$. All of these nanoparticles were acted as additional pinning centre and resulted in an increase of the J_C in higher magnetic fields (Guo et al., 1999, Zhang and Evetts, 1993, Goswami et al., 2007, Lee et al., 2001, He et al., 2001 and Mellekh et al., 2006). In order to effectively pin the vortices, nanoparticles should possess features including high density or uniform distribution. Nanoparticles having size of 3-10 nm is equal to the coherence length (ξ) of $YBa_2Cu_3O_{7-\delta}$ and able to be located at CuO_2 planes (Moutalibi and M'chirgui, 2007).

Among the added nanoparticles, Al_2O_3 is more attractive to be selected as the pinning centre material in $YBa_2Cu_3O_{7-\delta}$. Beside the capability to pin the vortex motions, Al_2O_3 nanoparticles are also selected due to its availability in nanometer size, easy fabrication route, higher thermal stability, higher density, better hardness and lower cost. In 1987, the effects of Al substitution for yttrium (Y) or copper (Cu) sites in $YBa_2Cu_3O_{7-\delta}$ were accidently found. For long period of high temperature calcination process, the use of alumina crucibles results in the incorporation of Al in crystals having composition of $YBa_2Cu_{3-x}Al_xO_y$. X-ray diffraction (XRD) analysis reveals that such substitution does not lead to changes in the structural symmetry of $YBa_2Cu_3O_{7-\delta}$ but the orthorhombicity of the system is decreased with increasing Al content (Zhang et al., 2005). The value of T_C decreases with increasing Al. This finding was confirmed by Zhang and his colleagues as they purposely added Al_2O_3 powder into $YBa_2Cu_3O_{7-\delta}$ but yet no reports have published regarding the ability of Al_2O_3 particles as pinning centre material. Until Mellekh et al. (2006) revealed that by using the Al_2O_3 nanoparticles with size about 50 nm, the J_C of $YBa_2Cu_3O_{7-\delta}$ was significantly improved. The improvement was due to pinning mechanism provided by the defects and second phase nanoparticles. Then the roles of Al_2O_3 nanoparticles as pinning centre material were further studied by Moutalibi and M'chirgui (2007). They used smaller Al_2O_3 nanoparticles (~10 nm) to achieve ξ of $YBa_2Cu_3O_{7-\delta}$ superconductor. In this case, the J_C was significantly increased in Al_2O_3 nanoparticles added $YBa_2Cu_3O_{7-\delta}$ samples. This was attributed due to the introduction of second phase nanoparticles as pinning centre material. This finding was supported by another study from Albis et al. (2010). In this study it was showed that the failure to distribute Al_2O_3 nanoparticles uniformly in $YBa_2Cu_3O_{7-\delta}$ decreased the effectiveness of this mechanism as well as reduced the T_C.

Nevertheless, imperfections in the superconductor results in quick loss of superconducting state before the ideal J_C can be achieved. Therefore, in this sense, high purity of superconducting materials is required to optimize ideal T_C and J_C. In the last decade, various strategies have been employed to prepare pure single-phase $YBa_2Cu_3O_{7-\delta}$ powder, which can be subsequently processed to yield superconducting specimens. One interesting method can be employed is citrate-nitrate auto-combustion reaction. This method is a combination of combustion reaction with gel processing technique. Combustion reaction is powerful technique to obtain high purity samples since the reaction generates enough heat to volatize all low boiling point impurities. Other advantages of using this reaction are; low processing costs, simple exothermic reaction, and can be used to yield new materials. In the gel processing technique, the reactants were mixed in solution state before complexed using citric acid and heated to form gel. The reactants uniformly disperse in the gel before reacting at high temperature. Thus, combination of these techniques will result in highly pure and well dispersed nanoparticles compound compared with other conventional methods. Bhattacharya et al. (1991) demonstrated that by using citrate-nitrate auto-combustion reaction, highly pure $YBa_2Cu_3O_{7-\delta}$ powder can be yielded. On the other hand, Pathak et al. (2002) successfully synthesized highly pure Al_2O_3 nanoparticles using this same method.

Therefore, in this research works, improvisations of citrate-nitrate auto-combustion reaction were employed to synthesize Al_2O_3 nanoparticles added $YBa_2Cu_3O_{7-\delta}$ superconductor. The Al_2O_3 nanoparticles were uniformly dispersed in highly pure $YBa_2Cu_3O_{7-\delta}$ matrix by a single combustion reaction. In order to achieve ideal combustion reaction, the citrate to nitrate ratio of the gel was optimized. Then different amount of Al_2O_3 nanoparticles were yielded in $YBa_2Cu_3O_{7-\delta}$ matrix by adding varying mole fraction of $Al(NO_3)_3$. The effects of Al_2O_3 nanoparticles on the combustion characteristics, crystal structure, superconducting and mechanical properties of $YBa_2Cu_3O_{7-\delta}$ compound were thoroughly investigated and discussed. Finally, the role of Al_2O_3 nanoparticles as efficient pinning centre material was established evidencing from the increased J_C without any significant lowering of T_C of $YBa_2Cu_3O_{7-\delta}$ superconductor.

1.3 Research objectives

The objectives of this research are summarized below:

i. To synthesize and characterize $YBa_2Cu_3O_{7-\delta}$ superconductor produced by citrate-nitrate auto-combustion reaction with optimum citrate-nitrate ratio.

ii. To synthesize and characterize Al_2O_3 nanoparticles added $YBa_2Cu_3O_{7-\delta}$ superconductor produced by citrate-nitrate auto-combustion reaction with different Al_2O_3 compositions.

iii. To investigate and understand the influence of the distribution of Al_2O_3 nanoparticles on structural and mechanical properties of $YBa_2Cu_3O_{7-\delta}$.

iv. To investigate T_C of the $YBa_2Cu_3O_{7-\delta}$ superconductor though added with of high density of Al_2O_3 nanoparticles.

v. To investigate critical current density (J_C) of the $YBa_2Cu_3O_{7-\delta}$ superconductor by introduction of Al_2O_3 nanoparticles as pinning centre material.

1.4 Scope of the works

This research work scopes are synthesizing and characterizing $YBa_2Cu_3O_{7-\delta}$ and Al_2O_3 nanoparticles added $YBa_2Cu_3O_{7-\delta}$ superconductors produced by citrate-nitrate auto-combustion reaction. Two important parameters were verified during synthesizing: citrate-nitrate ratio (c/n) and Al_2O_3 compositions. The combustion reaction of the samples was evaluated by analyzing the thermal behaviour of as-prepared gels at increasing temperature. The structural properties of the synthesized samples; such as, lattice constants, orthorhombicity, crystallite size, elements, morphology and microstructure were characterized using multiple techniques to investigate the effects of each parameter. The superconductivity responses such as resistivity and T_C were evaluated for both un-added and Al_2O_3 added samples as comparison. Special attention was given on the effects of Al_2O_3 nanoparticles in $YBa_2Cu_3O_{7-\delta}$ superconductor. The hardness of this composite superconductor was assessed by Vickers microhardness. While the magnetic responses such as hysteresis and J_C of the superconductors were investigated at two different temperatures: 50 and 77 K in purposes to obtain clear effects of Al_2O_3 nanoparticles as pinning center materials in $YBa_2Cu_3O_{7-\delta}$ superconductor.

1.5 Significant of research

This research presents a novel method for synthesizing composite superconductors. The citrate-nitrate auto-combustion reaction consumed less energy and time compared with other conventional synthesis methods for processing of composite superconductor oxides. This technique produced better distribution of second phase nanoparticles in a highly pure superconductor matrix by a single step reaction. As consequences, the superconducting, magnetic, and mechanical properties of $YBa_2Cu_3O_{7-\delta}$ superconductor were increased. Well distributed Al_2O_3 nanoparticles were found functionalized as pinning centre materials in $YBa_2Cu_3O_{7-\delta}$ superconductor. It was realised that well distribution Al_2O_3 nanoparticles increases the J_C with minimum effects towards T_C. This enhancement provides opportunities to $YBa_2Cu_3O_{7-\delta}$ superconductor to be operated above 77 K in real applications.

CHAPTER 2

LITERATURE REVIEW

2.0 Superconductivity

Superconductivity is phenomenon at which electricity can flow without resistivity. In 1911, the research community was astonished by this new scientific discovery of Onnes when he found that the resistivity of mercury (Hg) rapidly reduced to zero once the temperature was brought down to 4.19 K in presence of liquid helium (He) (Onnes, 1911). In 1933, Meissner and Oschenfeld found another identical characteristic of superconductivity which differentiates it from perfect conductivity (Meissner and Oschenfeld, 1933). The second characteristic of superconductivity is perfect diamagnetism at which the magnetic induction, (B) of the superconducting material has to be zero. At superconductivity, the internal magnetic flux is expelled out while external magnetic flux is prevented to penetrate in the body of the material; hence, generate levitation. This phenomenon is known as the Meissner's effect. Since the discovery of superconductivity, it has been found in many elements and alloys such as lead (Pb), niobium (Nb), aluminium (Al), NbN and Nb_3Sn. In all cases these conventional superconductors achieved superconductivity at extremely low temperature and requires liquid He as their coolant. Therefore, many researchers conducted investigation to find new type of superconducting materials which are able to be operated at higher temperature. In 1986, Bednorz and Muller initiated this breakthrough by discovering copper based superconducting materials (Bednorz and Muller, 1986). The La-(Sr,Ba)-CuO was found to show superconductivity at 30 K. Based on this finding Wu and colleagues discovered the first material to show superconductivity at above 77 K which is the boiling temperature of liquid nitrogen (Wu et al., 1987). The $YBa_2Cu_3O_{7-\delta}$ was found to achieve superconductivity at about 92 K. This achievement has opened the possibilities for the new applications of superconductor at relatively lower cost. As consequences, many other superconductors have been discovered to have higher superconducting transition temperature or critical temperature (T_C). Figure 2.1 shows yearly change of T_C.

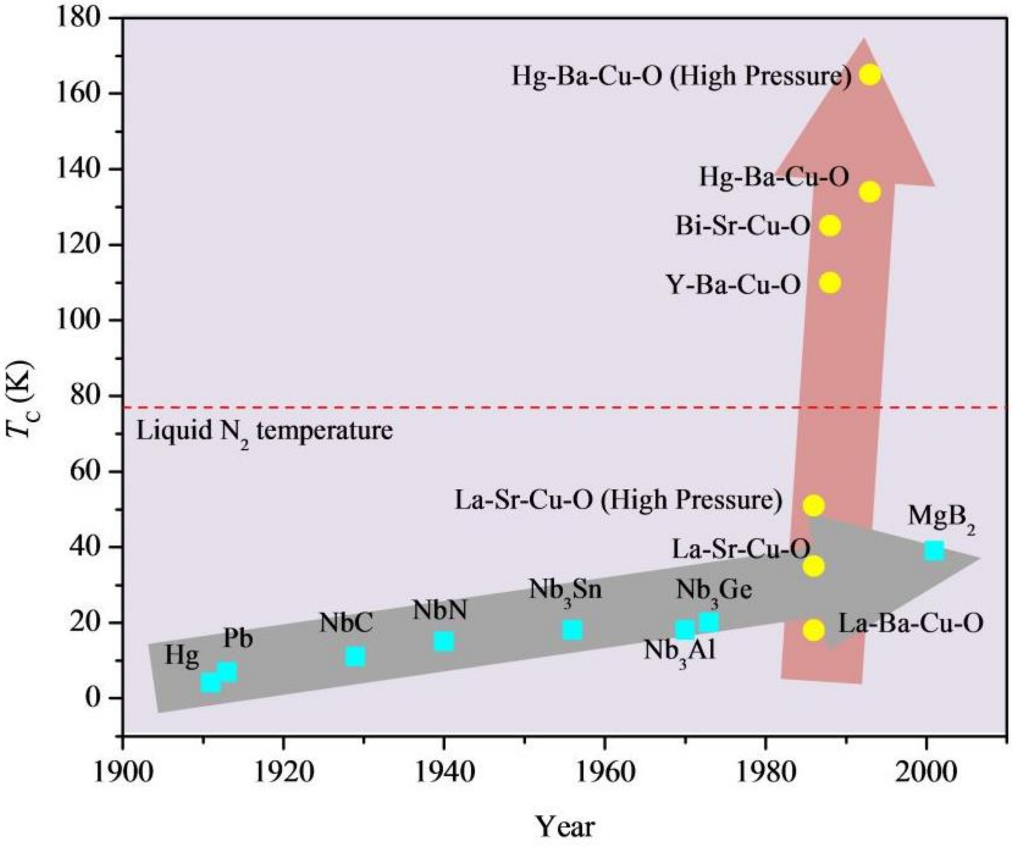

Figure 2.1: Progress of T_C according to year discovered (Roslan, 2004).

2.1 Zero resistivity of superconductors

In a normal conductor, an electrical current may be visualized as a fluid of electrons moving across the ionic lattice. The electrons are constantly colliding with ions in the lattice, and during each collision some part of the energy carried by the electron is absorbed by the lattice. This absorbed energy is converted into heat which is essentially the vibrational kinetic energy of the lattice ions. This is the phenomenon of electrical resistivity suggested by Ohm’s law. As a result, the energy carried by the electrical current is constantly being dissipated. However, the situation is different in a superconductor. In a conventional superconductor, the electronic fluid cannot be resolved into individual electrons; instead it is consisted of bound pairs of electrons. This theory is commonly known as BCS theory as referred to its founders Bardeen, Cooper and Schrieffer (Bardeen et al., 1957). This pairing is caused by an attractive force between electrons due to the exchange of phonons. At superconductivity, the positively charged lattice is attracted to the first passed through electron; hence, distorted. This distortion creates a region of positive net which draw the second electron passes through the same path. The distance between electrons in Cooper pair is known as coherence length, ξ. According to quantum mechanics, the spectrum of this Cooper pair fluid possesses an energy *gap*, meaning there is a minimum amount of energy, ΔE that must be supplied in order to excite the fluid. The ΔE can be related to temperature by Equation (2.1) (Deutscher and Bok, 1993).

$$2\Delta E = 3.5k_B T_C \tag{2.1}$$

Where, k_B is Boltzmann's constant and T is the temperature. Therefore, if ΔE is larger than the thermal energy of the lattice, the Cooper pair fluid will not be scattered by the lattice. The Cooper pair fluid is thus a superfluid, meaning that it can flow without energy dissipation. In other words, at below T_C, the resistivity of superconductors is exactly zero.

2.2 Perfect diamagnetism

Perfect diamagnetism or Meissner effect in superconducting materials is limited by critical magnetic field, B_C. Based on two assumptions, below B_C, the materials remain superconducting with B=0. First, the relative permeability (μ_r) of superconductor is zero and second, the interior field (B_i) generated from surface current has the same magnitude with applied field (B_a) and thus canceled each other. However, once the applied magnetic field is larger than B_C, the magnetic fluxes entirely penetrates into the materials when $\mu_r > 0$ and $B_i < -B_a$; hence, the superconductivity of the material is destroyed and experienced normal resistive phase. B_C is related to the temperature as shown in Equation (2.2) (Krabbes, 2006)

$$B_c(T) = B_c(0)\left[1 - \left(\frac{T}{T_c}\right)^2\right] \tag{2.2}$$

Where, B_C (0) is the critical field at absolute zero temperature. This equation yielded parabolic shaped graph as shown in Figure 2.2.

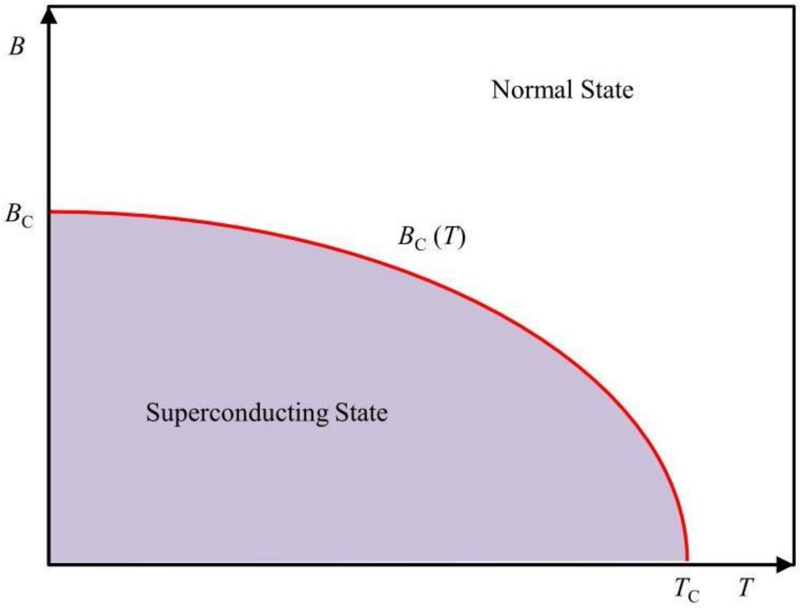

Figure 2.2: Temperature dependence B_C relation depicts boundary that separate between superconducting and normal state.

The superconducting state in all superconductors are totally destroyed at above B_C and approved not fully relevant by Abrikosov in 1957 (Krabbes, 2006). He found that in certain types of superconductors, the transition from superconducting state to normal state is gradual though applied magnetic field is above the B_C. This so called type II superconductors totally loss their superconductivity only at higher upper critical magnetic field, B_{C2}. Therefore, the superconductor which abruptly loss its superconductivity as it surpass the B_C is classed as type I superconductor.

In present, type II superconductors are more interesting since they have two critical fields, B_{C1} and B_{C2} where the upper one can be huge, even hundreds of Teslas (Krabbes, 2006). The temperature dependence of both superconductors is similar to B_C as shown in Equation (2.2); hence, a graph is yielded in Figure 2.3.

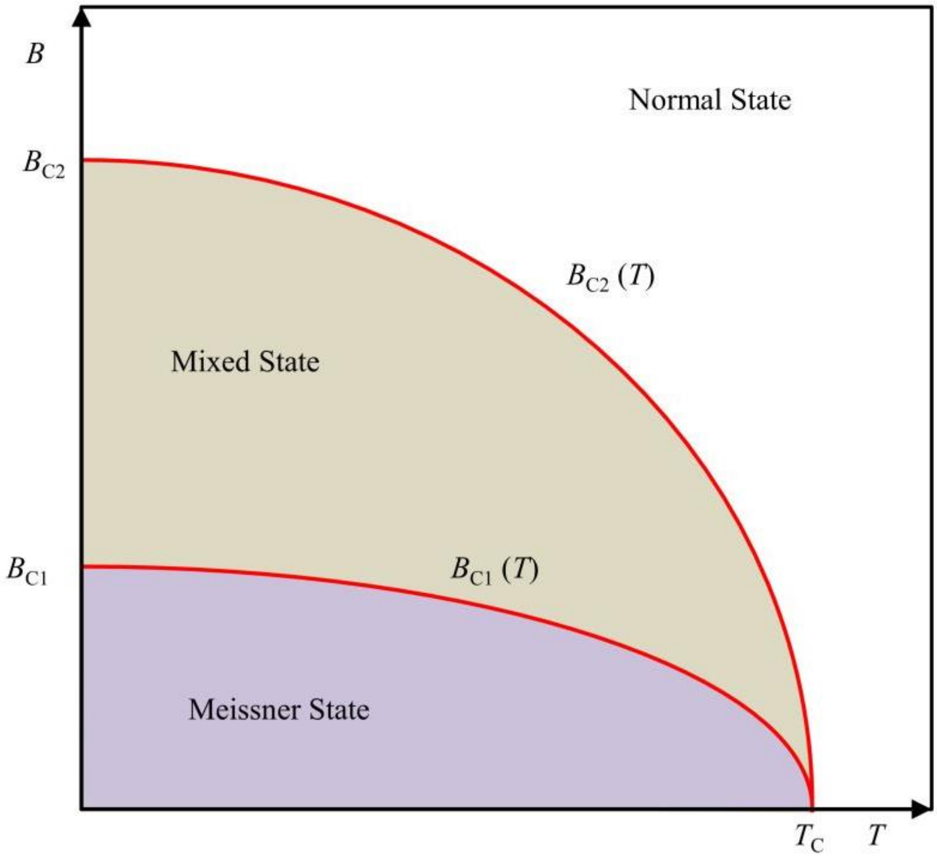

Figure 2.3: Temperature dependence B_{C1} and B_{C2} of type II superconductor.

Below B_{C1}, in the Meissner-state no magnetic field exists inside the superconductor. Between B_{C1} and B_{C2} is so called mixed state, where magnetic field can penetrate into the superconducting material by forming vortices, which have a constant value of magnetic flux. The material remains superconducting though infiltrated by the magnetic vortices. Only above B_{C2}, the superconductivity of the material is vanished.

2.3 Phenomenological theory

2.3.1 London penetration depth

In real cases, the magnetic field actually can penetrate a small length on the surface of the superconductor. When a superconductor is placed inside a weak external magnetic field H**,** the field penetrates for only a short distance of λ, called the penetration depth**,** after which it decays rapidly to zero (London, 1935). It can be easily derived from Maxwell's equations which give the relation between B and current density, J as shown in Equation below

$$\nabla \times B = \mu_0 J \tag{2.3}$$

Where, μ_0 is permeability of vacuum. In superconducting state the interior magnetic field, $\nabla \times B$ are totally zero and J; therefore, must be zero. Outside the material, $B \neq 0$ thus the J will be infinite which is not physically possible. Because of that, the current is assumed to flow on the surface of the material by certain λ, where the value is dependent on the types of superconductor.

London theory can be explained to predict the λ value (London, 1935). In this theory, the average number of electrons per unit volume (n_o) is assumed as the combination of the normal electrons (n_n) and superconducting electrons (n_s). Hence,

$$n_o = n_n + n \tag{2.4}$$

By applying a constant electric field, superconducting electrons are accelerated:

$$m\frac{dv_s}{dt} = -eE \tag{2.5}$$

Where v_s is the velocity of superconducting electrons, m is the mass of electron and E is the electric field. The density of superconducting current can be written as:

$$J_s = -en_s v_s \tag{2.6}$$

Then, the first London equation can be derived from Equations (2.5) and (2.6) to be as:

$$\frac{dJ_s}{dt} = \frac{n_s e^2}{m}E \tag{2.7}$$

Operating with curl (∇) on the both sides:

$$\nabla \times \frac{dJ_s}{dt} = \frac{n_s e^2}{m}\nabla \times E \tag{2.8}$$

By using the Maxwell equation:

$$\nabla \times E = -\frac{\partial B}{\partial t} \tag{2.9}$$

Equation (2.8) can be written as

$$\nabla \times \frac{dJ_s}{dt} = -\frac{n_s e^2}{m}\frac{\partial B}{\partial t} \tag{2.10}$$

By integrating Equation (2.10) with respect to time and considering the Meissner effect, the integration constant can be regarded to be zero and the second London equation can be written as:

$$\nabla \times J_s = \frac{n_s e^2}{m} B \tag{2.11}$$

By using Maxwell Equation (2.3) and considering $J = J_s$, the Meissner effect can be derived from the second London equation as:

$$\nabla \times \nabla \times B = \mu_o \nabla \times J_s \tag{2.12}$$

Equation (2.12) can be written as:

$$\nabla(\nabla \cdot B) - \nabla^2 B = \mu_o \nabla \times J_s \tag{2.13}$$

Hence, $\nabla \cdot B$ is zero inside the superconductor; thus, the equation is simplified as:

$$\nabla^2 B = \mu_o \nabla \times J_s \tag{2.14}$$

By using Equation (2.11), Equation (2.14) can be written as:

$$\nabla^2 B = \frac{1}{\lambda_L^2} B \tag{2.15}$$

Where, λ_L is London penetration depth which defined as:

$$\lambda_L = \left(\frac{m}{\mu_o n_s e^2}\right)^{1/2} \tag{2.16}$$

It can be also is written as:

$$B(x) = B(0) exp\left(-\frac{x}{\lambda_L}\right) \tag{2.17}$$

Where, it is used in the case of semi-infinite superconductor. This equation shown as a graph in Figure 2.4 and proves that B penetrates with just λ_L into the superconductor before it totally decays.

At $T \sim T_C$, λ_L becomes larger. The relation between temperature and λ_L can be written as:

$$\left[\frac{\lambda_L(0)}{\lambda_L(T)}\right]^2 = \left[1 - \left(\frac{T}{T_C}\right)^4\right] \tag{2.18}$$

While the density of n_s with regards of temperature can be written as:

$$n_s = n_o\left[1-\left(\frac{T}{T_C}\right)^4\right] \tag{2.19}$$

Thus, once the temperature achieves the T_C of superconductor, n_o is dominated by n_n because the n_s decreases.

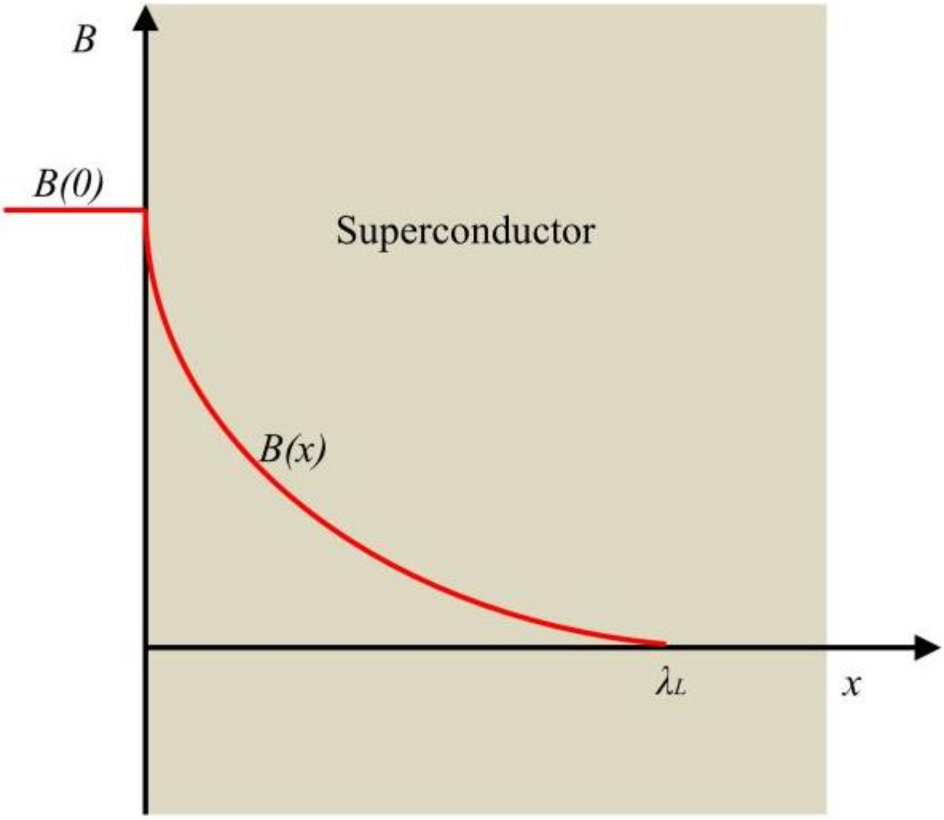

Figure 2.4: Penetration of magnetic field into superconductor, $B(x)$ as determined from Equation (2.16). The B (0) is the field on the surface of superconductor. After the λ_L of superconductor, B no longer exists.

2.3.2 Pippard's non local theory

The non-local theory proposed by Pippard suggested that the change in magnetic potential of superconductors is experienced by superconducting carriers within the penetration depth (Tinkham, 1957). In this theory, Pippard counted the intrinsic coherence length (ξ_o) in prediction of effective penetration depth in terms of London equation as follows:

$$\lambda = \lambda_L \left(\frac{\xi_o}{\xi}\right)^{1/2} \tag{2.20}$$

This equation is in well agreement with experimental results since it is frequently greater if estimated using London's theory. In other words, Pippard overcame the unavailability of the London's theory to predict the penetration depth at non-local condition.

2.3.3 Ginzburg-Landau theory

In presence of magnetic field, the free energy of superconductor expressed in Ginzburg-Landau theory (Cyrot, 1973) can be written as:

$$F_s = F_n + \left[\alpha(T)|\psi|^2 + \frac{\beta}{2}|\psi|^4 + \frac{1}{2m^*}|-i\hbar\nabla\psi + 2e\vec{V}\psi|^2 + \frac{(B)^2}{2\mu_o}\right] \tag{2.21}$$

Where, $\psi = |\psi|e^{i\varphi}$ is the complex order parameter, $\vec{V}$ is vector potential, B is magnetic field, m^* is $2m_e$. Again, from the microscopy theory (Bardeen et al., 1957), Aranson and Kramer (2002) suggested:

$$\alpha = 1.83 \frac{\hbar^2}{2m^*} \frac{1}{{\xi_o}^2} \frac{T - T_c}{T_c} \tag{2.22 (a)}$$

$$\beta = 0.35 \frac{1}{N(0)} \frac{\hbar^2}{2m^*} \frac{1}{{\xi_o}^2} \frac{1}{kT_c} \tag{2.22 (b)}$$

Where, $N(0)$ is the density of states at E_F and ξ_o is the intrinsic coherence length.

Equation (2.21) generates two equations by minimizing the equation with respect to ψ and $\vec{V}$ as:

$$\frac{1}{\mu_o}\left[-\nabla \times (\nabla \times \vec{V})\right] - \frac{ie\hbar}{m^*}[\nabla^*\nabla\psi - (\nabla\psi^*)\psi] - \frac{4e^2}{m^*}\vec{V}|\psi|^2 = 0 \tag{2.23}$$

And

$$\alpha|\psi| + \beta|\psi|^2\psi + \frac{1}{2m^*}| - i\hbar\nabla + 2e\vec{V}|^2\psi = 0 \tag{2.24}$$

For $\vec{V}$=0 and J = 0, Equation (2.24) can be written as:

$$\alpha|\psi| + \beta|\psi|^2\psi + \frac{\hbar^2}{2m^*}\frac{d^2\psi}{dx^2} = 0 \tag{2.25}$$

Where,

$$\left(\frac{\hbar^2}{2m^*\alpha(T)}\right)^{1/2} = \xi(T) \tag{2.26}$$

If the spatial variations of ψ are neglected, the penetration depth can be obtained from Equation (2.23) as:

$$\lambda(T) = \left(\frac{m^{*}\beta}{4\mu_o e^2 \alpha(T)}\right)^{1/2} \tag{2.27}$$

Here, Ginzburg-Landau parameter κ can be obtained as

$$\kappa = \frac{\lambda}{\xi} = \frac{2\pi}{\Phi_0}\sqrt{2}H_c\lambda^2 \tag{2.28}$$

Where, $\Phi_0 = h/2e$ is the flux quantum. If $\kappa < 1/\sqrt{2}$, the superconductivity occurs below H_C and Meissner state is formed; hence, repels the flux. When $\kappa > 1/\sqrt{2}$, superconductivity occurs above H_C; hence, Meissner state is energetically unfavorable and allows vortex phase penetration. Based on the Ginzburg-Landau parameter, κ, superconductor can be classified into two types which are:

$\kappa < 1/\sqrt{2}$ type I

$\kappa > 1/\sqrt{2}$ type II

The classification of superconductors is made by Abrikosov (1957) where the existence of lower critical field, B_{C1} and upper critical field, B_{C2} for $\kappa \geq 1/\sqrt{2}$ was established. These critical fields can be determined as:

$$B_{c1} = \mu_0 H_{c1} = \frac{\Phi_0}{4\pi\lambda^2}\ln\kappa \tag{2.29}$$

And

$$B_{c2} = \mu_0 H_{c2} = \frac{\Phi_0}{2\pi\xi^2} \tag{2.30}$$

The theory limits by local theory which fails at higher frequencies and at temperatures away from T_C. At temperature near T_C the theory, $\lambda > \xi$ becomes valid; hence, Ginzburg-Landau theory suggests that the type II is better than type I superconductor.

2.4 Type II superconductor

2.4.1 Critical current density (J_C)

Critical current density (J_C) is the maximum current that can flow through cross section (A) of superconductor before superconductivity is destroyed. In type II superconductor, magnetic flux is allowed to penetrate the body between B_{C1} and B_{C2}. The flux or vortex is not superconducting at the interior and surrounded by magnetic field. As the magnetic field and the number of vortices are increased, the vortices are aligned hexagonally in case of no pinning, since the vortices are repelled by each other. The phase is called as vortex lattice (Krabbes, 2006). The vortex interacts with the current flow through Lorentz law. The interaction between vortex and current determines J_C in the type II superconductor. Once the current density J is applied, the vortices are started to move, due to the Lorentz-force $F_L = J \times B$ (Dew-Hughes, 2001).

The movement of vortices creates electric field E; thus, dissipates energy, $E \times J$ which is seen as a resistance and the zero resistivity superconducting state is vanished. In order to increase J_C in type II superconductor, vortex must be pinned from moving. The average pinning force, F_P is required so that $F_P > F_L$. Hence, no vortex flow and superconducting current persists as shown $J_C \times B$ (Dew-Hughes, 2001). At absolute zero temperature, when $J < J_C$, current can be flown without energy loss. However when $J > J_C$, the current flow leads to energy loss.

At relatively high temperature and high magnetic field though $F_L = 0$ ($J < J_C$), the thermal fluctuation or flux creep causes the lattice to melt and the lattice order is lost. This phase is called vortex liquid. In this case, the flux creep activation energy ratio, U_0 (T, B) / k_B for type II superconductor reaches towards T_C. Thus the flux creep plays major role in determining J_C. In ideal condition, J_C is only determined by pair breaking current, which is strong enough to break the electron pair with binding energy of 2ΔE. Once the current is started to flow, the free energy of superconducting state is increased by 1/2 $(n_s m v^2)$; where, n_s is density of superconducting electron, m is the mass and v is the velocity of electron (Dew-Hughes, 2001). Superconducting properties vanish when energy gain is equal energy condensate as:

$$\frac{1}{2}n_s m v^2 = \frac{1}{2}m\lambda^2 {J_C}^2 = \frac{1}{2}\mu_0 H_C^2 \tag{2.31}$$

Equation (2.31) predicts that at the ideal condition, J_C is H_C/λ. But imperfections in the superconductor results in quick loss of superconducting state before the ideal J_C can be achieved. In this sense, high purity of superconducting materials is required to achieve ideal J_C value.

2.4.2 Flux pinning

Generally, some pinning sites are naturally present in superconductor, and these pin the vortices with pinning force of F_p. Such pinning sites are point like defects. The F_P of a single point like pinning site is rather small, but a vortex can be adjusted within a network of point-like pins to gain pinning force to overcome F_P with expense of elastic energy (Matsushita, 2007). However, they trap only a fraction of the vortex. Therefore, they are considered weak pinning sites. In order to increase F_P, suitable impurities can be added into the pure superconductor matrix to act as pinning centre. The vortices will be pinned from moving as the free energy of fluxoid is lowered by the interaction with the pinning centres with relation:

$$U_P = \frac{1}{2}\mu_0 H_C^2 \pi \xi^2 d \tag{2.32}$$

Where, $\frac{1}{2}\mu_0 H_C^2$ is the condensation energy per unit volume, d is the size of non-superconducting region and $\pi\xi^2 d$ is the volume of interaction. The basic pinning force, f_P produce by this interaction can be written as:

$$f_P = U_P / \xi \tag{2.33}$$

Thus the total pinning force, F_P is the sum of all f_p in the superconductor (Murakami et al., 1992). Energy exchanged at the interface of the grain for the superconductor having large grains. The number of fluxoid pinned by each grain of size d_g is d_g / a_o. The F_P is related with density of pinning centre material (N_P) with the relation as follows:

$$F_P = N_P \frac{d_g}{a_0} f_P \tag{2.34}$$

Hence using Equation (2.34), J_C can be determined by using:

$$J_C = \frac{N_P d^2 B_C^2 \xi}{2\mu_0(\phi_0 B)^{1/2}} = \frac{\left(\frac{V_f}{d}\right) B_C^2 \xi}{2\mu_0(\phi_0 B)^{1/2}} \tag{2.35}$$

Where $V_f = N_P d_g^3$ is the volume fraction of pinning centre materials. This shows that the J_C is directly proportional to V_f / d in a constant field of B.

2.4.3 Bean model

J_C can be determined using the Bean model from magnetic hysteresis loop (Bean, 1964). Bean suggested that the hard superconductor can carry limited superconducting current density (J_C) which flows locally if induced by any electromotive force, *emf*. Figure 2.5 shows the magnetization of a slab in a parallel field to its surface of thickness D.

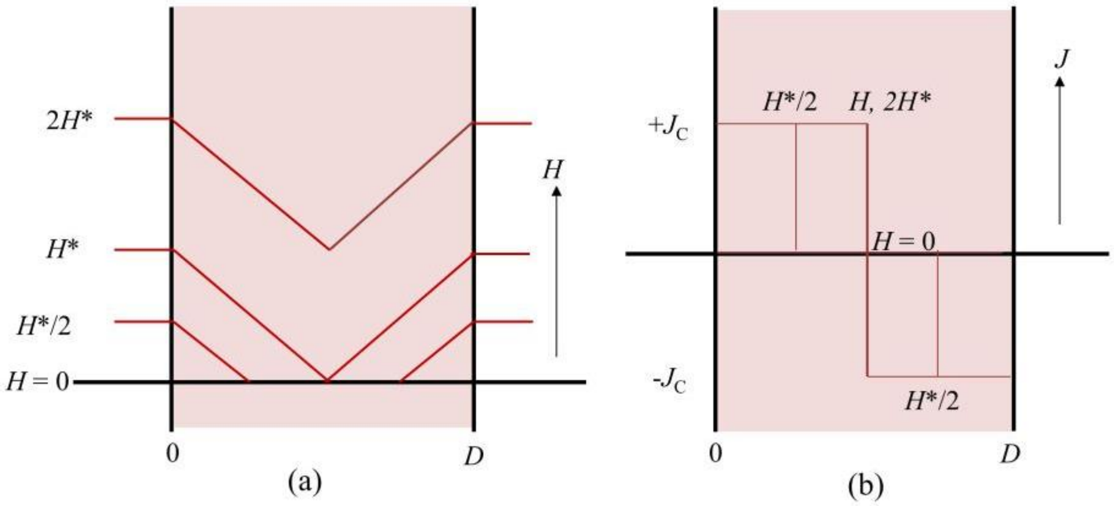

Figure 2.5: Internal profiles for the slab superconductor magnetized in a parallel field to its surface of thickness D; (a) local fields and (b) current distribution for fields 0, $H^*/2$, H^* and $2H^*$ (Bean, 1964).

There are three states of current flow at a given axis of magnetic field; zero current at un-achieved magnetic field regions, full flow current at perpendicular of the field axis and partial flow at gradient of magnetic field exists in inhomogeneous mixed-state superconductor (Bean, 1964). During initial stage of magnetization, the current flows in the superficial layers with thickness of d and just sufficient to reduce the internal local field to zero and can be written as:

$$d = 10H/4\pi J_C \tag{2.34}$$

Currents will flow through the entire volume of the slab at fields of $H \geq \pi J_C D/5$ or H^*. The magnetization curves of the slab then can be determined as:

$$4\pi M = B - H \tag{2.35}$$

Where $4\pi M$ is the average field created by the currents. Thus if $B = H^2/2H^*$, $-4\pi M = H - H^2/2H^*$ and if $B = H - H^*/2$, then $-4\pi M = H^*/2$. As the field is removed, the surface feels opposite direction of *emf*; hence, the surface currents reverse. At zero fields, the flux and current distribution is shown as Figure 2.6 (a) and (b) respectively.

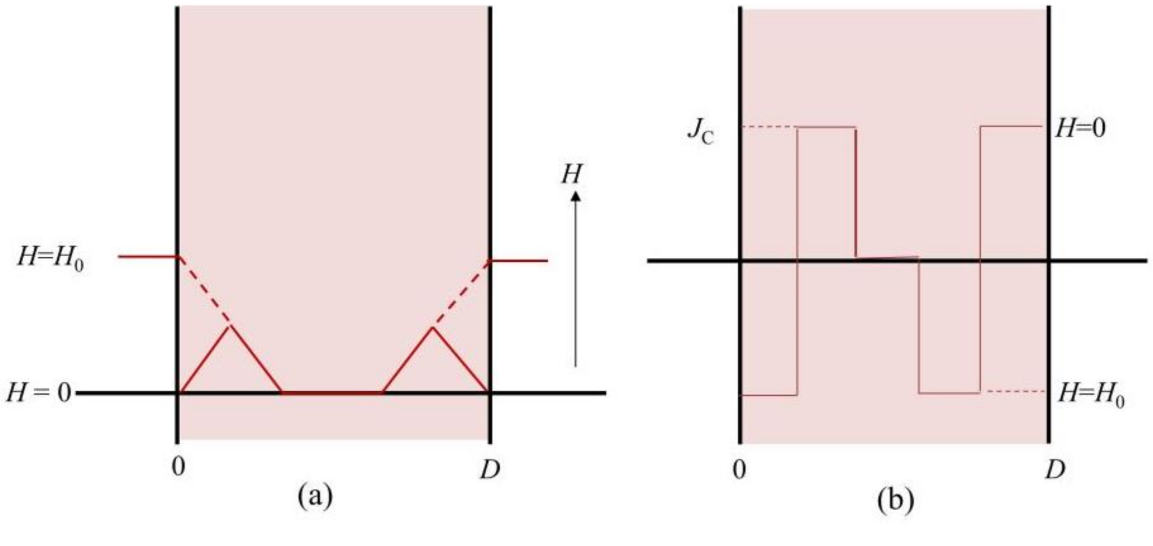

Figure 2.6: Internal profiles of the slab superconductor after the magnetic field (H_0) is removed; (a) local fields, and (b) current distribution (Bean, 1964).

Figure 2.6 (a) shows the trapped flux or remnant flux density, (B_r) as H is reduced to H_0 and can be written as:

$$B_r = H_0^2/4H^* \tag{2.36}$$

Where $H_0 \leq H^*$. Hence, the entire hysteresis loop for the slab specimen can be written as:

$$B = HH_0/2H^* \pm (H^2 - H_0^2)/4H^* \tag{2.37}$$

Where, the plus sign is applied for the course from $-H_0$ to H_0 while minus sign is applied from H_0 to $-H_0$. The hysteresis loop can be depicted as shown in Figure 2.7.

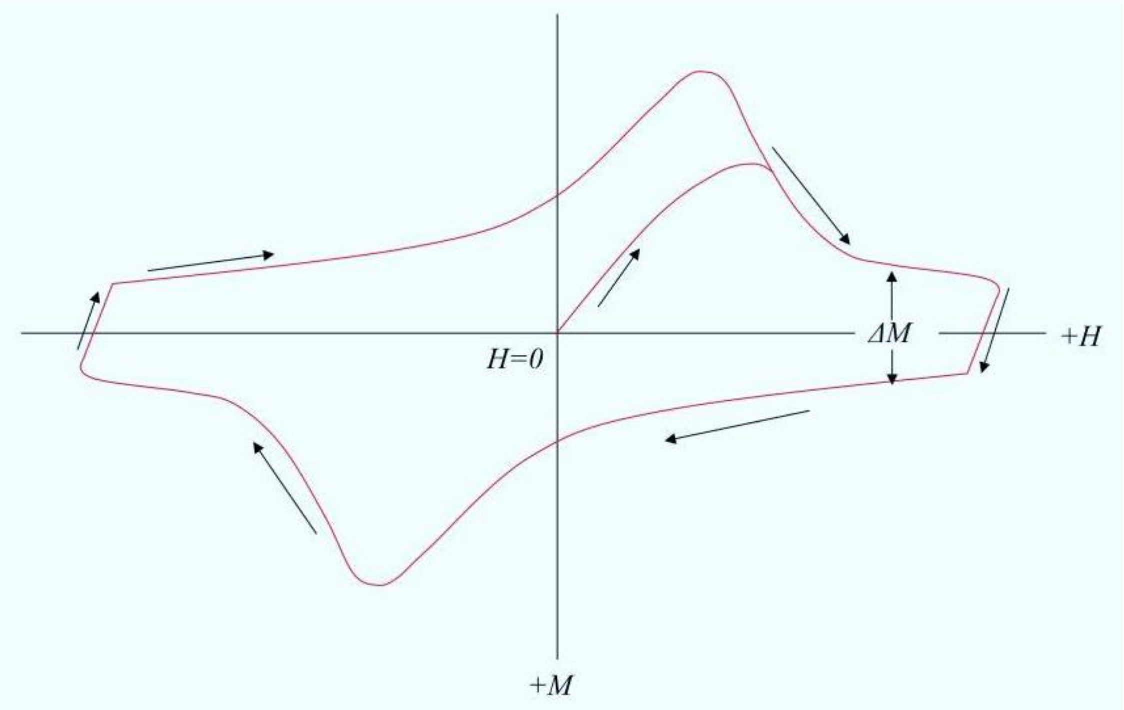

Figure 2.7: Magnetic hysteresis loop for type II superconductor. *ΔM* is the magnetization gap at increased and decreased of magnetic field (Gyorgy et al., 1989).

From Equations (2.34) and (2.35), M can be determined as $\Delta M = \frac{-J_C D}{30}$. Then the magnetization gap (ΔM) can be written as:

$$\Delta M = M_{\text{decrease}} - M_{\text{increase}} = \frac{J_C D}{30} \tag{2.38}$$

2.4.4 Extended Bean model

Bean's critical state model was extended by Gyorgy et al., (1989) to include anisotropic critical currents in explicit manner. In this extended model, magnetic field (H) is applied perpendicular to one surface of dimensions l x t as shown in Figure 2.8. As a consequence of Amperes law, the roof-like shape with vertical height to the ridge, h and horizontal distance appropriate edge to the ridge, k model can be formed.

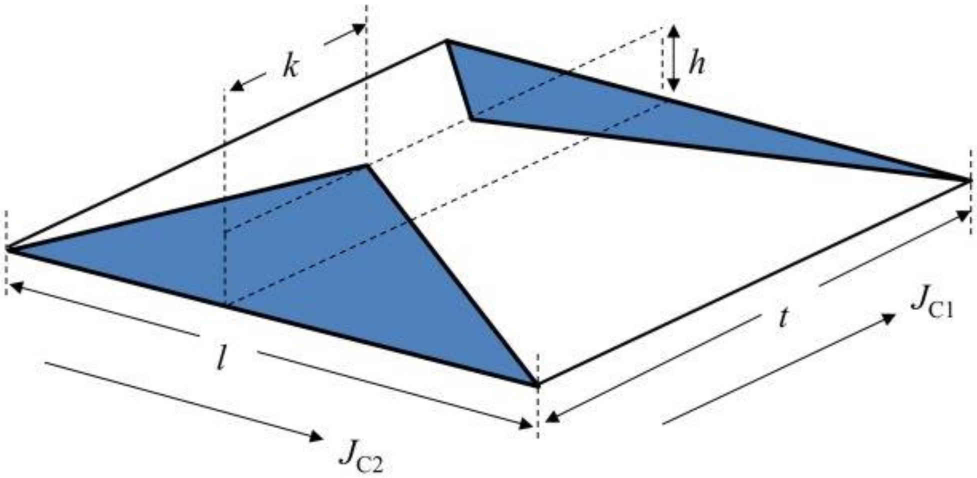

Figure 2.8: Anisotropic J_C at the magnetic field of H applied perpendicular to surface having of dimensions l x t (Gyorgy et al., 1989).

The current density along the t direction is assigned to be J_{C2} and along l direction is assigned as J_{C2}. The J_Cs at respective edges can be written as:

$$J_{C1} = \frac{2h}{t} \tag{2.39}$$

$$J_{C2} = \frac{h}{k} \tag{2.40}$$

Where, $k < ½$ or $J_{C1}/J_{C2} < l/t$. The ΔM can be determined by calculating the volume of the constructed roof-like shape (Figure 2.8) as follows:

$$\Delta M = \frac{J_{c1}t}{20}\left(1 - \frac{t}{3l}\frac{J_{c1}}{J_{c2}}\right) \tag{2.41}$$

For $l = t = D$ and $J_{C1} = J_{C2},$ the ΔM can be determined as $\Delta M = J_C D / 30$ which is in agreement with the Bean's model (2.38). Thus ΔM can be written as:

$$\Delta M = \frac{J_c}{20}\left(l - \frac{t}{3l}\right) \tag{2.42}$$

Hence,

$$J_C = \frac{20\Delta M}{\left(l - \frac{t}{3l}\right)} \tag{2.43}$$

Equation (2.43) can be used to determine magnetic J_C of rectangular-shaped superconductor for $l < t$.

2.5 $YBa_2Cu_3O_{7-\delta}$ superconductor

$YBa_2Cu_3O_{7-\delta}$ was discovered by Wu et al. (1987). It is the first superconductor to have T_C above 77 K and classified as type II superconductor. Three different metals in the $YBa_2Cu_3O_{7-\delta}$ superconductor are yttrium (Y), Barium (Ba) and Copper (Cu) which exists with the mole ratio of 1:2:3, respectively. The unit cell of $YBa_2Cu_3O_{7-\delta}$ consists of three pseudocubic elementary perovskite unit cells as shown in Figure 2.9.

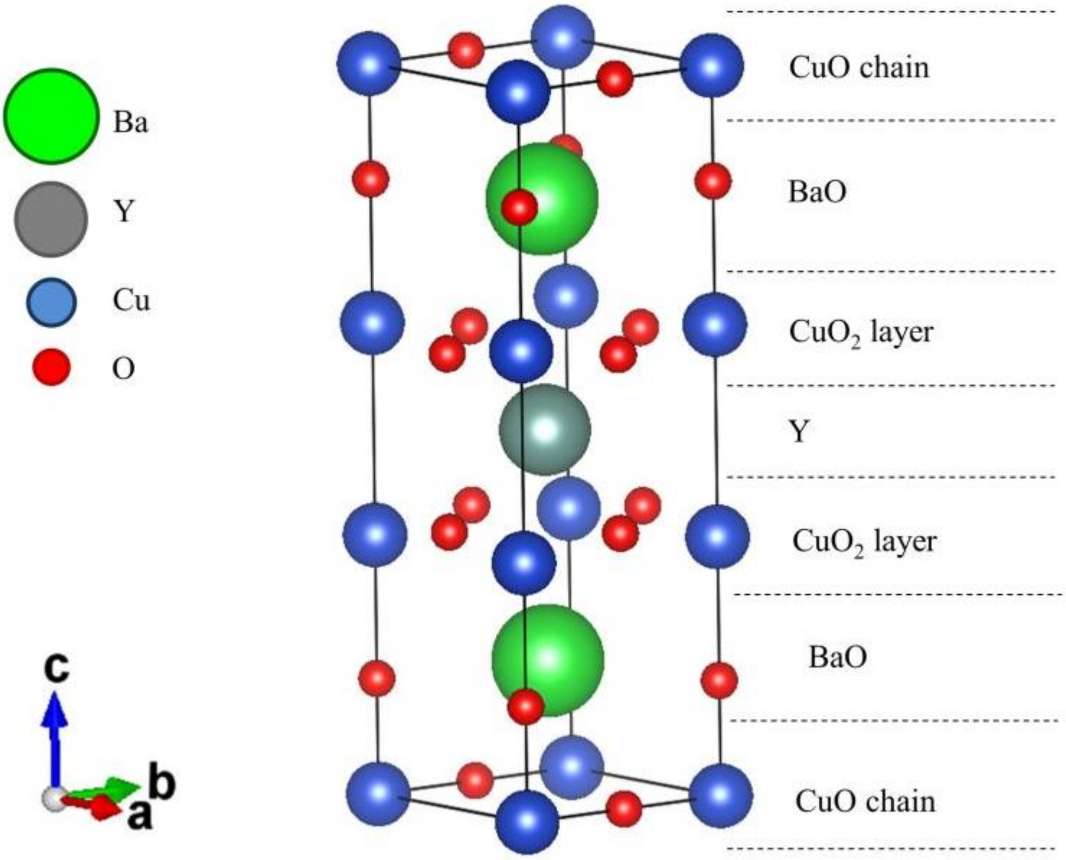

Figure 2.9: Crystal structure of $YBa_2Cu_3O_{7-\delta}$.

Each perovskite unit cell contains a Y or Ba atom at the centre of the unit cell. As shown in the Figure 2.9, Ba stays at the centre of the top and bottom unit cell while Y stays at the centre of the middle one. Thus, Y and Ba are stacked in the sequence of Ba–Y–Ba along the c-axis. All corner sites of the unit cell are occupied by Cu, which have different coordination number of Cu (1) and Cu (2) with respect to oxygen atoms.

There are four possible crystallographic sites for oxygen: O(1), O(2), O(3) and O(4). The coordination polyhedra of Y and Ba with respect to oxygen are different. The tripling of the perovskite unit cell leads to nine oxygen atoms, whereas $YBa_2Cu_3O_{7-\delta}$ has seven oxygen atoms. Therefore, it is referred to as an oxygen-deficient perovskite structure. Since there are oxygen deficiencies, the Cu valencies are in a mixed state and the chemical formula of this superconductor can be written as $YBa_2Cu^{2+}{}_2Cu^{3+}O_{7-\delta}$. The Cu^{2+} ions occupy CuO_2 layers while Cu^{3+} ions occupy the CuO chains. Hence, the structure has a stacking of different layers: $(CuO)(BaO)(CuO_2)(Y)(CuO_2)(BaO)(CuO)$. While, CuO chains act as the charge reservoir, CuO_2 layers act to supply the hole to the superconductor. The role of Y plane is to serve as a spacer between two CuO_2 planes.

The oxygen deficiency, δ plays an important key in determining the lattice parameters of $YBa_2Cu_3O_{7-\delta}$ superconductor (Kishio et al., 1987, Cava et al., 1990, Conder, 2001). For $\delta < 0.6$, $YBa_2Cu_3O_{7-\delta}$ has orthorhombic structure. For $\delta = 0$, lattice constants of this compound is $a = 3.821$ Å, $b = 3.885$ Å and $c = 11.676$ Å. The lattice parameters for various oxygen deficiencies are shown in Figure 2.10. On the other hand, for $\delta = 1$, the $YBa_2Cu_3O_{7-\delta}$ have tetragonal structure with lattice constants of $a = b = 3.857$ Å and $c = 11.819$ Å. The oxygen deficiencies also affect the T_C of $YBa_2Cu_3O_{7-\delta}$ (Ossandon et al., 1992, Skakle, 1997). The δ dependence T_C for $YBa_2Cu_3O_{7-\delta}$ is shown in Figure 2.11. $YBa_2Cu_3O_{7-\delta}$ only achieves superconducting state if $\delta < 0.6$. For $\delta > 0.6$, $YBa_2Cu_3O_{7-\delta}$ acts like insulator or semiconductor and never achieves superconductivity even though at very low temperatures. Doping of oxygen will attract the electron from CuO_2 layer then transforming $YBa_2Cu_3O_{7-\delta}$ into metal-like material. Hence, for $\delta > 0.6$, $YBa_2Cu_3O_{7-\delta}$ achieves superconductivity with higher T_C which is maximized to 92 K when $\delta \approx 0.07$. Table 2.1 lists the critical parameters for $YBa_2Cu_3O_{7-\delta}$ superconductor.

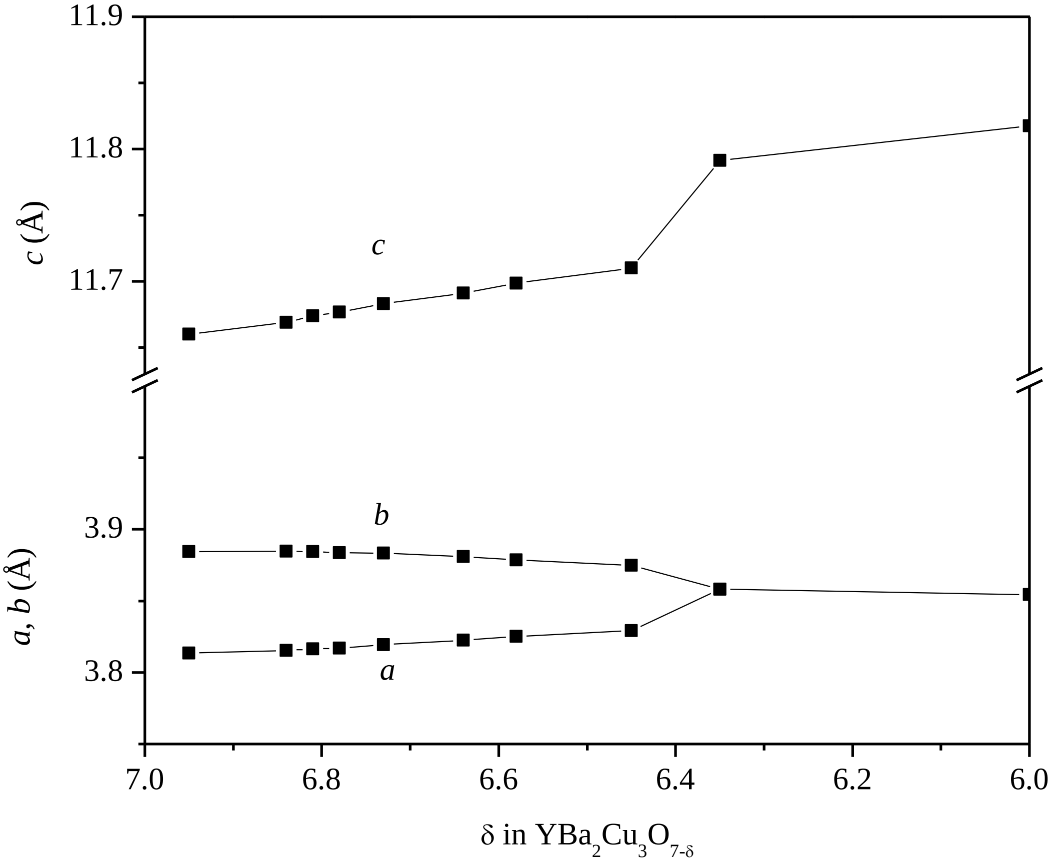

Figure 2.10: Lattice parameters for $YBa_2Cu_3O_{7-\delta}$ with different δ (Cava et al., 1990).

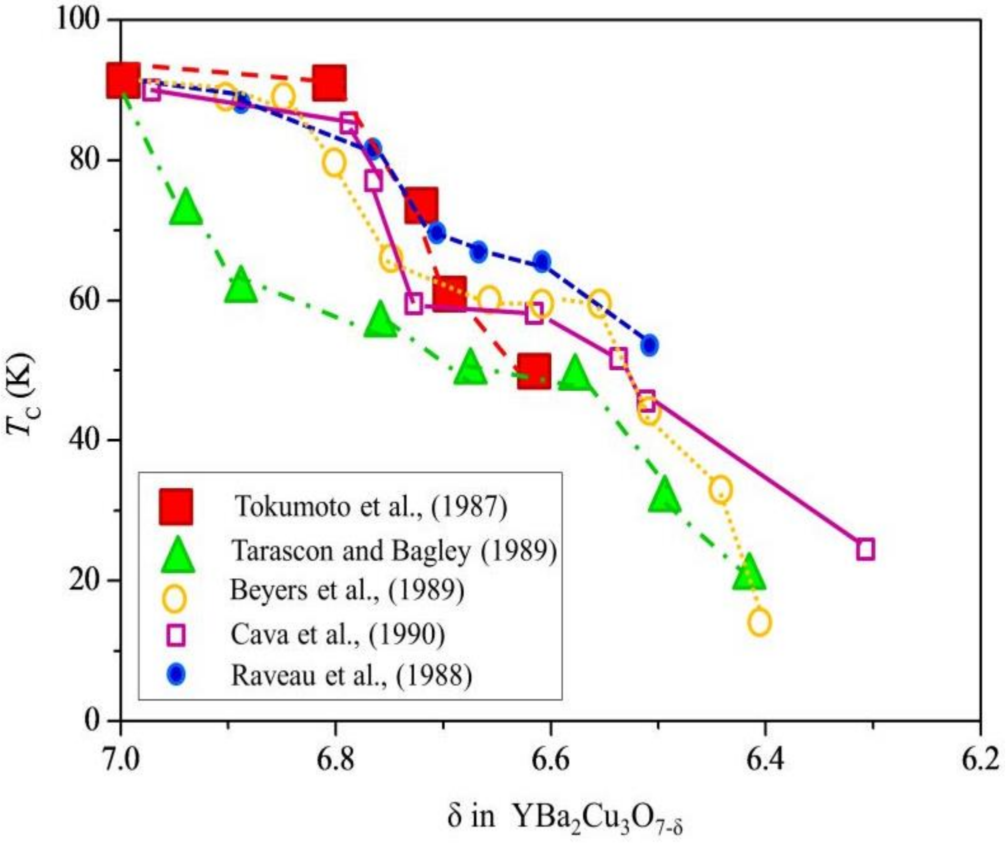

Figure 2.11: Oxygen deficiencies, δ dependence T_C for various $YBa_2Cu_3O_{7-\delta}$ samples.

Table 2.1: Critical parameters of $YBa_2Cu_3O_{7-\delta}$ superconductor (Roslan, 2004).

Critical parameters	**Value**
T_C (K)	92
$H_{C(0)}$ (T)	1.27
$H_{\parallel C2}$ (T)	30
$H_{\perp C2}$ (T)	220
$J_{C\parallel}$ (A/cm^2) at 77 K	1.8 x 10^6
$J_{C\perp}$ (A/cm^2) at 77 K	2 x 10^4
ξ_{ab} (nm)	1.5 - 3
ξ_c (nm)	0.2 - 0.6
λ_{ab} (nm)	140

2.5.1 Addition of nanoparticles in bulk $YBa_2Cu_3O_{7-\delta}$

$YBa_2Cu_3O_{7-\delta}$ remains superconducting though penetrated by magnetic fluxes at below H_{C2}. This makes the superconductor to operate at high temperature at above 77 K and in presence of high magnetic field. In the presence of vortices and at high operating temperature, $YBa_2Cu_3O_{7-\delta}$ superconductor suffers the reduction of J_C due to vortex movement and vortex creep. For bulk polycrystalline $YBa_2Cu_3O_{7-\delta}$, weak connection at the grain boundaries further reduces the J_C. The low J_C of typical pure single phase

$YBa_2Cu_3O_{7-\delta}$ can be increased as occurred in several $YBa_2Cu_3O_{7-\delta}$ related epitaxial thin films where it achieved J_C > $MAcm^{-2}$ when induced by particle irradiation as flux pinning center (Foltyn et al., 2007). However, research on polycrystalline $YBa_2Cu_3O_{7-\delta}$ is still essential for superconducting engineering in searching simpler processes with lower cost.

In order to sustain high J_C in bulk $YBa_2Cu_3O_{7-\delta}$, the vortices need to be pinned to restrict their movement. This can be done by various pinning mechanisms. First mechanism is inducing defects into $YBa_2Cu_3O_{7-\delta}$. Defects such as twin boundaries (Flippen et al., 1995), atomic substitution (Baldha et al., 1995), planar faults (Gurevich et al., 1998), lattice disorder (Crabtree et al., 2000) and stacking faults (Zhou et al., 2002) have been reported to produce non-superconducting region to pin the vortex. However, this mechanism traps only a fraction of the vortex and therefore considered weak pinning sites. Furthermore it is difficult to induce defects at specified structure.

The defects can be induced by using irradiation or chemical doping. In chemical doping, elements like silver (Ag) (Sen et al., 1991, Plech et al., 2001), aluminums (Al) (Zhang et al., 1995, Brecht et al., 1996, Antal et al., 2009), platinum (Pt) (Longhorn, 1996), rhodium (Rd) (Longhorn, 1996), sodium (Na) (Zou and Zhang, 2000), potassium (K) (Celebi et al., 2000), calcium (Ca) (Giri et al., 2005), gadolinium (Gd) (Ozturk et al., 2007) and praseodymium (Pr) (Singal, 2011) are purposely used to substitute certain atomic sites (Cu or Y or Ba) of $YBa_2Cu_3O_{7-\delta}$. Indeed, chemical doping is proven to increase the J_C but it resulted in significant decrease of T_C since the doping elements alter the orthorhombic structure of $YBa_2Cu_3O_{7-\delta}$ superconductor.

One promising method to pin the vortex and to increase the J_C is to incorporate second-phase nanoparticles into $YBa_2Cu_3O_{7-\delta}$ matrix (Matsushita, 2007). Since the ξ of $YBa_2Cu_3O_{7-\delta}$ at 77 K is around 3 nm, the incorporated nanoparticles with size ranging from 3 to 10 nm can be efficiently used to pin the vortex (Moutalibi and M'chirgui, 2007). The effectiveness of this method is demonstrated using various nanoparticles; such as, SiO_2 (Takao et al., 1999), ZrO_2 (Zhang and Evetts, 1993), Y_2O_3 (Lei et al., 2011, Goswami et al., 2007), CeO_2 (Lee et al., 2009), SnO_2 (He et al., 2001), Al_2O_3 (Mellekh et al., 2007, Moutalibi and M'chirgui, 2009). From these studies, it is confirmed that the nanoparticles need to be located in the CuO_2 planes to interact directly with the vortex. Furthermore, high density and good distribution of nanoparticles is required to pin the vortex in different layer.

2.5.2 Others work of adding Al_2O_3 nanoparticles into $YBa_2Cu_3O_{7-\delta}$

The Al_2O_3 nanoparticles have attracted much attention to be used as pinning centre material in $YBa_2Cu_3O_{7-\delta}$ superconductor (Mellekh et al., 2007). The reasons are; the Al_2O_3 nanoparticles are good insulator, available, easy to fabricate, high thermal stability, dense compared with other common inclusions, better hardness and low cost. The main factor of Al_2O_3 nanoparticles for being chosen is due to its influence towards superconductive properties of $YBa_2Cu_3O_{7-\delta}$ compound; especially, to pin the vortex and to increase the J_C. These unique properties of Al_2O_3 nanoparticles compared with other common inclusions make it suitable for adding into $YBa_2Cu_3O_{7-\delta}$.

Prior intentional adding of Al_2O_3 into $YBa_2Cu_3O_{7-\delta}$, it had been used as crucible during crystal growth of $YBa_2Cu_3O_{7-\delta}$ superconductor (Siegrist et al., 1987). Due to high processing temperature, unexpected phase transition of aluminium was occurred in the crystal of superconductor and thus affected the superconductive properties at which T_C and J_C was reduced and improved, respectively. Then the influences of Al towards the superconductive properties of $YBa_2Cu_3O_{7-\delta}$ were studied by purposely adding Al_2O_3 powder in raw materials during the production of $YBa_2Cu_3O_{7-\delta}$. It came out that the J_C of $YBa_2Cu_3O_{7-\delta}$ was significantly increased by this addition.

There are two possible mechanisms by which Al_2O_3 improves the performance of $YBa_2Cu_3O_{7-\delta}$ superconductor. Firstly, Al_2O_3 nanoparticles act as pinning centre in $YBa_2Cu_3O_{7-\delta}$ grain structure (Mellekh et al., 2006). Secondly, during processing at high temperature for long period of time, Al_2O_3 diffuses into $YBa_2Cu_3O_{7-\delta}$ and replaces certain atoms at certain sites. This induces defects in $YBa_2Cu_3O_{7-\delta}$ (Azzouz et al., 2007). In most studies, nanoparticles of Al_2O_3 were added to act as pinning centre material. The criterion for excellent pinning centre is fulfilled by Al_2O_3 nanoparticles as reported by Moutalibi and M'chirgui (2009). They proved that by adding small amount (<0.1 wt. %) of Al_2O_3 nanoparticles having average size of 10 nm, the flux pinning behaviour of $YBa_2Cu_3O_{7-\delta}$ can be improved.

In some other study it was found that nanoparticles of Al_2O_3 effects the T_C value (Antal et al., 2009). Taking into account that Y and Al are isovalent and the ionic radius of Y^{3+} (0.90 Å) is higher than the ionic radius of Al^{3+} (0.56 Å), Al can occupy the Y sites when $YBa_2Cu_3O_{7-\delta}$ ceramic is added with Al_2O_3 (Mellekh et al. 2006). On the other hand, Azzouz et al., (2007) concluded that Al from Al_2O_3 is capable to substitute both Cu in Cu atoms chains, which is in relation with superconductive properties of $YBa_2Cu_3O_{7-\delta}$ system. The substitution does not alter the structural symmetry of $YBa_2Cu_3O_{7-\delta}$ but the orthorhombicity of the system is decreased by increasing of Al_2O_3 content. These changes affect the oxygen content of crystals, and the superconducting transition temperature is decreased accordingly. Table 2.2 lists T_C and J_C values of $YBa_2Cu_3O_{7-\delta}$ added with Al_2O_3 nanoparticles.

The incorporation of Al ions from Al_2O_3 into $YBa_2Cu_3O_{7-\delta}$ induce defects in the crystal but is not sufficient to provide high density of pinning sites. Furthermore, this incorporation reduces the available Al_2O_3 nanoparticles for acting in the main pinning mechanism. This resulted in lower J_C than it supposed to be. Thus, the addition of Al_2O_3 nanoparticles as pinning centre material in $YBa_2Cu_3O_{7-\delta}$ need to be further optimized for higher J_C values.

Table 2.2: T_C and J_C of Al_2O_3 nanoparticles added $YBa_2Cu_3O_{7-\delta}$ obtained from various studies.

Studies	**Al_2O_3 size (nm)**	**T_C (K)**	**$J_C\perp$ at 77 K (A/cm^2)**
(Mellekh et al., 2006)	50	90	200
(Azzouz et al., 2007)	50	90.5	191.5
(Moutalibi and M’chirgui, 2009)	10	87	~1000
(Albis et al., 2010)	50	80	3500

Over last few years, all studies are using mechanical mixing or solid state processing to add nanoparticles into the bulk $YBa_2Cu_3O_{7-\delta}$ matrix. However, through this processing technique, Al_2O_3 nanoparticles generally possessed a wide distribution of particle size. Therefore, the induced defects were random and not homogeneous inside the superconducting matrix. This result in a low density of effective pinning centres at high temperature i.e,; a significant decrease of T_C at high level of addition (Azzouz et al., 2007). Considering that this technique involves high temperature and long period of heating steps, the inhomogeneous distribution of Al_2O_3 nanoparticles can be easily reduced and can be diffused into $YBa_2Cu_3O_{7-\delta}$ structure. Thus, to obtain high J_C without lowering T_C, Al_2O_3 nanoparticles need to be uniformly distributed in $YBa_2Cu_3O_{7-\delta}$ matrix of superconductor.

2.6 Synthesis of $YBa_2Cu_3O_{7-x}$ powder

Powder synthesis is the primary and fundamental step before fabricating devices such as bulk or film during ceramic processing. Therefore, careful selection of synthesis method is very important as this could result in different properties and quality of the fabricated device. Generally, dense ceramic sample fabrication demands homogeneous, single phase powder and adequate distribution of particle size as the starting material. The preparation of $YBa_2Cu_3O_{7-\delta}$ superconductor powder can be done by various techniques such as the conventional solid state reaction (Wu et al., 1987), sol gel (Kordas, 1990, Kani et al., 1991 and Yeoh and Shukor, 2008), micro-emulsion method (Vipulanandan and Li, 2003), co-precipitation technique (Kumar et al., 1993 and Bhargava et al., 1995), explosive powder compaction (Mamalis, 2000) and auto-combustion technique (Xu et al., 2002 and Pathak et al., 2004). Discussing all the synthesis technique is beyond the scope of this study.

The synthesis of $YBa_2Cu_3O_{7-\delta}$ superconductor can be summarized by classifying them into two categories: conventional ceramic synthesis or solid state processing (SSP) and solution techniques. In SSP, the oxides, carbonates or nitrates of desired compound are mechanically mixed and subsequently heated to produce final powder. This process is the simplest technique and can yield a lot of quantities but the poor quality of the powder is the main drawback. Inhomogeneous mixture is obvious due to solid state process and large starting material. Even though the size of the starting materials can be reduced to a certain level by mechanical milling, contamination is imminent due to abrasion of the milling balls. This further creates another shortcoming to get pure powder due to difficulties to separate the unreacted compounds. Besides, other study showed that there is evaporation loss of Ba^{2+} and Cu^{2+} if it is calcined at temperature higher than 900 °C (Mishra and Pathak, 1992). In other word, one would not choose to use SSP if ever quality of the product is desirable.

In solution technique, processes do not involve solid state of the starting material but it is in the liquid form. A common advantage of solution techniques over the solid state synthesis is the homogeneity of mixture at molecular level whereas in solid state synthesis it is achieved only at macroscopic level. Among the solution techniques, co-precipitation and sol gel process are the most famous process. Co-precipitation may yield homogeneous powder at low calcinations temperature. However, the main disadvantage of this technique is the requirement to adjust the solution chemistry to prevent the leaching out of the constituents during precipitation (Sharma et al., 1992). Gel combustion processing method is favourable due to its ability to produce high homogeneity and nanocrystalline powder. This is technologically important, desirable as fabrication demands homogeneous, single phase powder in addition with adequate distribution of particle size.

2.7 Synthesis of Al_2O_3 nanoparticles

Generally, Al_2O_3 exists as phases such as gamma (γ), delta, theta (θ) and alpha (α) (Li et al., 2007). The thermodynamically stable and suitable phase as pinning centre material is α-Al_2O_3 which is referred as Al_2O_3 in this study. Various methods have been reported to synthesize Al_2O_3 nanoparticles including microemulsion (Wang et al., 2005), solvothermal (Mekasuwandumrong et al., 2006), chemical vapour deposition (Sivakumar et al., 2006), ball milling (Reid et al., 2008), sol gel (Mirjalili et al., 2010, Ibrahim et al., 1999), laser ablation (Piriyawong et al, 2012), hydrothermal (Hakuta et al., 2013) and citrate nitrate gel combustion (Li et al., 2007 and Pathack et al., 2002) techniques. It can be determined from these reports that the Al_2O_3 phase was successfully yielded after calcination of precursor materials at high temperature in the range of 900 to 1200 °C for 1 to 2 h. Among these methods, gel combustion process has gained considerable attention due to its simplicity, reproducibility, and more importantly the lower production cost, less time and energy consumption. Most importantly, this is the only method that suits the production of $YBa_2Cu_3O_{7-\delta}$ compound simultaneously.

2.8 Combustion synthesis

Combustion synthesis is an efficient and simple technique for producing advanced materials including ceramics, composites and intermetallic compounds. The combustion technique also known as self-propagating high temperature system was discovered by Borovinskava and colleagues in 1967 (Moore and Feng, 1995). They found that, at certain temperature the mixture of Ti and B react violently to produce TiB_2 with improved properties. Basically, the combustion technique employs self-sustaining heat from exothermic reactions to boost up reduction and oxidation reaction between reactants which are energetically efficient. Furthermore, the generated heat is high enough to volatize impurities hence to produce purer products.

Moore and Feng (1995) list the advantages of using this technique compared with conventional ceramic processing as below;

i. High purity samples can be produced since the combustion reaction generates enough heat to volatize all low boiling point impurities
ii. Low operating and processing costs as the reaction consumed short times
iii. Simple exothermic nature of this reaction requires non-expensive processing and equipment
iv. New non-equilibrium or metastable phase can be yielded from high thermal gradients and rapid cooling rates processes
v. One step synthesize and consolidation of inorganic materials into final product by utilizing the chemical energy of the reactants.

Due to these advantages, this technique has been used to synthesize materials for many applications including cutting tools; such as, TiC (Liu et al., 1995), electrodes; such as, TiN (Grami and Munir, 1989), composite materials; such as, TiC + Al_2O_3 (Bowen and Derby, 1996) and TiB_2 + SiC (Hoke et al., 1996), nanomaterials (Aruna and Mukasyan 2008), and materials with specific magnetic, electrical or physical properties such as $YBa_2Cu_3O_{7-\delta}$ (Rupp et al., 1994). Generally, the reaction of combustion synthesis can be written as

$$\Sigma n_i R_i = \Sigma n_j P_j \tag{2.44}$$

Where n_i and n_j are the stoichiometric coefficients of reactants and products while R_i and P_j are the appropriate reactants and products, respectively. There are two modes of combustion reaction which are self-propagating mode and simultaneous combustion modes. In self-propagating mode, the combustion reaction is initiated at one point of the reactant and then propagated through the reaction mixture as a form of wave. The wave moves without external heat but driven by exothermic heat formed by an adjacent layer. This mode occurred when a part of reactant mixture is exposed to the heat source thus ignited first. While in the simultaneous combustion mode, the entire mixture of reactants was combusted simultaneously as it achieves the ignition temperature, T_{ig}. This situation is occurred in a furnace heated reactants where the heat can be uniformly distributed in the entire mixture reactants.

The combustion reaction is controlled by four different temperatures; initial temperature (T_0), ignition temperature (T_{ig}), adiabatic combustion temperature (T_{ad}) and actual combustion temperature (T_{com}) (Moore and Feng, 1995). Under adiabatic condition and propagating mode, combustion reaction is ignited as the reactant was heated from T_o to T_{ig}. The amount of heat, $H(R)$ needed to increase from T_o to T_{ig} can be determined as:

$$H(R) = \int_{T_0}^{T_{ig}} \Sigma n_i C_P(R_i) dT + \sum_{T_0 - T_{ig}} n_i L(R_{i)} \qquad (2.45)$$

Where $C_P(R_i)$, $L(R_i)$ are the heat capacity and the phase transformation enthalpy (if the reactants go through phase change) of the reactants respectively. Under adiabatic conditions, the heat required to raise the temperature from T_{ig} to T_{ad} by the products, $H(P)$ can be written as:

$$H(R) = \int_{T_{ig}}^{T_{ad}} \Sigma n_i C_P\left(P_j\right) dT + \sum_{T_{ig}-T_{ad}} n_i L(P_{j)} \qquad (2.46)$$

Where $C_P(P_j)$, $L(P_j)$ are the heat capacity and the phase transformation enthalpy (if the products go through phase change) of the products respectively.

Therefore, the heat at T_{ig}, $\Delta H(T_{ig})$ can be written as:

$$\Delta \mathrm{H}\ (T_{\mathrm{ig}}) = -\ [H\ (P) + H\ (R)] \qquad (2.47)$$

The relationship between the T_0, T_{ig}, T_{ad}, T_{com}, $H(R)$, $H(P)$ and $\Delta H(T_{ig})$ can be plotted as shown in Figure 2.12.

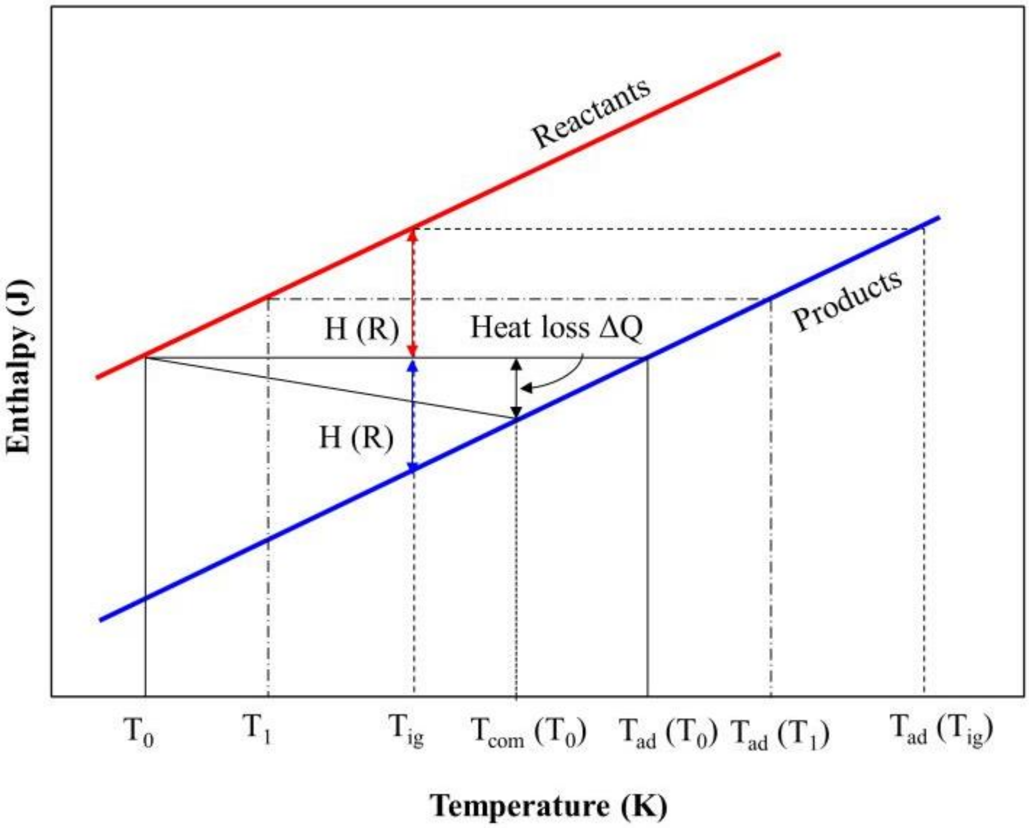

Figure 2.12: Enthalpy-temperature plot for reactants and products in combustion reaction system (Moore and Feng, 1995).

From this figure, pre-heating of reactants from T_0 to T_1 decreases the $H(R)$, and increases $H(P)$. The T_{ad} is also increased to $T_{ad}(T_1)$. Further increase of pre-heating to T_{ig} decreases the $H(R)$ to zero where the heat is totally absorbed by the products; thus, the $H(P)$ is maximized and $T_{ad}(T_{ig})$ is achieved. At this condition the ignition occurred under simultaneous combustion mode.

The heat generation and loss from the reactions controls the combustion temperature (T_{com}), wave propagation rate and stability. During combustion reaction, the generated heat can be lost in two ways which are; (1) by transferring to the adjacent reactant mixture and (2) by dissipating to the environment. Usually the T_{com} is less than maximum theoretical T_{ad} with corresponding heat loss, ΔQ as shown in Figure 2.12. Decrement in heat generation or increment in heat loss or both creates instabilities and might be a reason for slowing down or delays of wave propagation through the mixture reactant. This condition is called non-steady state mode combustion. It can be occurred in three forms; oscillating, spinning and repeated combustion (Moore and Feng, 1995). In oscillating mode, the wave is driven by rapid and slow movements while in spinning mode, the wave proceeds in spiral motion through the sample. The repeated combustion mode occurs by two combustions: the first combustion is relatively fast and localized on the surface while the second is slower and the combustion zone is much broader. The second combustion wave propagates through the passage created from the first combustion wave in the mixture reactants.

In combustion synthesis, there are two processing techniques: dry processing and wet processing (Patil et al., 2002). Through dry processing, reactants powder are mixed and compacted before heating to achieve combustion. The powder could agglomerate due to Van der Waals attractive force. This creates poor mixing and inhomogenities of the sample. In wet processing, the particles are dispersed in a solution to make moveable and efficient reaction with each other. Another way to disperse the reactant particles is to use the gel processing technique. This technique gives uniform distribution and homogeneity in the sample.

In the gel processing technique, solutions of reactants (usually nitrates) containing desired metals are complexed by complexing agent and heated to form a gel. The products of reduction and oxidation reactions remain dispersed in the gel. The combustion reactions produce sufficient heat to calcine the products and volatize all impurities. Combination of gel together wirh combustion synthesis is known as gel combustion synthesis. There are various gel system which can be used in gel combustion synthesis including urea-nitrates (Manoharan and Patil, 1992 and Baiduri et al., 1996), glycine-nitrates (Toniolo et al., 2005 and Peng et al., 2006) , carbo-hydrazide-nitrates (Aruna et al., 1995) and citrate-nitrates (Pathack et al., 2002; Li et al., 2007; Singh et al., 2007 and Marinsek et al., 2008).

2.9 Citrate-nitrate auto-combustion reaction

Citrate-nitrate auto-combustion reaction works based on oxidation of metal nitrates using citric acid as oxidizing agent. Citric acid is also acted as complexing agent to transform nitrates solutions to gel and fuels the combustion reaction. At high temperature (~ 200 °C), citric acid decomposes to aconitic acid and itaconic acid (Pathack et al., 2002). General reaction of metal nitrate with citric acid can be written as:

$$a\ \mathrm{M\,(NO_3)} + b\ \mathrm{C_6H_8O_7} \rightarrow c\ \mathrm{MOH} + d\ \mathrm{CO_2} + e\ \mathrm{H_2O} + f\ \mathrm{N_2} \qquad (2.48)$$

Where *a*, *b*, *c*, *d*, *e*, *f* and *g* (in mol) are dependent on stoichiometry of the reactions. During this reaction, lot of gases are deliberated including N_2, CO_2 and H_2O (Battacharya et al., 1990). Metal hydroxide (MOH) is transformed and calcined to metal oxide by heat supplied from the auto-combustion reaction as shown in equation below:

$$\mathrm{MOH} \rightarrow \mathrm{MO} + \mathrm{H_2O} \tag{2.49}$$

Citrate-nitrate auto-combustion reaction is ignited by the decomposition of NH_4NO_3 which was initially formed from the reaction between ammonia solutions with deliberated N_2 gases. The ignition initiates the combustion reaction of itaconic acid gel containing dispersed metal hydroxides. The combustion propagates through the entire mixture, volatizes all impurities and produces fine ashes in the form of a very low-density sponge. Since the oxide ashes are highly reactive, calcination at appropriate temperature and time is required to obtain stable powder.

The stoichiometry composition between metal nitrates and citric acid is important to optimize the auto-combustion reaction (Banarjee and Devi, 2007, Li et al., 2007). Excess or limited amount of citric acid results in repeated or delayed combustion reaction which may produce impurities. The stoichiometric composition is calculated based on the total oxidizing and reducing valencies of the oxidizer (metal nitrates) and fuel (citric acid) which serve as numerical coefficients for stoichiometric balance so that the equivalence ratio become unity. For example, at oxidizer/fuel = 1 the energy released is at maximum (Manoharan and Patil, 1992). According to the concepts used in propellant chemistry proposed by Jain et al. (1981), the elements C, H, Y, Ba, Cu, and Al are considered as reducing elements with corresponding valences of +4, +1, +3, +2, +2, +3 (or valency of the metal ion in that compound), respectively. The element oxygen is considered to be zero. Accordingly, the oxidizing and reducing valences of the compounds used in the combustion mixtures can be calculated.

The citrate-nitrate auto-combustion reaction has been used to synthesis nanocrystalline and highly pure oxide materials; such as, ZrO_2 (Juarez et al., 2000), Al_2O_3 (Pathack et al., 2002, Banarjee and Devi, 2007, Li et al., 2007), TiO_2 (Seeley et al., 2009), $Li_{1+\delta}Mn_{2-\delta}O_4$ (Hon et al., 2001), $YBa_2Cu_3O_{7-\delta}$ (Battacharya et al., 1990, Xu et al., 2002), and composite ceramics such as CeO-TiO_2 (Yana et al., 2006), Y_2O_3-ZrO_2 (Singh et al., 2007), NiO-YSZ (Marinsek et al., 2008) and Al_2O_3-ZrO_2 (Chandradas and Kim, 2009).

In synthesizing $YBa_2Cu_3O_{7-\delta}$ powder, aqueous solutions of nitrates were mixed in the mole ratio of Y^{3+}:Ba^{2+}:Cu^{2+} = 1:2:3 and added with appropriate amount of citric acid and ammonia solution. The mixture was heated at 250 °C to initiate auto-combustion reaction. The as-synthesized black ashes produce from the auto-combustion reaction were calcined at temperature ranging from 850 to 1000 °C for 1h (Battacharya et al., 1990). The $YBa_2Cu_3O_{7-\delta}$ powder prepared by this method possessed good physical properties as well as superconducting behaviour in comparison with the co-precipitation (CP) and solid-state processes (SSP) as shown in Table 2.3. The microscopic studies indicated that this technique generates very fine $YBa_2Cu_3O_{7-\delta}$ powder in nanoscale size. The highest densification of the powder obtained from auto-combustion process is mainly due to the fine size, which enhances the mass transfer rates. Extensive grain growth with little porosity was observed in the SEM micrographs for sintered pellet prepared by auto-combustion process which exhibited sharp T_C at 92 K.

Table 2.3: Comparison of the properties of $YBa_2Cu_3O_{7-\delta}$ produced using various processing techniques (Pathack et al., 2004).

Properties	**SSP**	**CP**	**Auto-combustion**
Particles size (nm)	1070	188	40 -60
Density of sintered pellets (1g.cm^{-3})	~3.4	~4.3	~4.7
Densification (%)	60	90	98
Linear shrinkage of sintered pellets at 1000 K (%)	6	16	19
Grain Morphology	Less grain growth and higher porosity	Less grain growth and more porosity	Extensive pellet type of grain growth and little porosity

In synthesis of Al_2O_3 powder using citrate-nitrate auto-combustion reaction, $Al(NO_3)_3$ was mixed with calculated amount of citric acid and ammonia solution. The mixture was heated at 200 °C. The main combustion for stoichiometric reaction is occurred at around 161.5 °C (Li et al., 2007) leaving black ashes. The ashes were transformed to Al_2O_3 powder after calcination for 1 h at 900 – 1000 °C having particle size ranging from 10 to 100 (Pathack et al., 2002). The nanoparticles of Al_2O_3 obtained from an optimized composition appeared to have a higher degree of purity, homogeneity, and better sinterability.

CHAPTER 3

METHODOLOGY

In this chapter, details of the sample preparation and characterizations techniques are presented. Preparation of the samples is divided into two parts. The first part involves the determination of citric to nitrate ratio (c/n) to yield $YBa_2Cu_3O_{7-\delta}$ where the optimized c/n was selected for the preparation of Al_2O_3 nanoparticles added $YBa_2Cu_3O_{7-\delta}$. The second part is synthesizing different compositions of Al_2O_3 added $YBa_2Cu_3O_{7-\delta}$ samples where the content of Al_2O_3 nanoparticles was varied. In Section 3.1, all materials used for preparing the samples are introduced. The auto-combustion reaction method and relevant parameters used in synthesizing the sample is briefly explained in Section 3.2. Sequentially in Section 3.3, the thermal, structural and mechanical characterization techniques and tools for measuring superconducting transition temperature (T_C) and critical current density (J_C) of the samples is specified.

3.1 Materials

The materials used for samples preparation are yttrium nitrate hydrate ($Y(NO_3)_3.6H_2O$), barium nitrate ($Ba(NO_3)_2$), copper nitrate hydrate ($Cu(NO_3)_2.3H_2O$), aluminium nitrate hydrate ($Al(NO_3)_3.9H_2O$), citric acid ($C_6H_8O_7$), and ammonia hydroxide (NH_4OH). The details of the initial materials are summarized in Table 3.1.

3.2 Samples preparation

3.2.1 Citrate to nitrate ratio (c/n) dependence of mixture solution

Y, Ba, and Cu nitrate stock solutions were mixed at a mole ratio of 1:2:3. Different concentration of citric acid was added to the mixture solution which subjected to the c/n ratio of 0.3, 0.5, 0.6, 0.7, and 0.9. Volume ratio of citric acid was calculated using Equations (3.1), (3.2) and (3.3). The mixture solutions were labelled as listed in Table 3.2.

$$\frac{\text{Citrate}}{\text{Metal nitrates}} = c/n = \frac{\text{Concentration of citric acid}}{\text{Concentraion of } Y(NO_3)_3 + Ba(NO_3)_2 + Cu(NO_3)_2} \tag{3.1}$$

$$c/n = \frac{1\text{M} \times \text{volume ratio of citric acid}}{(0.5\text{ M}\times 2) + (0.25\text{ M}\times 8) + (0.5\text{ M}\times 6)} \tag{3.2}$$

$$\text{Volume ratio of citric acid} = (c/n) \times 6 \tag{3.3}$$

Table 3.1: Raw materials used to prepare stock solutions.

Material	Manufacturing company	Molecular weight (g/mol)	Concentration (M)
$Y(NO_3)_3.6H_2O$	Sigma-Aldrich	383.01	0.50
$Ba(NO_3)_2$	Sigma-Aldrich	261.34	0.25
$Cu(NO_3)_2.3H_2O$	Sigma-Aldrich	241.60	0.50
$Al(NO_3)_3.9H_2O$	Merck Chemical	374.99	0.50
$C_6H_8O_7$	R&M Chemical	192.13	1.00
NH_4OH	R&M Chemical		1.00

Table 3.2: Citrate-nitrate ratio (c/n) composition.

Citrate-nitrate ratio, c/n	Volume ratio of citric acid	Samples label
0.3	1.8	c/n = 0.3
0.5	3.0	c/n = 0.5
0.6	3.6	c/n = 0.6
0.7	4.2	c/n = 0.7
0.9	5.4	c/n = 0.9

3.2.2 Al_2O_3 added $YBa_2Cu_3O_{7-\delta}$ mixture solution

Y, Ba, Cu and $Al(NO_3)_3$ stock solutions were mixed at mole ratio of 1:2:3:x. Calculated amount of citric acid was added to the mixture solution to obtain the best c/n. The mixtures were labelled as listed in Table 3.3.

Table 3.3: Labels of as-prepared solution varied by $Al(NO_3)_3$ compositions.

$Al(NO_3)_3$ solution (mol)	Samples label
0.00	x_{mol}= 0.00
0.02	x_{mol} = 0.02
0.04	x_{mol} = 0.04
0.06	x_{mol} = 0.06
0.08	x_{mol} = 0.08
0.10	x_{mol} = 0.10

3.2.3 Auto-combustion reaction of the gel

PH of the as-prepared mixture solution was adjusted to 7 by the addition of ammonia solution. The mixture solution was heated to 250 °C on the hot plate under infra-red radiation for achieving a uniform heating. This process gradually transformed the solution into gel as shown in Figure 3.1. A portion of this gel was kept for thermal characterization. The gel was automatically combusted by continuous heating to form very fine and reactive ashes. The physical changes of the as-prepared mixture solution through auto-combustion process are depicted in Figure 3.1.

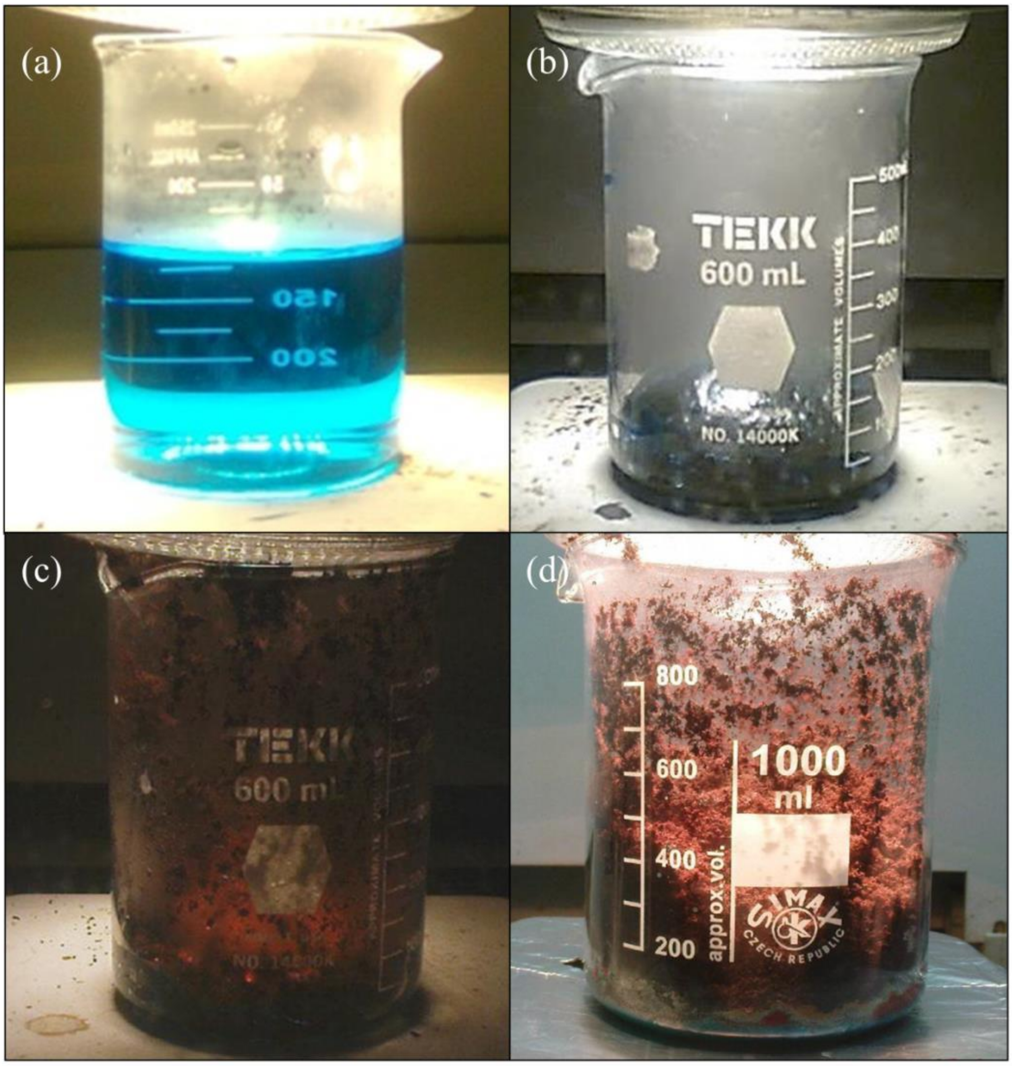

Figure 3.1: Physical appearance of samples; (a) as-prepared mixture solution, (b) gel, (c) flammable combustion and (d) ashes product.

3.2.4 Calcination and sintering process

Ashes (Figure 3.2 (a)) were calcined in the muffle furnace at 900 °C for 1 h under normal atmosphere to yield stable black powder. The calcined powder (Figure 3.2 (b)) was pelletized into 10 mm diameter x 2 mm of thickness disks by applying 12.4 MPa load. Pellet samples were sintered at 960 °C for 1 h under normal atmosphere and annealed at 500 °C for 20 h in oxygen flow (5 ml/min) in tube furnace using alumina crucibles as sample holder. Since the oxygen absorption was unable to be controlled due to higher reactivity of the sample at sintering temperature, annealing process at lower temperature is needed (Battacharya et al., 1990). Each pellet sample was self-cooled to room temperature. The as-prepared pellet is shown as in Figure 3.3. The calcination and sintering profile are depicted in Figures 3.4 and 3.5.

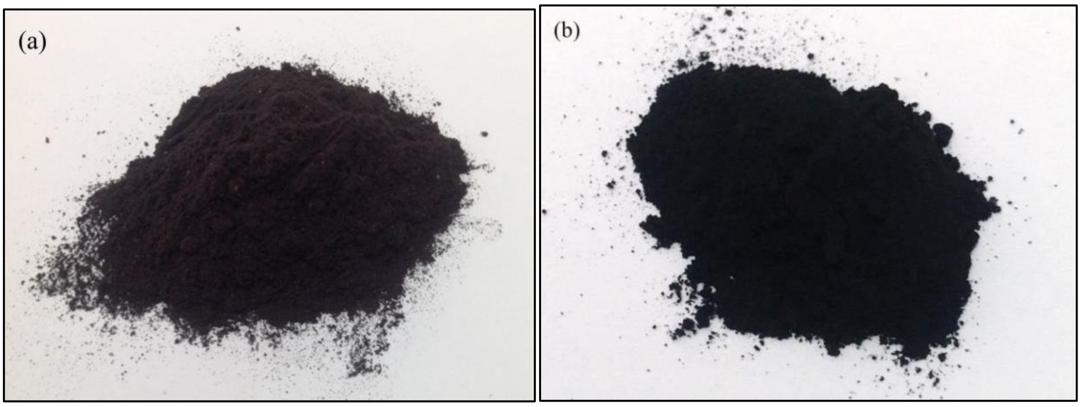

Figure 3.2: Physical appearances of the resultant powders; (a) before calcination, and (b) after calcination.

Figure 3.3: Pellet sample ready for characterizations after sintering process.

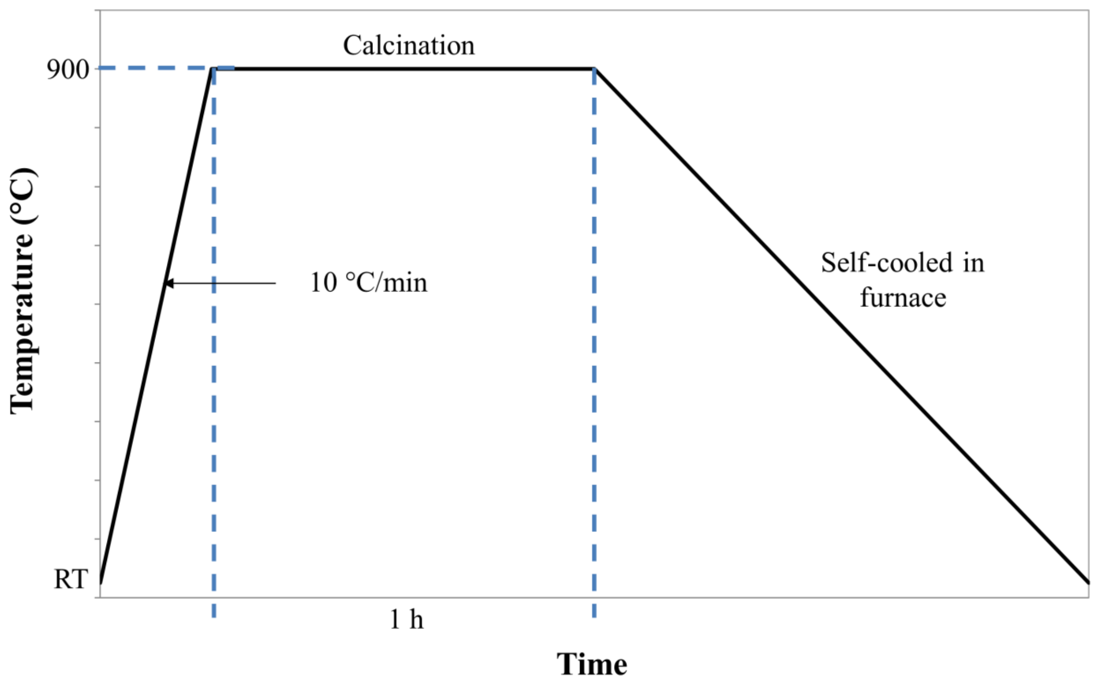

Figure 3.4: Calcination profiles of the ashes product.

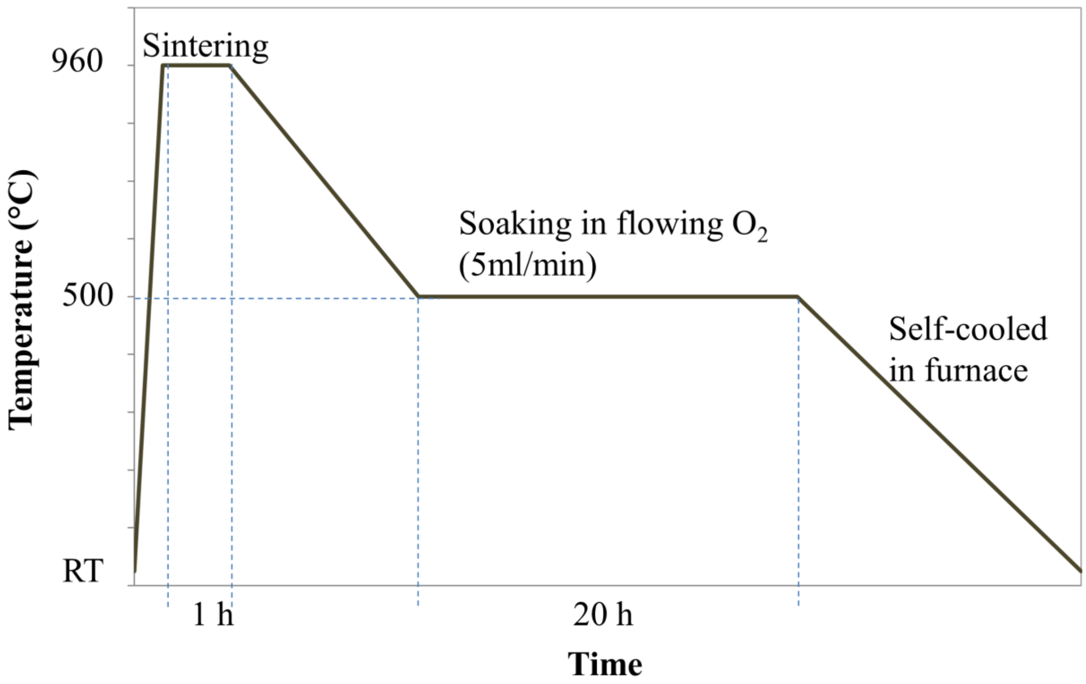

Figure 3.5: Sintering profiles of the pellet samples.

3.3 Characterization techniques

3.3.1 Thermogravimetric analysis (TGA) and differential thermal analysis (DTA)

Thermal stability and combustion profile of the precursor gel was characterized by thermogravimetric analysis (TGA) and differential thermal analysis (DTA) performed using NETZCH thermal analyser unit 409C. About 10 mg of precursor gel was constantly heated from 27 to 1000 °C with heating rate of 5 °C min^{-1} in Argon atmosphere. The change in mass was recorded at every 10 °C of temperature increment. The α-alumina was used as reference material to monitor the energy released or absorbed via reactions during the heating process at specified temperatures.

3.3.2 X-ray diffraction (XRD)

The crystal structure, phase purity of the resulting powders was examined by powder X-ray diffraction, XRD; Rigaku RINT2500 Ultra18 (Figure 3.6) using Cu$K\alpha$ radiation. The diffraction data was collected over the diffraction angle range of 2θ = 10° to 100° by step scanning width of 0.01°. Peaks assigned to Kα2 diffractions are separated from Kα1 diffractions by fitting software using Pseudo-Voight functions Lattice constants were roughly refined by Rietveld method using the Rietan-FP code (Izumi and Momma, 2007). The exact position of 2θ for each yielded peak on the XRD pattern was determined using Curve Fit software and was corrected by machine correction factor calibrated by Si standard powder. Then the crystallite size of the sample was calculated from half width-maximum peak using Debye-Scherer formula in Equation (3.4),

$$\tau = \frac{k\lambda}{\beta\ cos\theta} \tag{3.4}$$

Where, β is the broadening at half the maximum intensity in radians, k is shape factor (0.90), λ is X-ray wavelength, and τ is mean crystallite size.

Figure 3.6: Rigaku RINT2500Ultra18 XRD machine.

All significant peaks on the XRD pattern were assigned with significant diffracted plane generated by Findit program. This information was crucial in Rietan simulation program where the lattice parameters of the sample were obtained. Based on these parameters the molecular structure of the sample was built using Vesta software (Figure 3.7) and simulated to produce refined patterns.

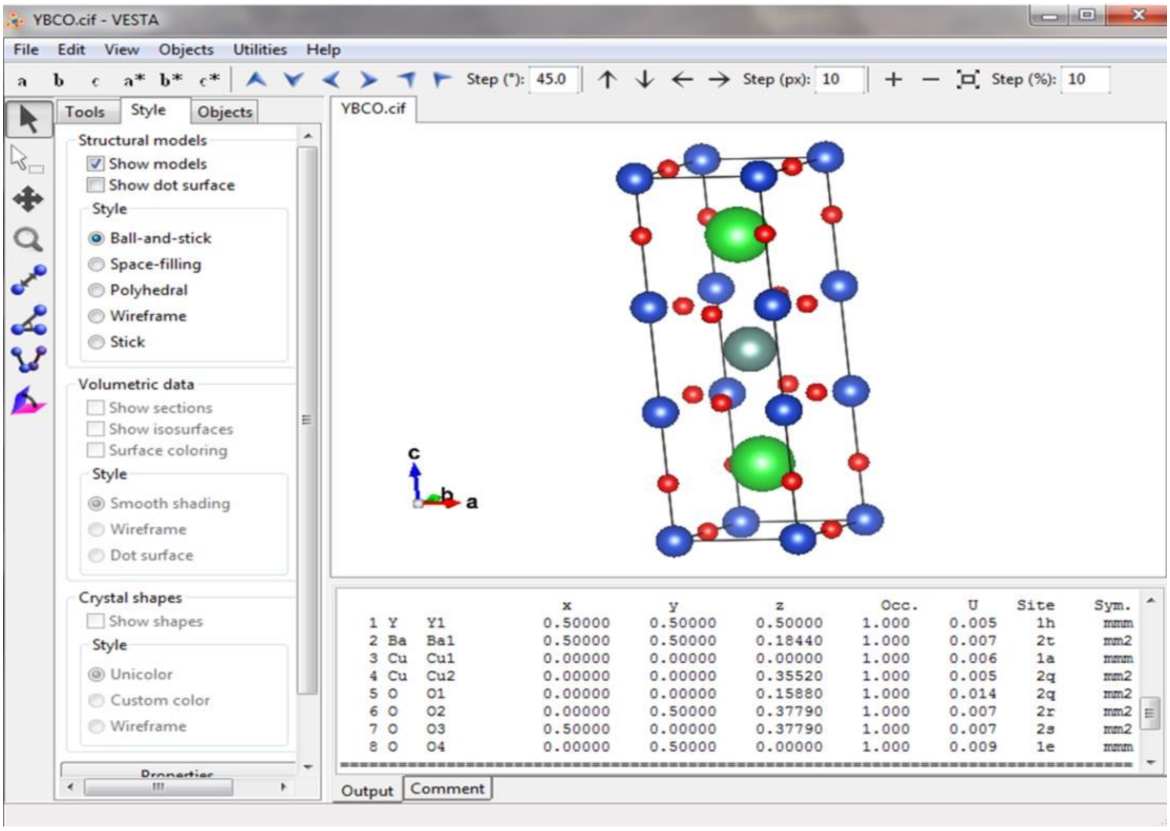

Structural models
☑ Show models
☐ Show dot surface
Style
● Ball-and-stick
○ Space-filling
○ Polyhedral
○ Wireframe
○ Stick

Volumetric data
☐ Show sections
☐ Show isosurfaces
☐ Surface coloring
Style
● Smooth shading
○ Wireframe
○ Dot surface

Crystal shapes
☐ Show shapes
Style
● Unicolor
○ Custom color
○ Wireframe

```
                        x         y         z        Occ.      U     Site    Sym.
  1 Y    Y1         0.50000   0.50000   0.50000   1.000   0.005    1h     mmm
  2 Ba   Ba1        0.50000   0.50000   0.18440   1.000   0.007    2t     mm2
  3 Cu   Cu1        0.00000   0.00000   0.00000   1.000   0.006    1a     mmm
  4 Cu   Cu2        0.00000   0.00000   0.35520   1.000   0.005    2q     mm2
  5 O    O1         0.00000   0.00000   0.15880   1.000   0.014    2q     mm2
  6 O    O2         0.00000   0.50000   0.37790   1.000   0.007    2r     mm2
  7 O    O3         0.50000   0.00000   0.37790   1.000   0.007    2s     mm2
  8 O    O4         0.00000   0.50000   0.00000   1.000   0.009    1e     mmm
===============================================================================
```

Figure 3.7: Crystal structures are drawn using 'VESTA 3 program for three-dimensional visualisation of crystal, volumetric and morphology data' (Momma and Izzumi, 2011).

3.3.3 Field emission scanning electron microscope (FESEM) and energy dispersive X-ray (EDX)

The microstructure of the as-prepared pellet sample was observed using field emission scanning electron microscope (FESEM) by acceleration voltage of 3kV. The Zeiss Auriga Ultra 40XB (Figure 3.8) was employed in this characterization technique and provided high resolution images up to 50000x magnification which were able to confirm the particle size of the sample. The collected X-ray produced by the machine was used in elemental mapping and pointed energy dispersive X-ray (EDX) analysis to determine the atomic and weight percentage of elements at specified samples area.

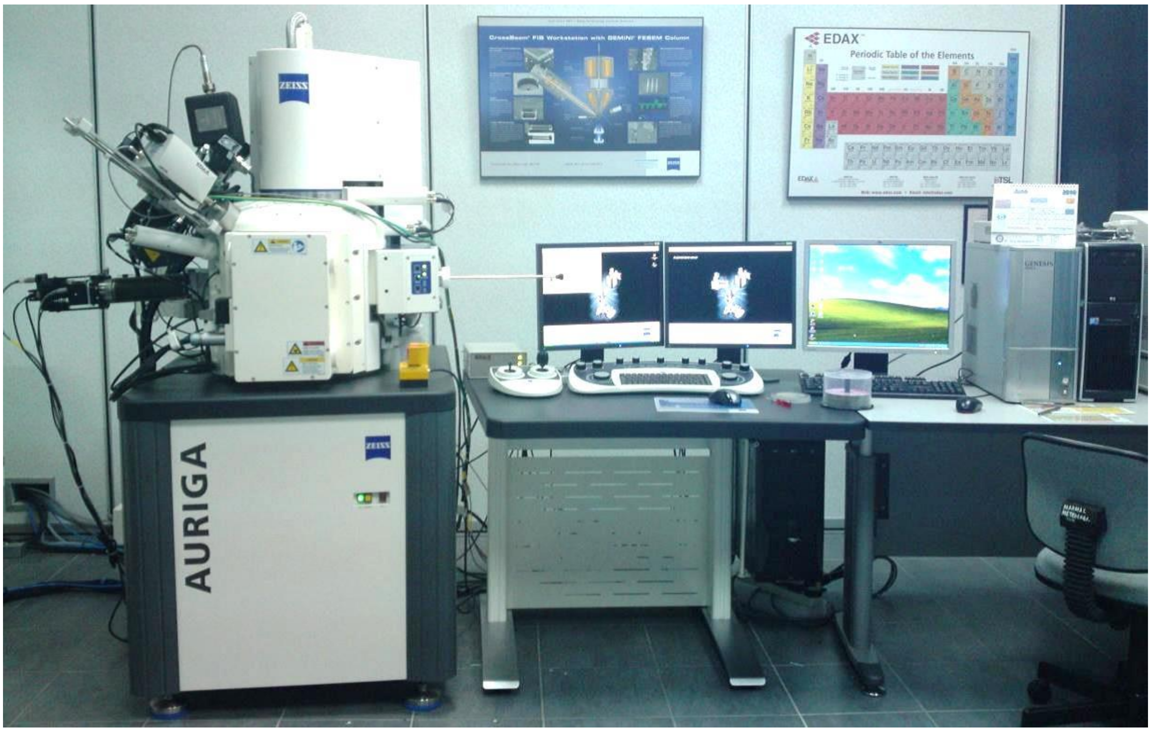

Figure 3.8: Zeiss Auriga Ultra 40 XB FESEM machine.

3.3.4 Resistivity measurement

The resistivity measurements were carried out using the standard four probe technique with silver paste contacts in conjunction with a closed cycle refrigerator. In this technique, the pellet sample was cut into 4mm x 2mm x 1mm bar using high precision Struers diamond cutter. The bar was coated with gold to improve connectivity and to control the gap distance of 0.5 mm between coated areas. Four thin silver wires with diameter of 0.2 mm were connected to the coated areas using silver paste (Figure 3.9). The sample was attached onto a sample holder in a closed cryogen chamber (SRDK-101D) for cooling purpose from 300 K to 4 K by helium gas as it is shown in Figure 3.10.

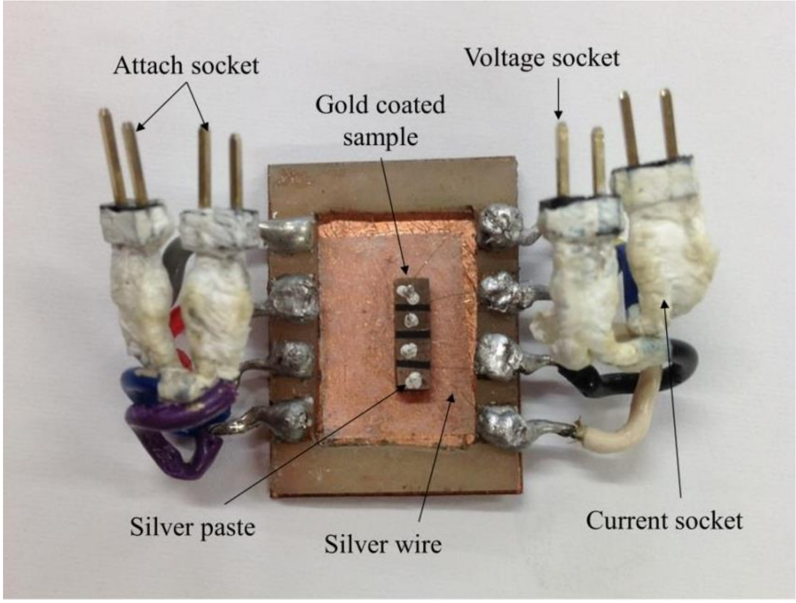

Figure 3.9: Sample holder set up for resistivity measurement.

The 0.001 mA current was applied to the sample through these 4 wires and the resistance was recorded for the temperature change of each 1 K. This step was repeated by warming up the sample from 4 to 300 K. Following the Ohm's law, the electrical resistance of the samples was determined by using Equations (3.5), (3.6), and (3.7),

$$V_+ = IR + V_o \tag{3.5}$$

$$V_- = -IR + V_o \tag{3.6}$$

$$R = \frac{V_- + V_+}{2I} \tag{3.7}$$

Where, R is electrical resistance, I is electrical current, V_0 is extrinsic resistance and V is voltage applied at forward (-) and reverse (+) condition. Resistivity of the sample was calculated by using Equation (3.8),

$$\rho = \frac{R\mathrm{A}}{l} \tag{3.8}$$

Where, ρ is resistivity, A is the area of the sample in cross section and l is the length of the sample.

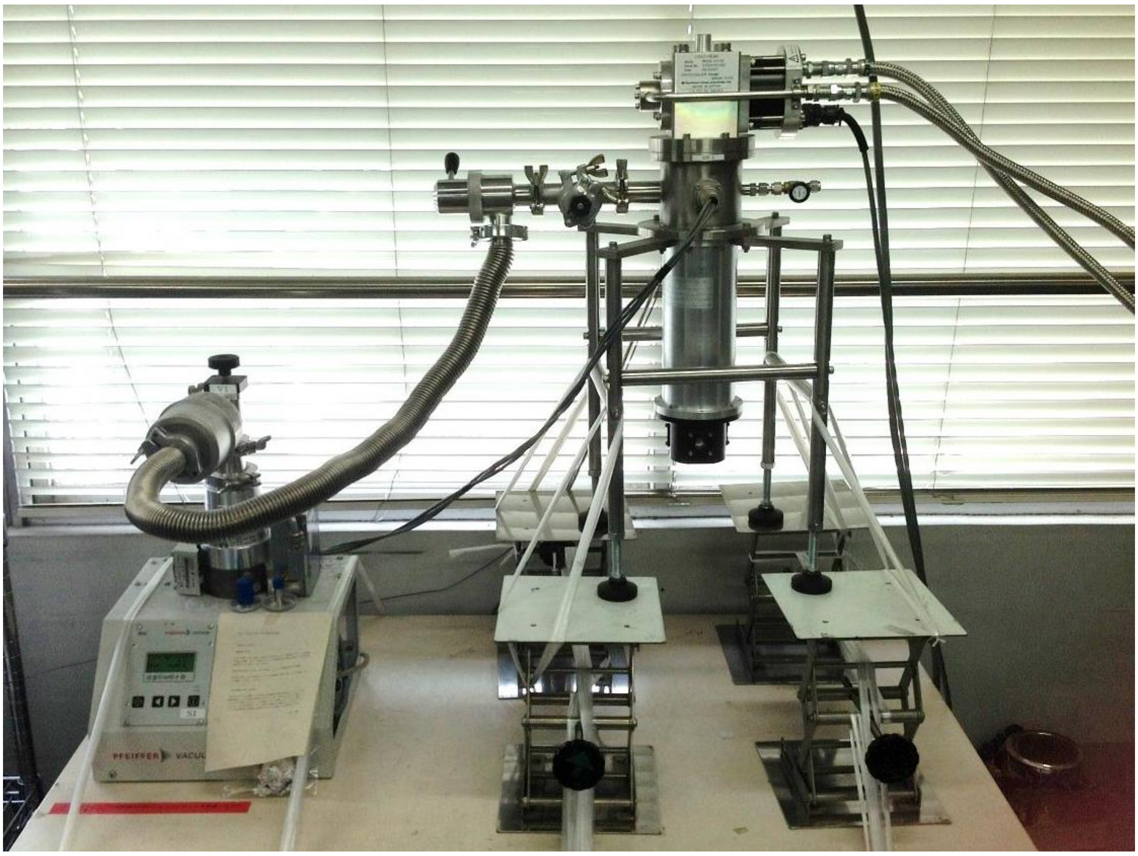

Figure 3.10: Closed cryogen chamber model SRDK-101D.

3.3.5 Defining critical temperature (T_C)

Critical temperature (T_C) of the samples was defined from the temperature dependence electrical resistivity curve as shown in Figure 3.11. The curve shows two types of T_C which are T_C onset and T_C zero. T_C onset was obtained as intersection of two tangent lines created on the curves while T_C zero was determined as the electrical resistivity achieves zero value.

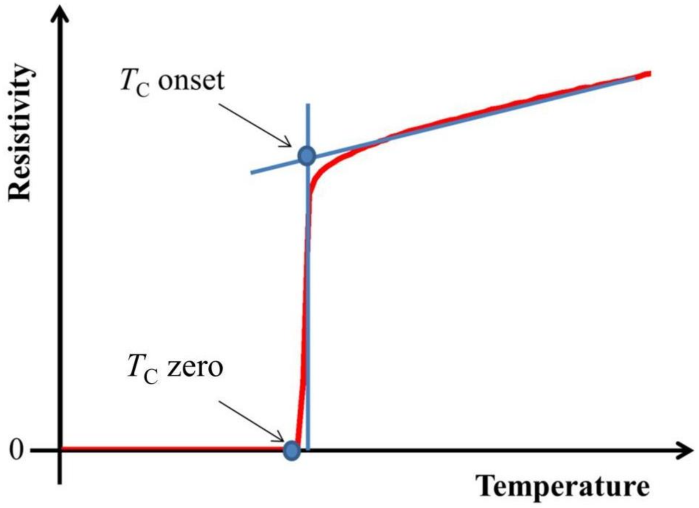

Figure 3.11: Determination of T_C onset and T_C zero from temperature dependence resistivity curve.

3.3.6 Magnetisation measurement

The magnetisation measurement was made using magnetic properties measurement system (MPMS) named superconducting quantum interference devices (SQUIDs) and was performed on 4 mm x 1.2 mm x 1.0 mm bar sample. The 1.2 mm^2 bar surface was positioned perpendicularly to the applied magnetic field in the machine using custom-made straw as sample holder (Figure 3.12). The magnetic flux ($\mu_0 H$) with the strength of -1 to 1 Tesla cycle was applied to the sample at 77 K using SQUIDs (Quantum Design Co. LTD; MPMS-XL) as shown in Figure 3.13.

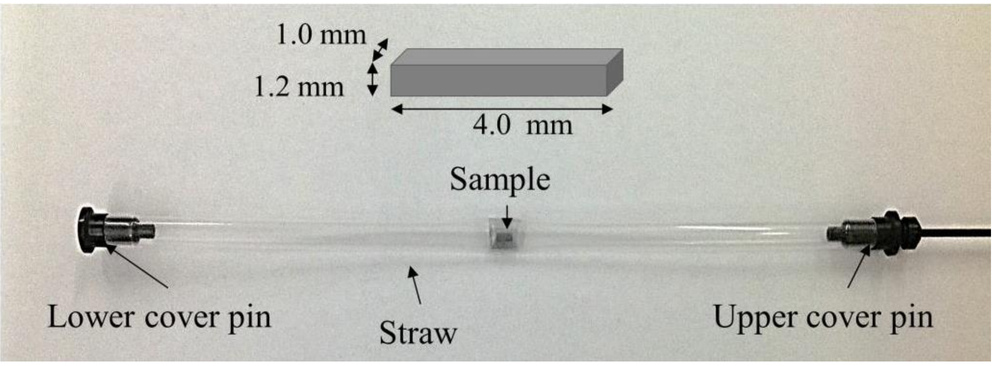

Figure 3.12: Sample holder set up for field dependence magnetization measurement.

Figure 3.13: SQUIDs (Quantum Design Co. LTD; MPMS-XL) for magnetic properties measurement.

3.3.7 Magnetic critical current density (J_C)

Magnetic critical current density (J_C) of the sample was determined by extended Bean critical state model formula (Gyorgy et al., 1989) as in Equation (3.9),

$$J_C\,(H) = \frac{20\,\Delta M(H)}{a(1-\frac{a}{3b})} \tag{3.9}$$

Where, *ΔM* is the vertical width of the magnetization hysteresis (emu·cm^{-3}), *a* and *b* (cm) are the cross-sectional dimensions of the sample perpendicular to the applied field with b ≥ a.

3.3.8 Hardness test

Hardness testing was performed using Mitutoyo AVK-C2 Vickers' hardness tester at room temperature. The diamond indenter with 136° of indentation angle was used to indent the samples at five different spots for holding time of 20 s. The Vickers hardness was calculated using Equation (3.10),

$$H_V = \frac{F}{\mathrm{A}} = \frac{kgf}{d_1 \times d_2} \tag{3.10}$$

Where, F is applied force in kgf, A is cross section of indented surface and was obtained from diameter of the two edges, d_1 and d_2.

3.3.9 Summary

The complete sample preparation steps and characterization techniques were summarized in the flowchart shown in Figure 3.14.

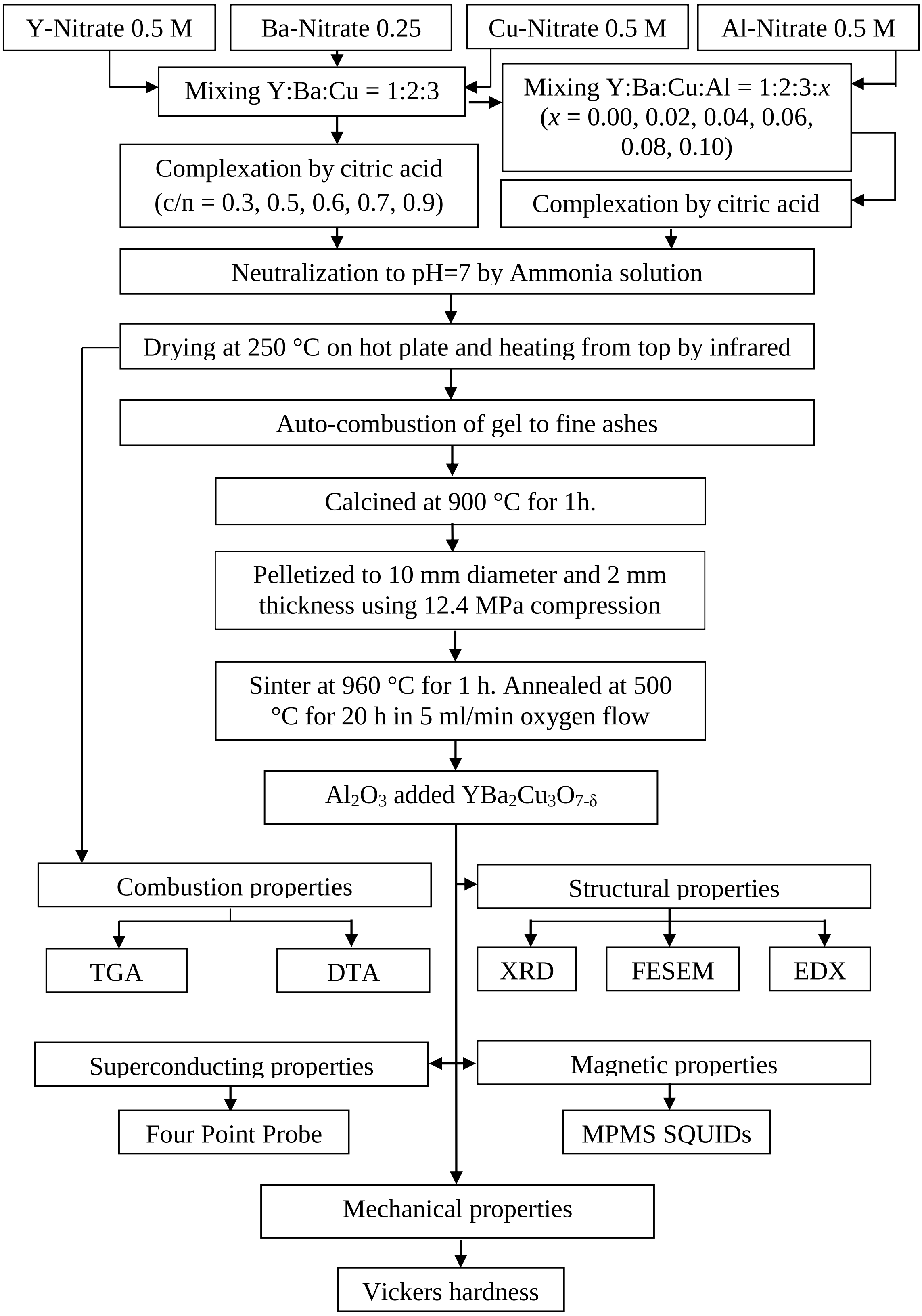

Figure 3.14: Flow chart for the preparation and characterization of Al_2O_3 nanoparticles added $YBa_2Cu_3O_7$ samples.

CHAPTER 4

EFFECTS OF CITRATE-NITRATE RATIO

This chapter presents the results of citrate-nitrate ration (c/n) effect on decomposition characteristics, structural and superconductivity properties of $YBa_2Cu_3O_7$.

4.1 Decomposition characteristic analysis

Decomposition of the precursor gel was highly influenced by the c/n and can be classified into three behavior. The first behavior is rapid decomposition of the gel samples with c/n = 0.6 and 0.7 depicted by TG/DTA curves as shown in Figure 4.1.

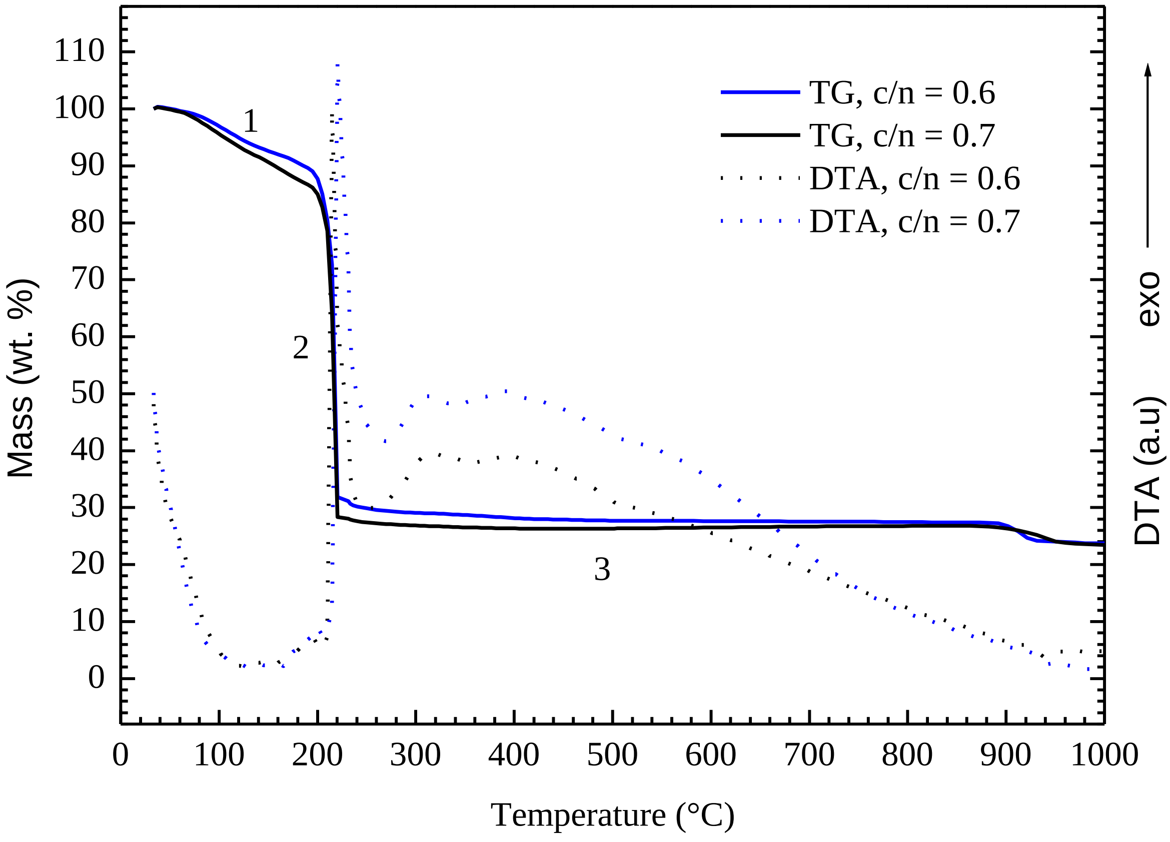

Figure 4.1: TG/DTA curves of c/n = 0.6 and 0.7 gel samples.

Rapid decomposition occurred in a single step reaction with a sharp fall of mass around 70 wt.% followed by a strong exothermic reaction occurring around 223 °C. Decomposition reaction is followed by thermally stable plateau begun at 230 °C which indicates the formation of a stable intermediate product and subsequent slow decomposition within the temperature range of 230-900 °C. Further observation showed that a small mass loss appeared at 900 °C, which might be resulted from $YBa_2Cu_3O_{7-\delta}$ phase formation.

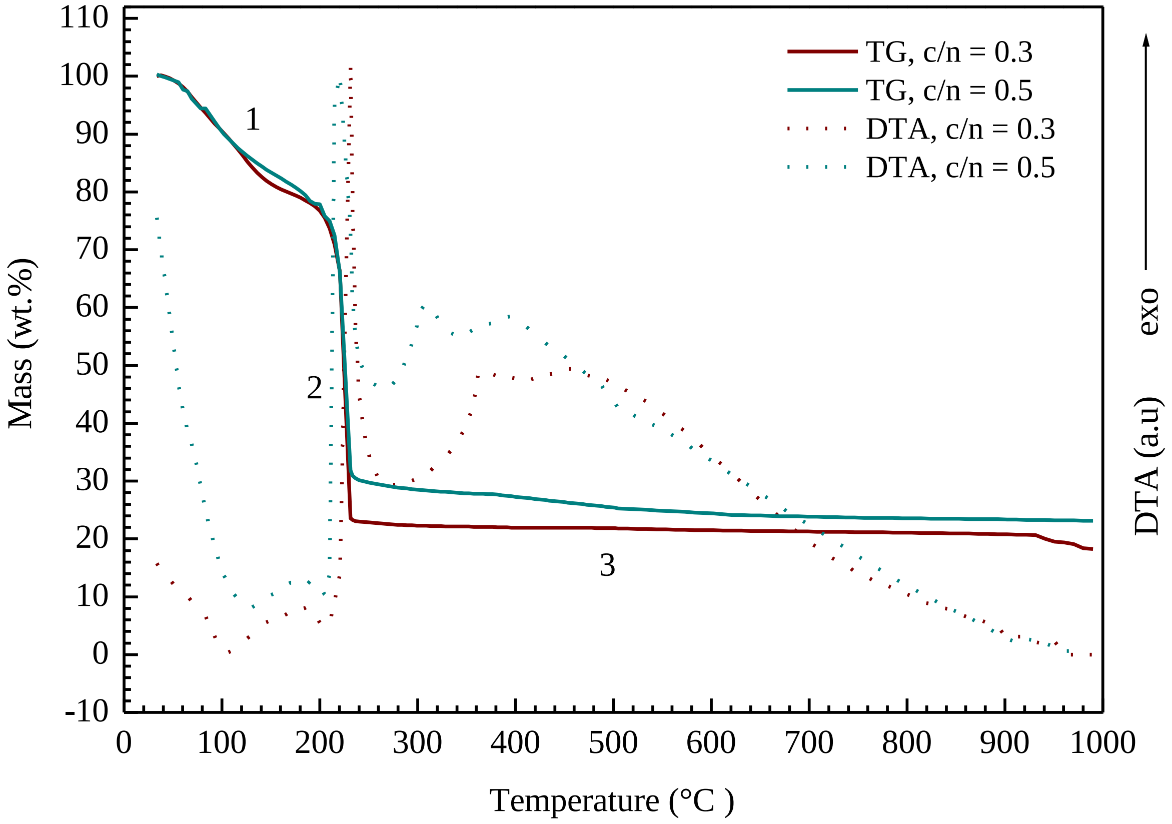

Figure 4.2: TG/DTA curves of c/n = 0.3 and 0.5 gel samples.

The second behavior is pre-decomposition of gel samples with c/n = 0.3 and 0.5 which is depicted by TG/DTA curves as shown in Figure 4.2. Precursor gel was initially decomposed around 200 °C which is before of the main combustion reaction at 240 °C through strong exothermic peak. During the initial endothermic decomposition reaction the mass loss of the precursor gel was about 25 wt. %. It was then followed by thermally stable plateau which indicated the formation of intermediate products.

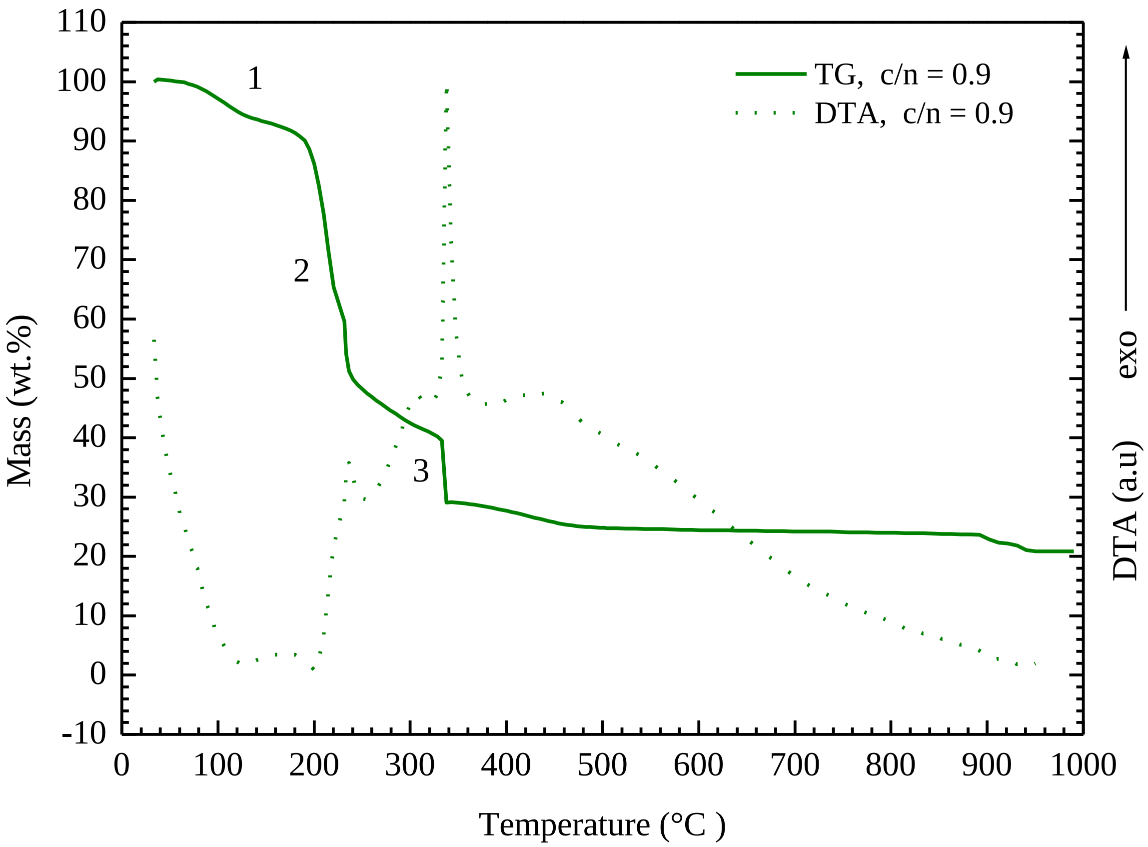

Figure 4.3: TG/DTA curves of c/n = 0.9 gel sample.

The third behavior is repeated decomposition reaction occurred in c/n = 0.9 sample. The main decomposition reactions were occurred at 240 and 330 °C as depicted by two exothermic peaks on the DTA curve as shown in Figure 4.3. It appeared that the second decomposition reaction generated much heat compare to the first decomposition reaction. Precursor gel lost about 40 wt. % of mass during the first decomposition and another 10 wt. % of mass during second decomposition. Thermally stable plateau of TG curve was observed after the second decomposition. The decomposition reactions of all gel samples at different temperatures are listed in Table 4.1.

Table 4.1: Temperature dependence decomposition behavior and reaction of the gel samples during auto-combustion reaction.

Sample (c/n)	Decomposition behavior	Reaction regards to temperature			
		1 (110 °C)	2 (200 °C)	2 (220-240 °C)	3 (330 °C)
0.3	Pre decomposition	Gel dehydration	Decomposition of un-reacted nitrates.	Main Decomposition	
0.5	Pre decomposition	Gel dehydration	Decomposition of un-reacted nitrates.	Main Decomposition	
0.6	Rapid decomposition	Gel dehydration		Main Decomposition	
0.7	Rapid decomposition	Gel dehydration		Main Decomposition	
0.9	Repeated decomposition	Gel dehydration		Main Decomposition	Second main decomposition of citric acid

Spontaneous combustion reaction of the gel samples was initiated by the decomposition reaction of ammonium nitrate (NH_4NO_3) (Hon et al., 2001). The NH_4NO_3 was formed through reaction between ammonia solution (NH_4OH) and Y, Ba and Cu nitrates as shown in Equation (4.1)

$$7NH_4OH + Y(NO_3)_3 + Ba(NO_3)_2 + Cu(NO_3)_2 \\ \rightarrow 7NH_4NO_3 + Y(OH)_3 + Ba(OH)_2 + Cu(OH)_2 \tag{4.1}$$

During heating process citric acid ($C_6H_7O_8$) was melted at 173 °C and decomposed to aconitic acid ($C_6H_6O_6$) at 175 °C by reaction shown in Equation (4.2) (Hon et al., 2001). Upon heating, aconitic acid was decomposed to itaconic acid ($C_5H_6O_4$) by reaction shown in Equation (4.3). The itaconic acid (melting point 166 °C) was polymerized and swelled by de-carboxylation process and CO_2 gas was released. The itaconic acid then decomposed to itaconic anhydrate ($C_5H_4O_3$) by further heating through the reaction shown in Equation (4.4).

$$C_6H_8O_7 \rightarrow C_6H_6O_6 \text{ (aconitic acid)} + H_2O \tag{4.2}$$

$$C_6H_6O_6 \text{ (aconitic acid)} \rightarrow C_5H_6O_4 \text{ (itaconic acid)} + CO_2 \tag{4.3}$$

$$C_5H_6O_4 \text{ (itaconic acid)} \rightarrow C_5H_4O_3 \text{ (itaconic anhydride)} + H_2O + CO_2 \tag{4.4}$$

The Y, Ba and Cu hydroxide was dispersed within polymerized itaconic acid. The flash pyrolysis of NH_4NO_3 yielded N_2, H_2O, and nascent oxygen excluded the formation of NO_x and HCN species by reaction as shown in Equation (4.5)

$$NH_4NO_3 \rightarrow N_2 + 2H_2O + O + \text{Heat} \tag{4.5}$$

The heat liberated during the decomposition reaction of ammonium nitrate was sufficient for water removal and complete transformation of $Y(OH)_3$, $Ba(OH)_2$, and $Cu(OH)_2$ to Y_2O_3, BaO and CuO respectively. The reactions can be written as shown in Equation (4.6).

$$2Y(OH)_3 + Ba(OH)_2 + Cu(OH)_2 \rightarrow Y_2O_3 + BaO + CuO + 4H_2O \tag{4.6}$$

Following the Pederson's reaction model (Banerjee & Devi, 2007), the overall decomposition reaction involving Y, Ba and Cu nitrate with citric acid can be presented as in Equations (4.7), (4.8), and (4.9);

$$6\ Y(NO_3)_3 + 5\ C_6H_8O_7 \rightarrow 3\ Y_2O_3 + 20\ H_2O + 30\ CO_2 + 9\ N_2 \tag{4.7}$$

$$9\ Ba(NO_3)_2 + 5\ C_6H_8O_7 \rightarrow 9\ BaO + 20\ H_2O + 30\ CO_2 + 9\ N_2 \tag{4.8}$$

$$9\ Cu(NO_3)_2 + 5\ C_6H_8O_7 \rightarrow 9CuO + 20\ H_2O + 30CO_2 + 9N_2 \tag{4.9}$$

Based on the concept of propellant (Manoharan & Patil, 1992), it was calculated that 9.72 mole of citric acid was required for each mole of nitrate in order to have a stoichiometric redox reaction in the gel that gives c/n = 0.6075. Near to this value, the c/n = 0.6 and 0.7 gel samples were experienced rapid combustion reaction. Rapid combustion reaction was occurred in c/n = 0.6 and 0.7 gel samples. The exothermic heat generated through this reaction was governed by thermally induced redox reaction involving the citrate and nitrate anions present in the precursor. The nitrate ions acted as oxidant and citrate ions acted as reductant in this reaction. The combustion wave propagates from the initial point to end point of the reactant and completes within a few seconds releasing a large amount of CO_2 and N_2 gases which resulting in a noticeable drastic weight loss.

Pre-decomposition reaction occurred in the c/n = 0.3 and 0.5 gel samples was due to the presence of lower amount of citric acid to form itaconic acid. The itaconic acid as complexing agent was important to prevent over dehydration of the gel samples (Li et al., 2009). This polymeric condition should be sustained before the auto-combustion reaction was ignited by NH_4NO_3 decomposition reaction. Lower amount of itaconic acid caused the gel to be dehydrated and pre decomposed. The gels lost most of the fuel (itaconic acid) during pre-decomposition reaction. Therefore, the exothermicity of the main decomposition reaction was reduced. Combustion reaction of remaining itaconic acid was not sufficient to generate sufficient heat to completely transform the metal hydroxides into their oxides.

Increased value of c/n = 0.9 caused the precursor gel to be decomposed repeatedly. The gel was initially decomposed at around 240 °C where at this temperature, ignition of NH_4NO_3 decomposition leads to the decomposition of itaconic acid together with Y, Ba and Cu nitrates. This reaction transformed most of these nitrates into Y_2O_3, $BaCO_3$ and CuO which was observed by large weight loss. However, the citric acid was not completely decomposed due to having higher volume (Li et al., 2007). Higher amount of citric acid yielded excess amount of aconitic acid. At the inner part of the gels, this aconitic acid was not fully decomposed to itaconic acid due to the difference in temperature gradient. The itaconic acid combustion propagation wave was stopped once it reached to the aconitic acid. The second decomposition reaction was occurred at 330 °C, once the aconitic acid was completely transformed to itaconic acid. The remaining nitrate gels were completely decomposed as this reaction produced much heat compare to the initial decomposition.

4.2 Structural properties of $YBa_2Cu_3O_{7-\delta}$

Figure 4.4 shows the XRD patterns of $YBa_2Cu_3O_{7-\delta}$ samples with different c/n. Vertical bars at bottom of the figure represent Bragg's diffraction angle of orthorhombic $YBa_2Cu_3O_7$ with lattice constants of a = 0.3877, b = 0.3827 and c = 11.6880 Å with *Pmmm* (47) symmetry. Each XRD pattern indicates the existence of polycrystalline $YBa_2Cu_3O_{7-\delta}$ phase. It can be observed that the XRD peaks for c/n = 0.6 and 0.7 samples were occurred at exact positions for standard $YBa_2Cu_3O_7$ phase. Few impurity peaks indicated by black dots in Figure 4.4 can be detected on XRD patterns of samples with c/n = 0.3, 0.5 and 0.9 where these peaks can be assigned to Y-Ba-O and Ba-Cu-O phases.

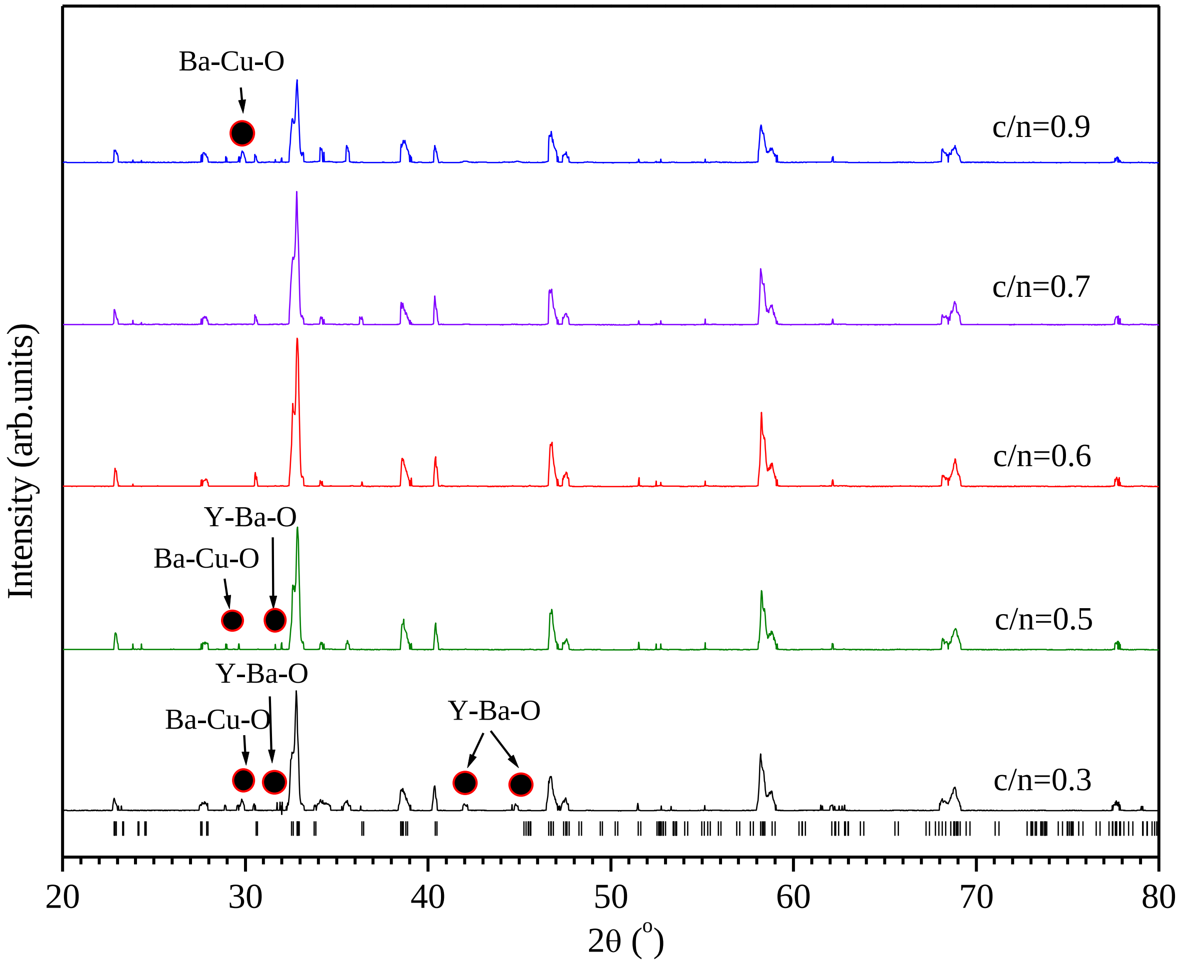

Figure 4.4: XRD patterns of $YBa_2Cu_3O_{7-\delta}$ samples after being calcined at 900 °C for 1h.

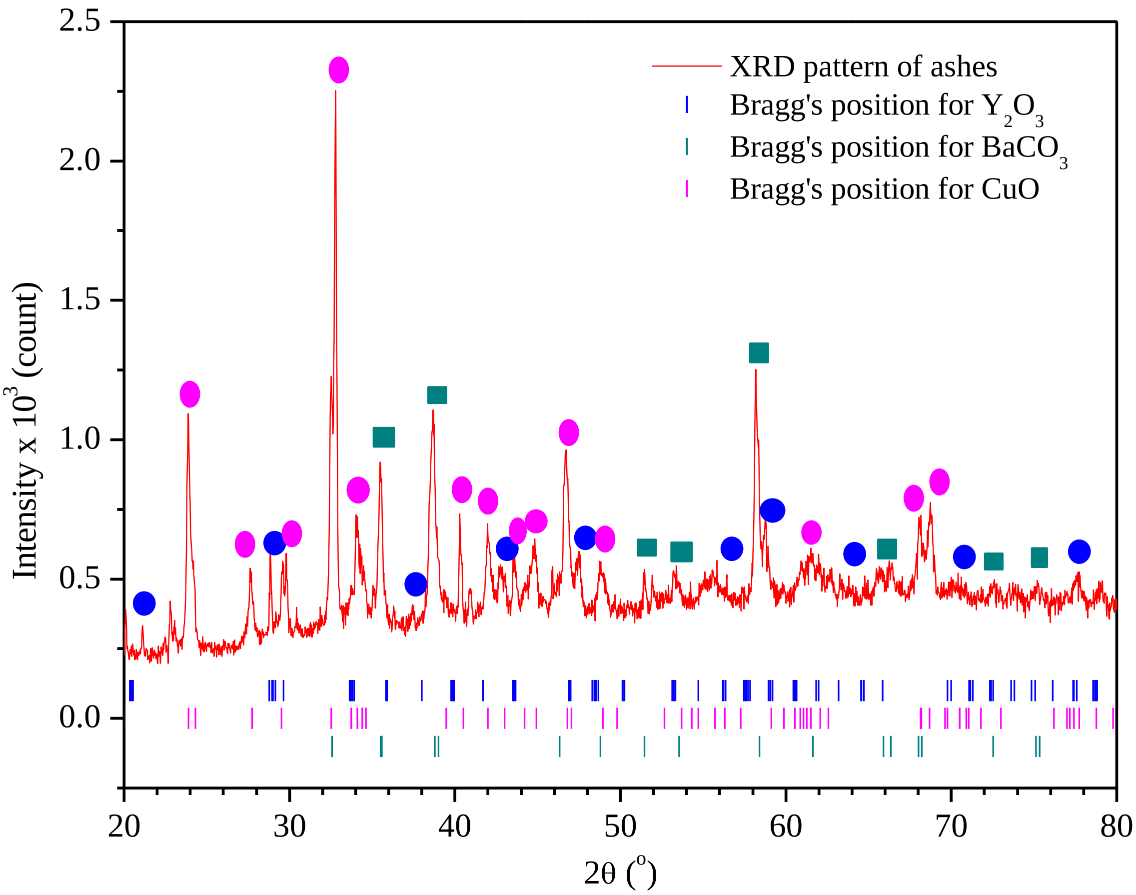

Figure 4.5: XRD pattern of ashes sample with c/n = 0.6 before calcination.

XRD pattern in Figure 4.5 revealed that the ashes sample had amorphous structure. It is believed that the ashes contained Y_2O_3, $BaCO_3$, and CuO as most of the peaks were assigned to Bragg's diffraction position of these compounds. These assigned peaks were indicated by green square, blue and pink dots for Y_2O_3, $BaCO_3$ and CuO compounds respectively. On the other hand, lot of un-assigned peaks in the figure indicates the existence of impurities which may be consisted of citrate ashes and un-decomposed matters. These impurities were eliminated during calcination process (Pathack et al., 2004); hence, produced highly crystalline and pure $YBa_2Cu_3O_{7-\delta}$ sample as depicted by XRD pattern in Figure 4.6.

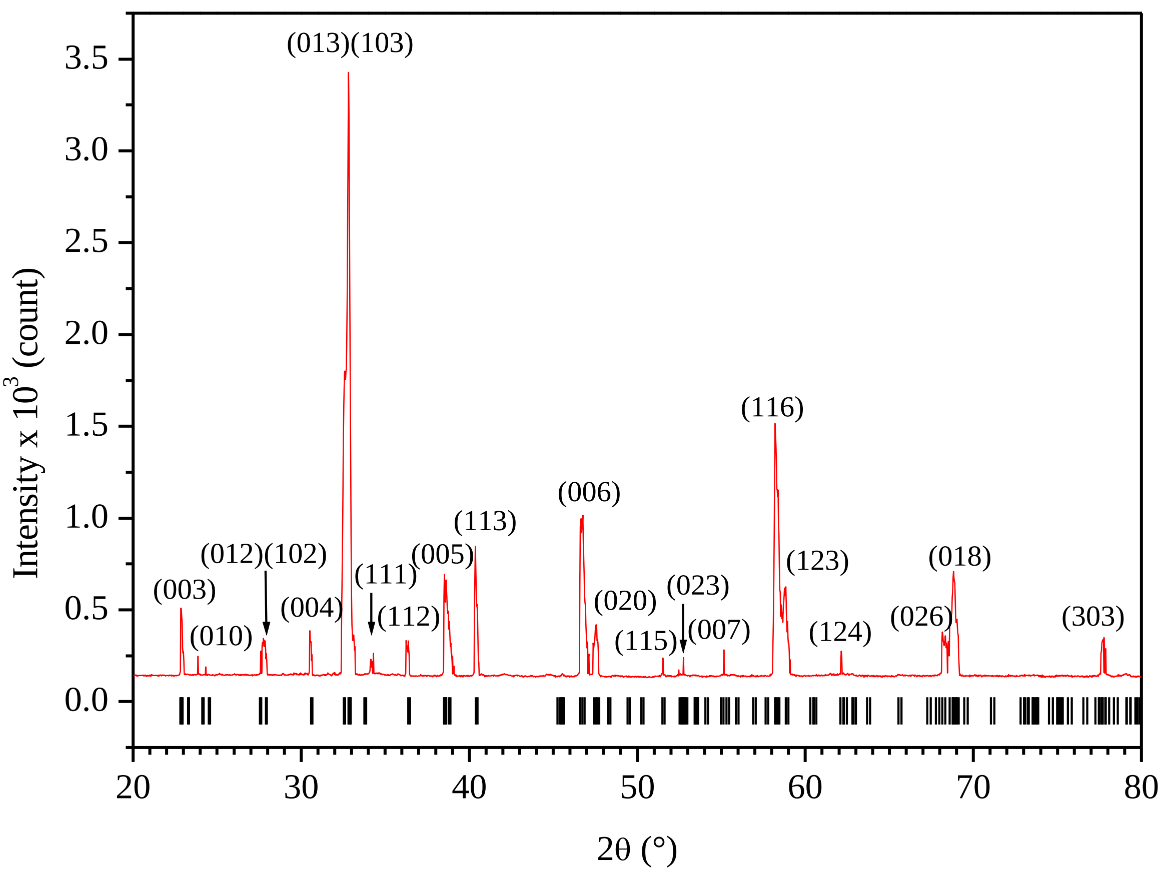

Figure 4.6: XRD pattern of powder sample with c/n = 0.6 after calcination.

Figure 4.6 revealed that the calcination process at 900 °C for 1 h is sufficient to yield high crystalinity in $YBa_2Cu_3O_{7-\delta}$ phase. The process is also able to eliminate the unwanted impurities in the ashes, thus, formed pure $YBa_2Cu_3O_{7-\delta}$ phase. The calcination process of involved reaction is shown in Equation (4.9).

$$Y_2O_3 + 4\ BaCO_3 + 6\ CuO \rightarrow 2\ YBa_2Cu_3O_{7-\delta} + CO + 3\ CO_2 \qquad (4.9)$$

From Equation (4.9), the purity of resultant $YBa_2Cu_3O_{7-\delta}$ powder is greatly depended on the amount (mol) of Y_2O_3, $BaCO_3$ and CuO in the ashes. As discussed in Section 4.1, expected moles of Y_2O_3, $BaCO_3$ and CuO ashes can only be achieved by the complete decomposition of Y, Ba, and Cu nitrates through rapid auto-combustion reaction. Thus, samples with c/n = 0.6 and 0.7 yielded highly pure of $YBa_2Cu_3O_{7-\delta}$ phase compare with other samples.

Existence of impurities in samples with c/n = 0.3, 0.5 and 0.9 is inevitable. This is due to pre and repeated decomposition of the nitrate gels which yields unbalanced amount of Y_2O_3, $BaCO_3$ and CuO in the ashes. The ashes produced from pre and repeated decomposition was transformed to Ba-Cu-O and Y-Ba-O compounds as the reactions shown in Equations (4.10) and (4.11) respectively.

$$3Y_2O_3 + 11BaCO_3 + 15CuO \rightarrow 5YBa_2Cu_3O_7 + 10CO_2 + CO + \text{Y-Ba-O} \tag{4.10}$$

$$2Y_2O_3 + 9BaCO_3 + 13CuO \rightarrow 4YBa_2Cu_3O_7 + 8CO_2 + CO + \text{Ba-Cu-O} \tag{4.11}$$

Figure 4.7 shows lattice constants of the samples. It can be observed that existence of impurity phases in samples with c/n = 0.3, 0.5 and 0.9 have significantly affected the lattice constants of $YBa_2Cu_3O_{7-\delta}$.

The *a* and *c* lattice constants of $YBa_2Cu_3O_{7-\delta}$ samples (Figure 4.7) were significantly changed as the c/n value was increased. However, the *b* lattice constant remained consistent at around 3.822 Å in all samples. It appeared that, the *a* lattice constant was reduced from 3.882 to 3.874 Å as the c/n was increased from 0.3 to 0.5. Then it was slowly increased by increasing the c/n and reached to the maximum value of 3.887 Å in c/n=0.9 sample. The characteristics of *c* lattice constant had a different behaviour. It can be clearly seen from Figure 4.7 that the *c* lattice was increased as the c/n was increased from 0.3 to 0.6. While at higher c/n, the *c* lattice constant was almost consistent at around 11.680 Å.

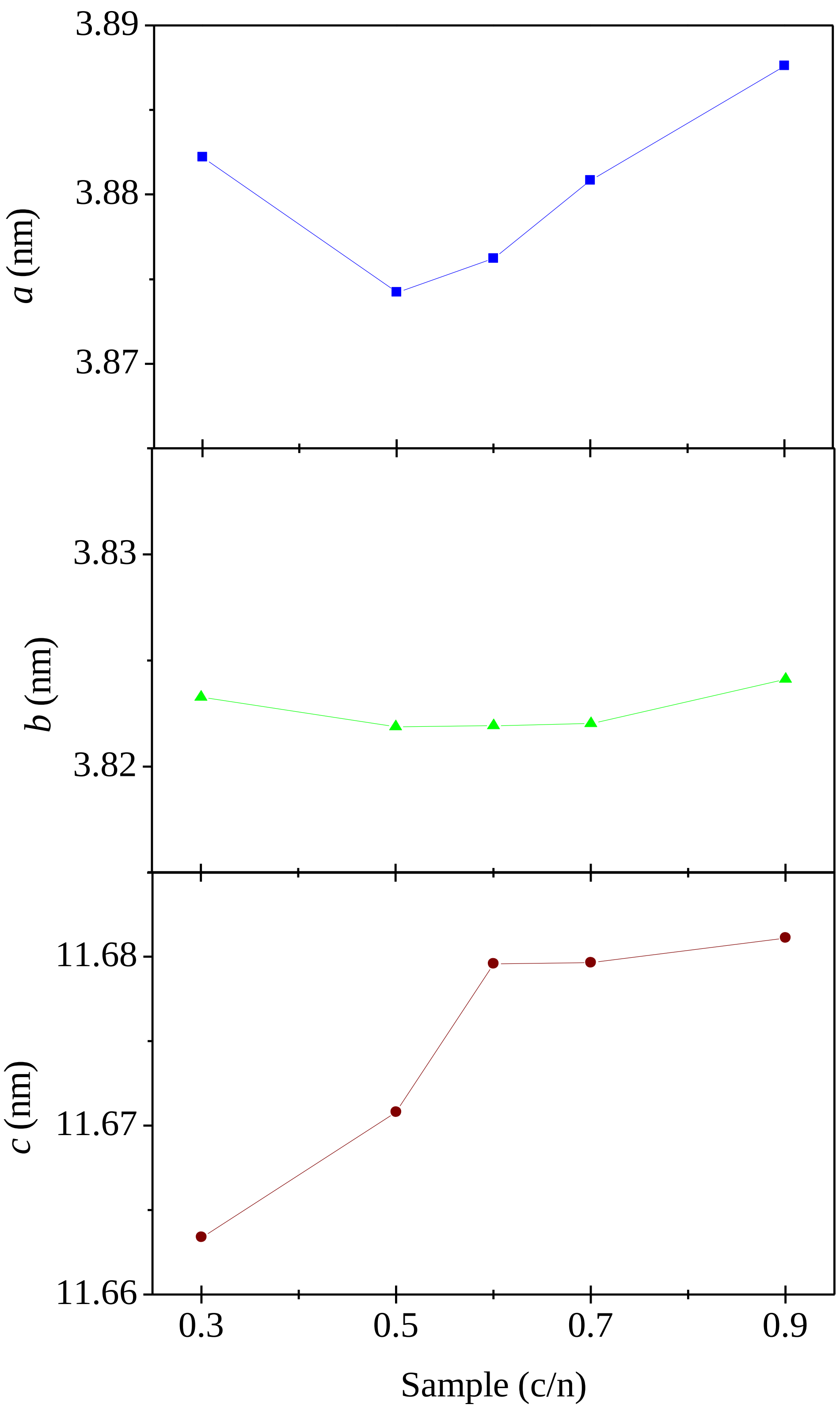

Figure 4.7: Lattice constants of $YBa_2Cu_3O_{7-\delta}$ samples for different c/n values.

Theoretically the *a* lattice constant of $YBa_2Cu_3O_{7-\delta}$ compound is controlled by the oxygen content (Cava et al., 1990). Hence, samples with c/n = 0.6 and 0.7 have smaller *a* lattice constant compare to the standard $YBa_2Cu_3O_7$ samples. This phenomenon was attributed from the higher oxygen deficiency in $YBa_2Cu_3O_{7-\delta}$. The samples with c/n = 0.3 and 0.9 however have larger *a* lattice constant and nearly equal with the standard $YBa_2Cu_3O_7$. The atomic number of oxygen in these samples is approached to seven. This means most of the oxygen sites in $YBa_2Cu_3O_{7-\delta}$ compound were occupied. Formation of Ba-Cu-O or Y-Ba-O compounds during calcination process altered the oxygen content of the $YBa_2Cu_3O_{7-\delta}$. Reoccupation of O sites by collecting oxygen from atmosphere could be a reason to form these impurities in the $YBa_2Cu_3O_{7-\delta}$ compound. Instead, the formation of smaller amount of impurities in samples with c/n = 0.5, the oxygen reserved for the formation of $YBa_2Cu_3O_{7-\delta}$ was consumed and resulted lower *c* lattice constant.

Consistency of *b* lattice constant in all samples was due to proper arrangement of copper in $YBa_2Cu_3O_{7-\delta}$ (Cava et al., 1990). Cu^{2+} ion from the CuO ashes had higher tendencies to occupy at preferably sites in $YBa_2Cu_3O_{7-\delta}$ during calcination. Hence, the *b* lattice constant was not varied in all samples.

Difference in *c* lattice constant of $YBa_2Cu_3O_{7-\delta}$ was determined by the Y sites (Zhang et al., 1995). The *c* lattice constant of samples with c/n = 0.6, 0.7 and 0.9 was nearly same with the standard $YBa_2Cu_3O_7$ sample due to full occupancy of the Y sites. As for samples with c/n = 0.3 and 0.5, the *c* lattice constant was reduced because of the existence of Y-Ba-O compound which lowered the presence of Y at it respective sites.

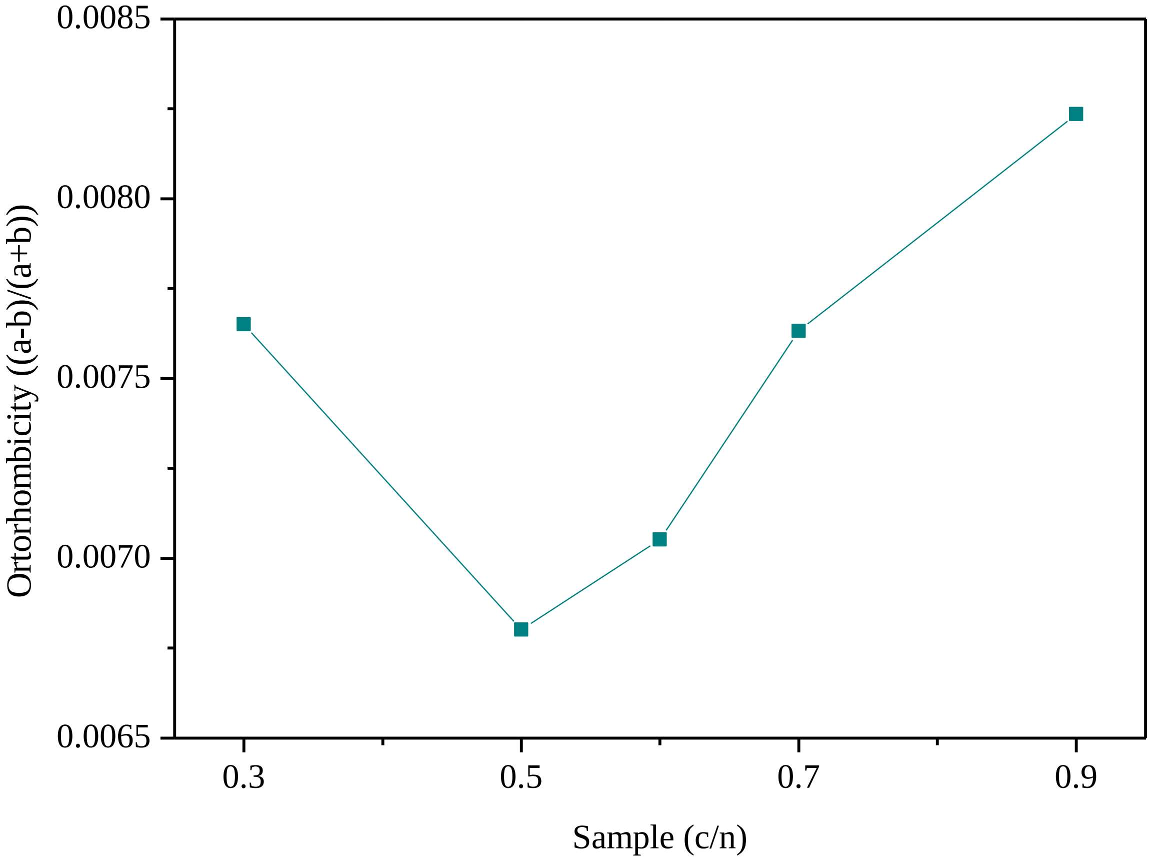

Figure 4.8: Orthorhombicity of $YBa_2Cu_3O_{7-\delta}$ samples for different c/n values.

Figure 4.8 shows the orthorhombicity of $YBa_2Cu_3O_{7-\delta}$ samples obtained from the *a* and *b* lattice constants using Equation (4.12).

$$\text{Orthorhombicity} = (a\text{-}b)/(a+b) \tag{4.12}$$

It appeared that all samples sustained it orthorhombic structure though prepared from different c/n ratios. The orthorhombicity value of $YBa_2Cu_3O_{7-\delta}$ samples was observed to be changed in similar pattern as the *a* lattice constant varied with c/n ratio. In sample with c/n = 0.3, the orthorhombicity was 0.0077. It was suddenly reduced in sample with c/n = 0.5 and then slowly increased in samples with c/n=0.6, 0.7 and 0.9.

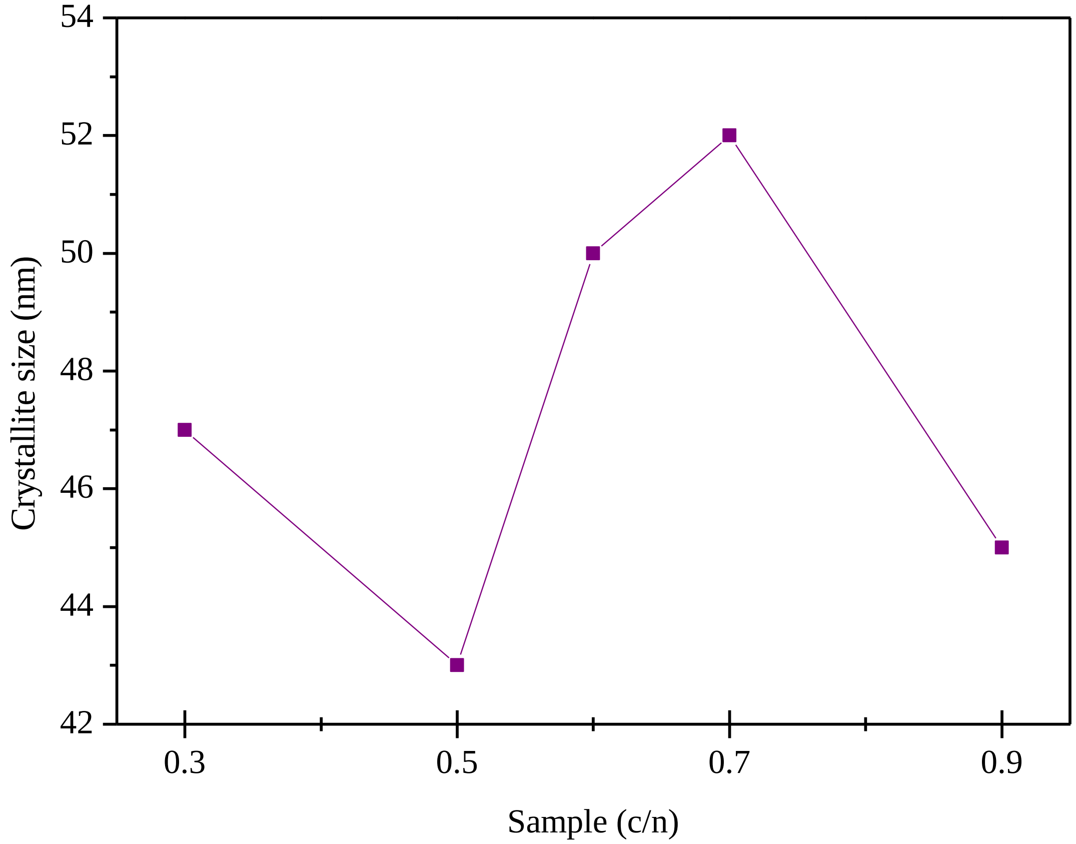

Figure 4.9: Crystallite sizes of $YBa_2Cu_3O_{7-\delta}$ samples for different c/n value.

The crystallite size of the $YBa_2Cu_3O_{7-\delta}$ samples were calculated from the Debye-Sherer formula (Equation 3.4) and shown in Figure 4.9. It can be observed that the crystallite size of all samples was below 100 nm which is in agreement with Xu et al., (2002). The smallest crystallite size was 43 nm obtained from the sample with c/n = 0.5 while the largest crystallite size was 52 nm for the sample with c/n = 0.7. Crystallite size of calcined $YBa_2Cu_3O_{7-\delta}$ powder was dependent on the starting ashes. Rapid decomposition reaction produced finer ash which upon calcination reacted quickly due to having larger reaction surface to nucleated $YBa_2Cu_3O_{7-\delta}$. The growth and densification process of the nucleus to form grains occurred over the span of sufficient period of time (Shi et al., 2005). Therefore large crystallite size was produced in samples with c/n = 0.6 and 0.7. The ashes produced after pre and repeated combustion reaction however were slightly larger. In addition, more heat was consumed in the reaction to produce impurities; hence, the grain growth rate was slower in $YBa_2Cu_3O_{7-\delta}$.

4.3 Microstructure and elemental analysis of $YBa_2Cu_3O_{7-\delta}$

The FESEM images of as-prepared pellet samples with c/n = 0.3, 0.5, 0.6, 0.7 and 0.9 are shown in Figures 4.10 – 4.14 respectively.

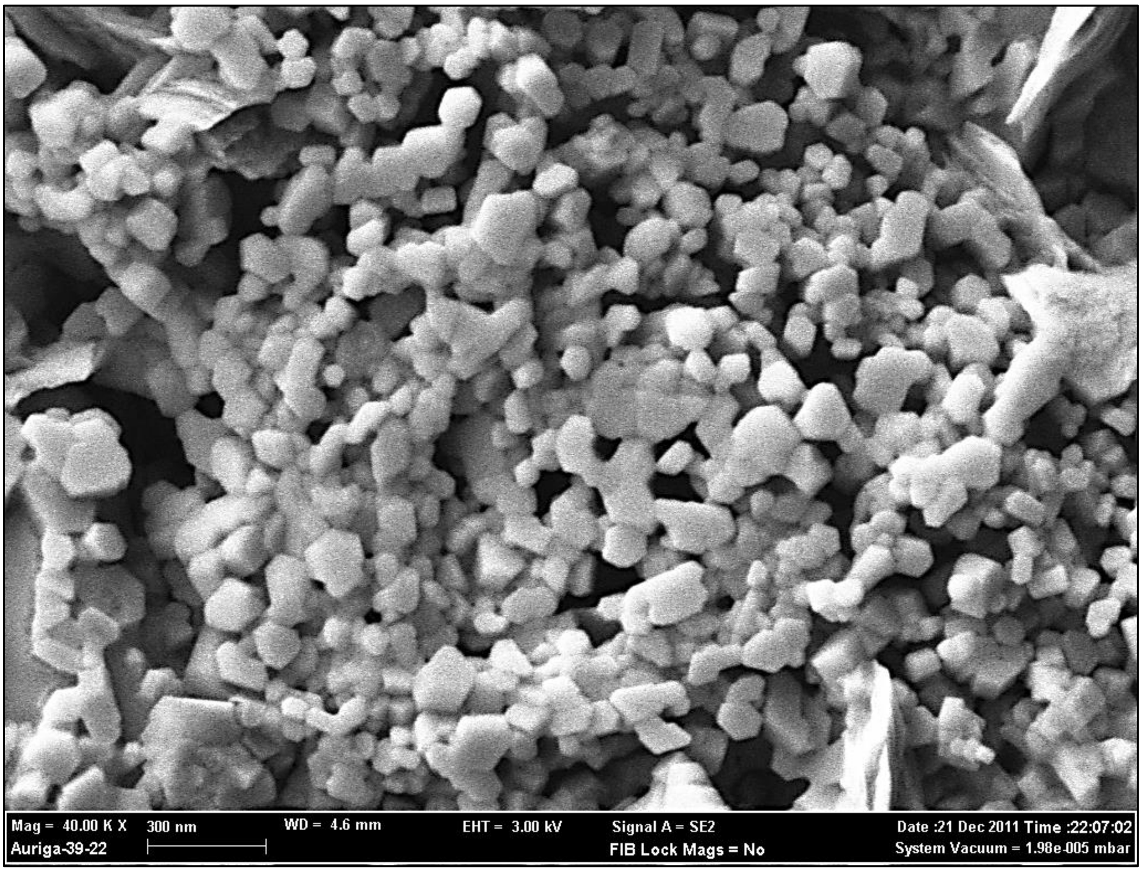

Figure 4.10: FESEM image of the sample with c/n = 0.3.

It is observed that the microstructure of sample with c/n = 0.3 shown in Figure 4.10 was consisted of distinct $YBa_2Cu_3O_{7-\delta}$ particles and pores. It appeared that, the grains of $YBa_2Cu_3O_{7-\delta}$ was just started to grow during heat treatment process. These grains were constructed of particulates with sharp edges having sizes ranged from 50 to 200 nm. Variation of particle sizes and shapes developed large gap between the particles which appeared as pores in Figure 4.10. This structure resulted in lower connectivity between particles.

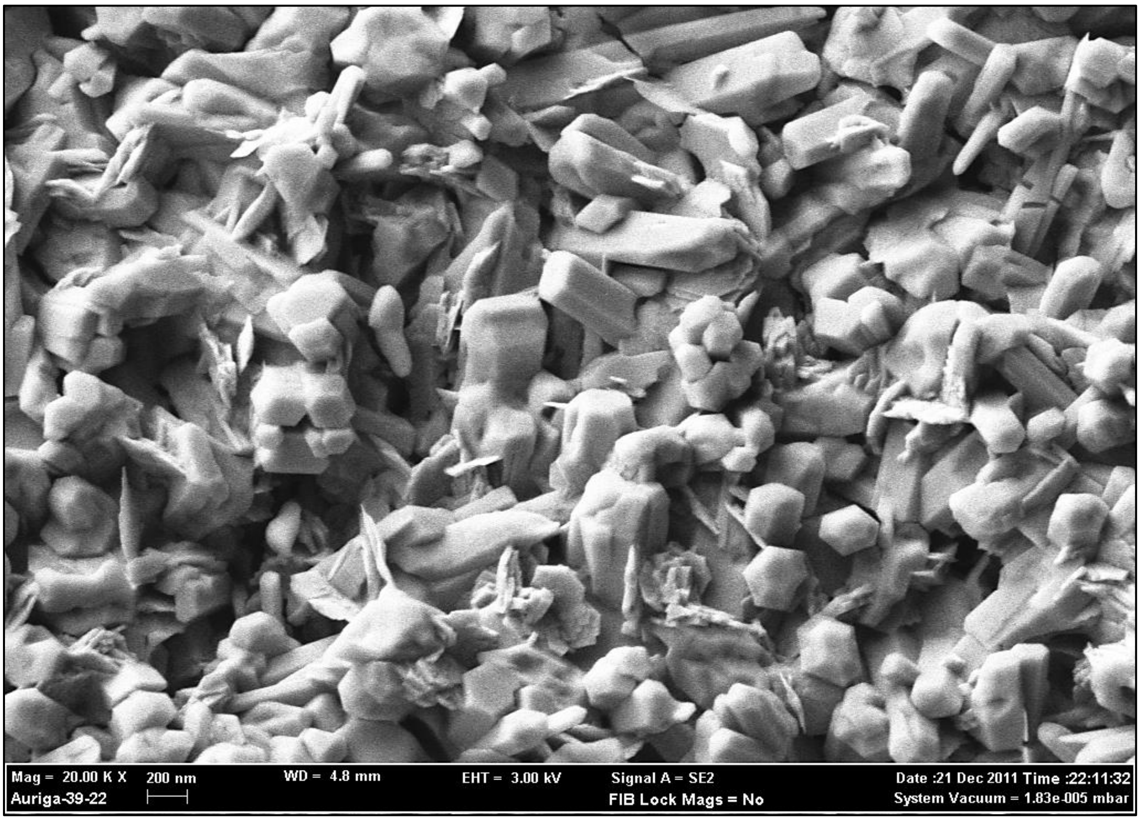

Figure 4.11: FESEM image of the sample with c/n = 0.5.

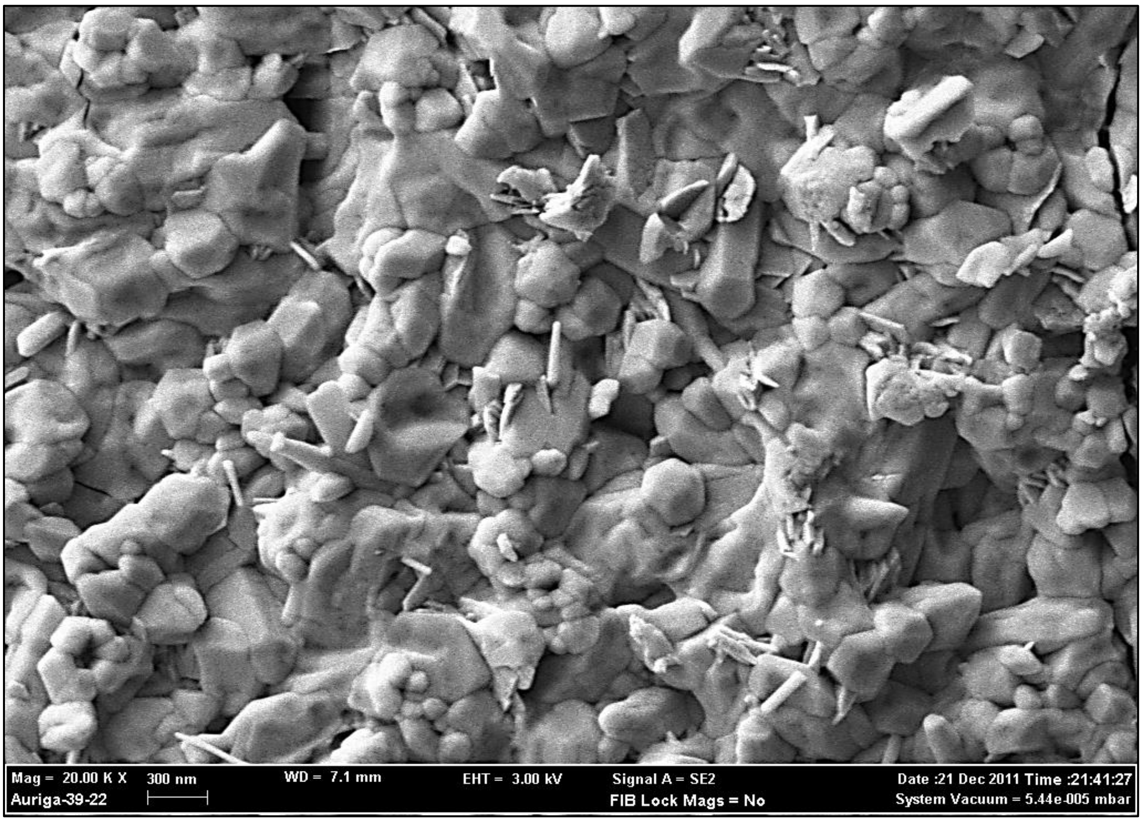

Figure 4.12: FESEM image of the sample with c/n = 0.6.

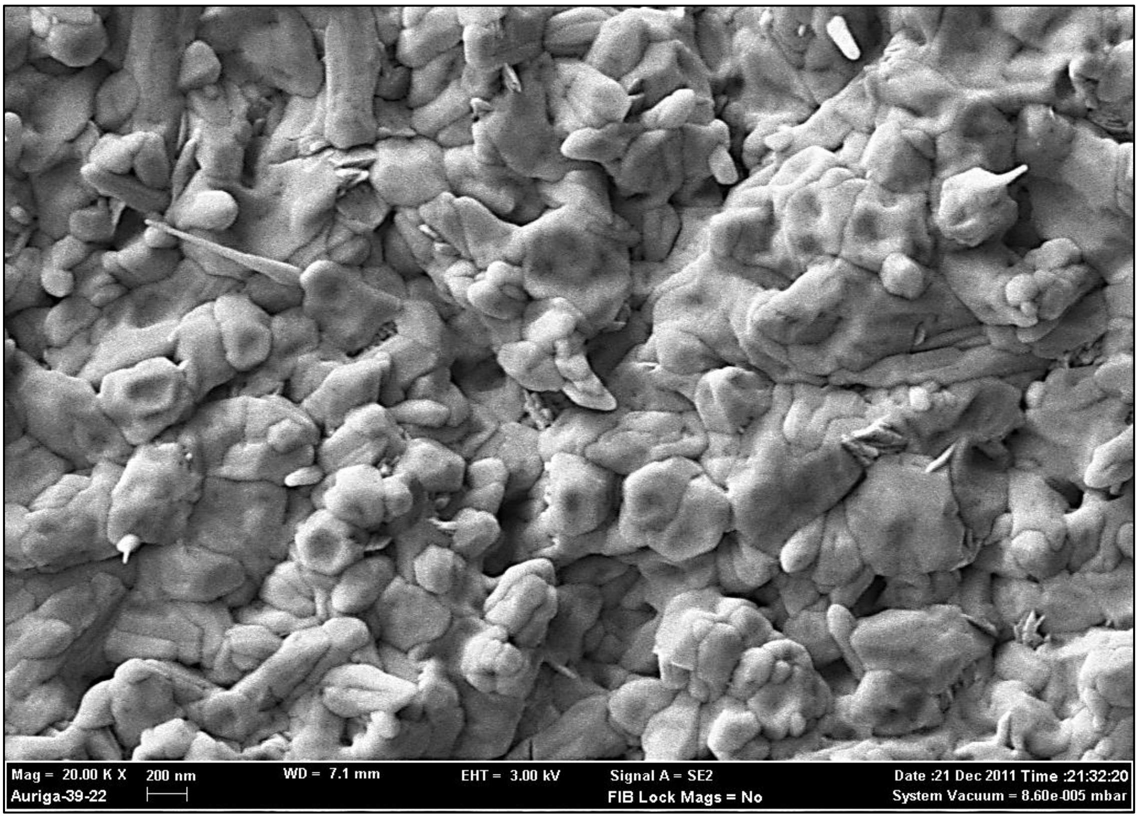

Figure 4.13: FESEM image of the sample with c/n = 0.7.

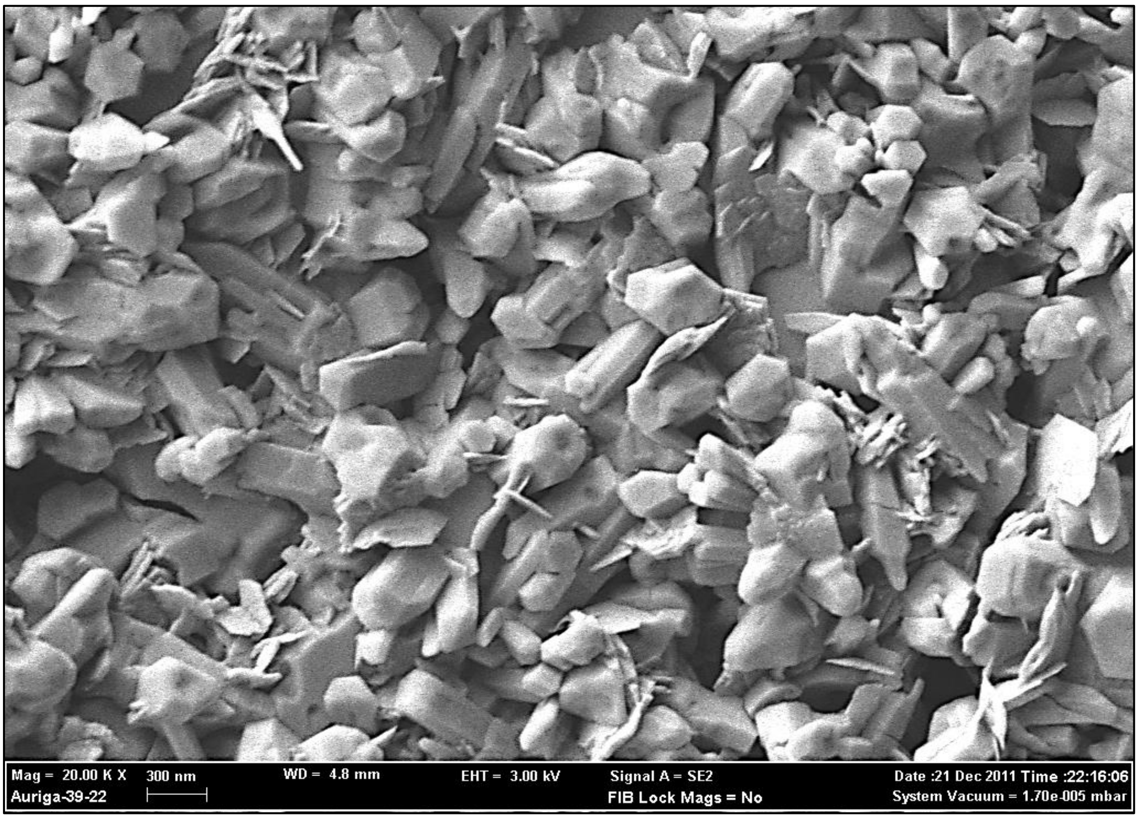

Figure 4.14: FESEM image of the sample with c/n = 0.9.

Samples with c/n = 0.5 and 0.9 shown in Figures 4.11 and 4.14 comprised of orthorhombic shape with larger particles and denser microstructure of $YBa_2Cu_3O_{7-\delta}$ compared to other samples. This is due to the continuous growth of $YBa_2Cu_3O_{7-\delta}$ grain during calcination followed by heat treatment. Each particle was observed to have even shape with sizes ranged from 100 to 300 nm. This type of structure was believed to have better connectivity compared to sample with c/n = 0.3 due to low existence of pores.

While samples with c/n = 0.6 and 0.7 presented in Figures 4.12 and 4.13 respectively have melted-like microstructure though $YBa_2Cu_3O_{7-\delta}$ particles are distinguishable. No pores were observed in these samples because the grains of $YBa_2Cu_3O_{7-\delta}$ were continued to grow and filled the gap between the particles. Particle sizes of all samples were in the ranged of 50 to 350 nm. It appeared that the size of the particles of all samples obtained from the FESEM images was larger than the crystallite size calculated from the XRD. This phenomenon indicates that each particle was consisted of several crystals.

Figure 4.15 shows the EDX spectra of all samples. It confirms that all samples constituted of Y, Ba, Cu and O. Existence of carbon (C) in EDX spectra was attributed from the carbon tape of the sample holder; hence, it can be neglected. The atomic number of each element in each sample is listed in Table 4.2. From the atomic ratio of all samples, it is proven that samples with c/n = 0.6 and 0.7 were yielded as pure $YBa_2Cu_3O_{7-\delta}$ compound. This is in good agreement with the XRD data. While the existence of excess Y, Ba and Cu in samples with c/n = 0.3 and 0.5 is the evidence of the presence of Y-Ba-O and Ba-Cu-O impurities. The Ba-Cu-O impurity was also apparent in sample with c/n = 0.9 as the ratio of Ba was exceeded the expected value.

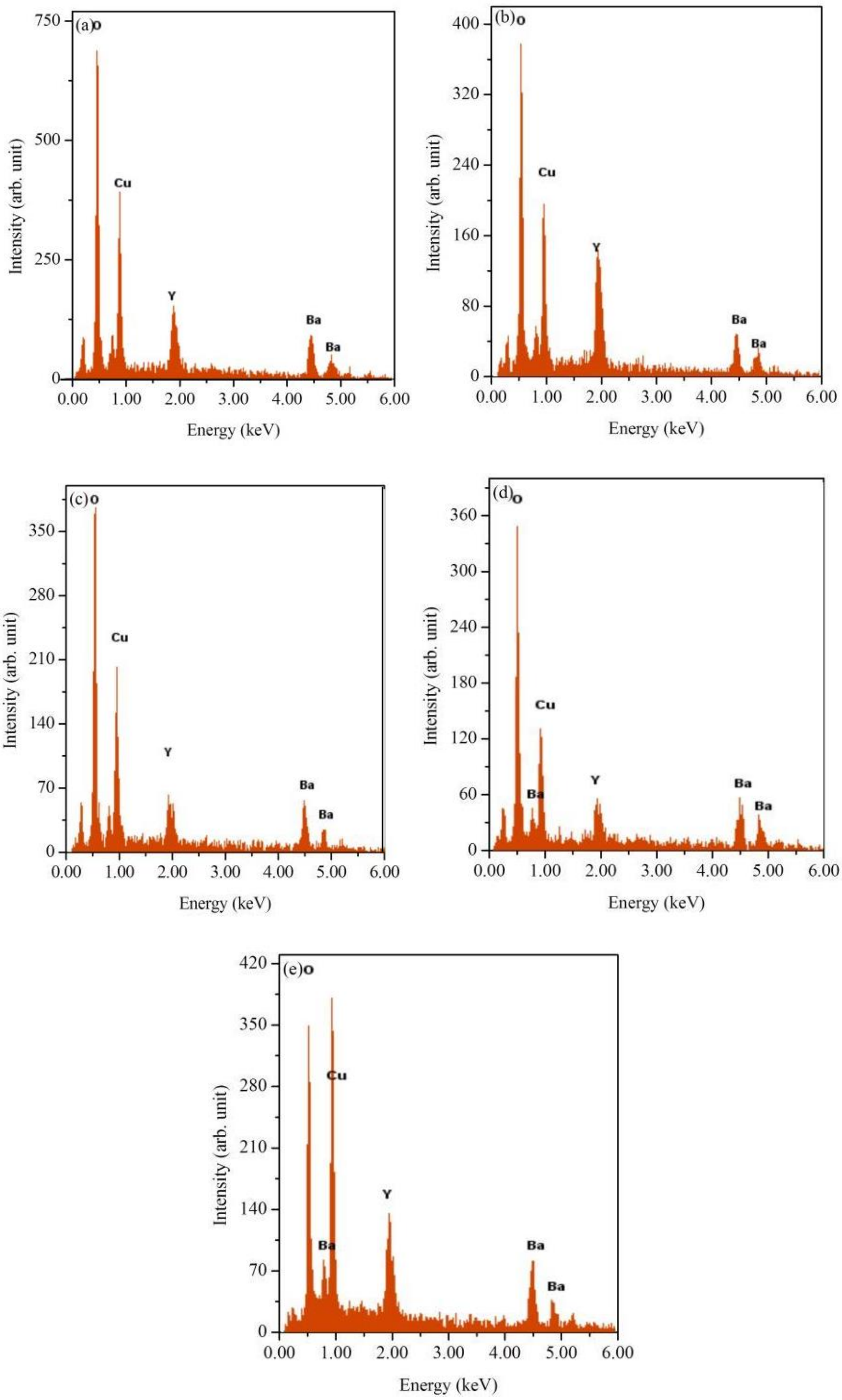

Figure 4.15: EDX spectra of samples for different values of c/n; (a) 0.3, (b) 0.5, (c) 0.6, (d) 0.7 and (e) 0.9.

Table 4.2: Atomic numbers and ratio of the elements obtained from EDX analysis of the $YBa_2Cu_3O_{7-\delta}$ for different c/n values.

Sample (c/n)	Atomic (at. %)				Atomic Ratio
	Y	Ba	Cu	O	Y:Ba:Cu
0.3	11.27	14.13	17.66	56.93	1:1.25:1.57
0.5	11.75	13.51	18.07	58.67	1:1.15:1.54
0.6	8.37	16.83	24.38	51.02	1:2.01:2.91
0.7	8.20	16.45	24.67	50.67	1:2:3.
0.9	6.89	16.95	19.12	57.04	1:2.46:2.78

4.4 Critical temperature (T_C) analysis

Figure 4.16 shows the temperature dependence of electrical resistivity for $YBa_2Cu_3O_{7-\delta}$ samples with different c/n values. It is seen from this figure, the resistivity of each sample was reduced to zero by different behavior. The resistivity was decreased and stabilized before abruptly reduced to zero in c/n = 0.3 and 0.5 samples. At temperature above the T_C, the relation between resistivity and temperature of these samples was more likely normal metallic behavior as suggested by BCS theory (Roslan, 2004). Instead, samples with c/n = 0.6, 0.7 and 0.9 were behaved like semiconductor as the resistivity was consistently decreased and then rapidly dropped to zero at the T_C.

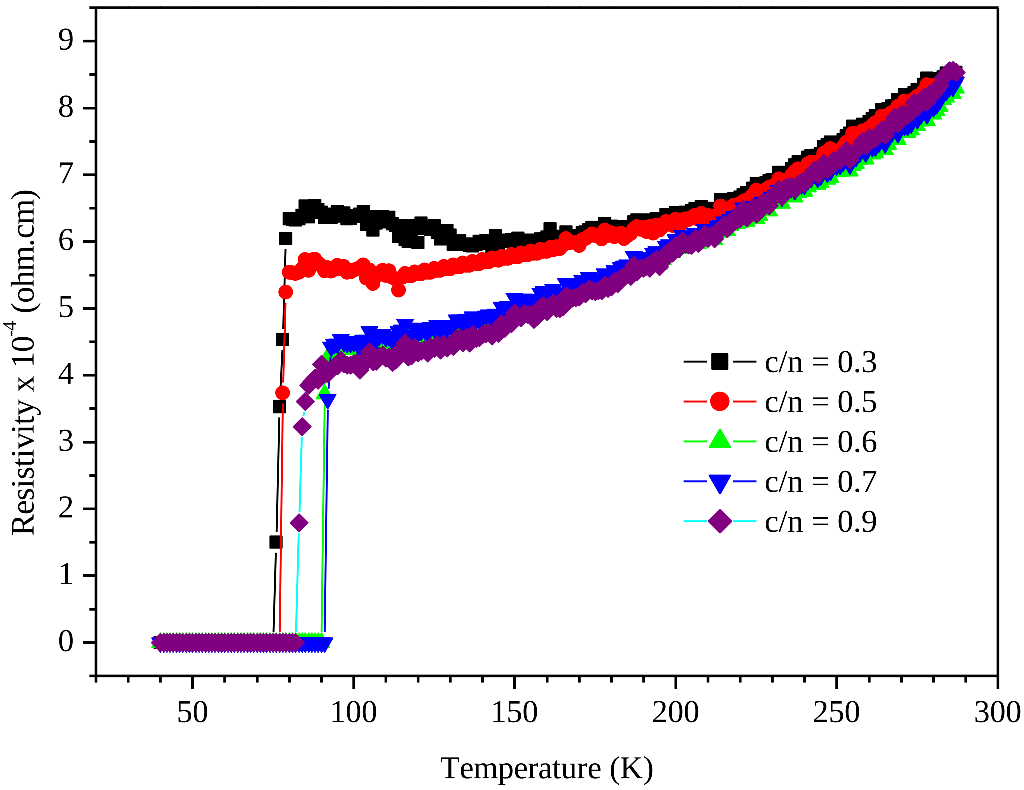

Figure 4.16: Temperature dependence resistivity of $YBa_2Cu_3O_{7-\delta}$ samples with different c/n values.

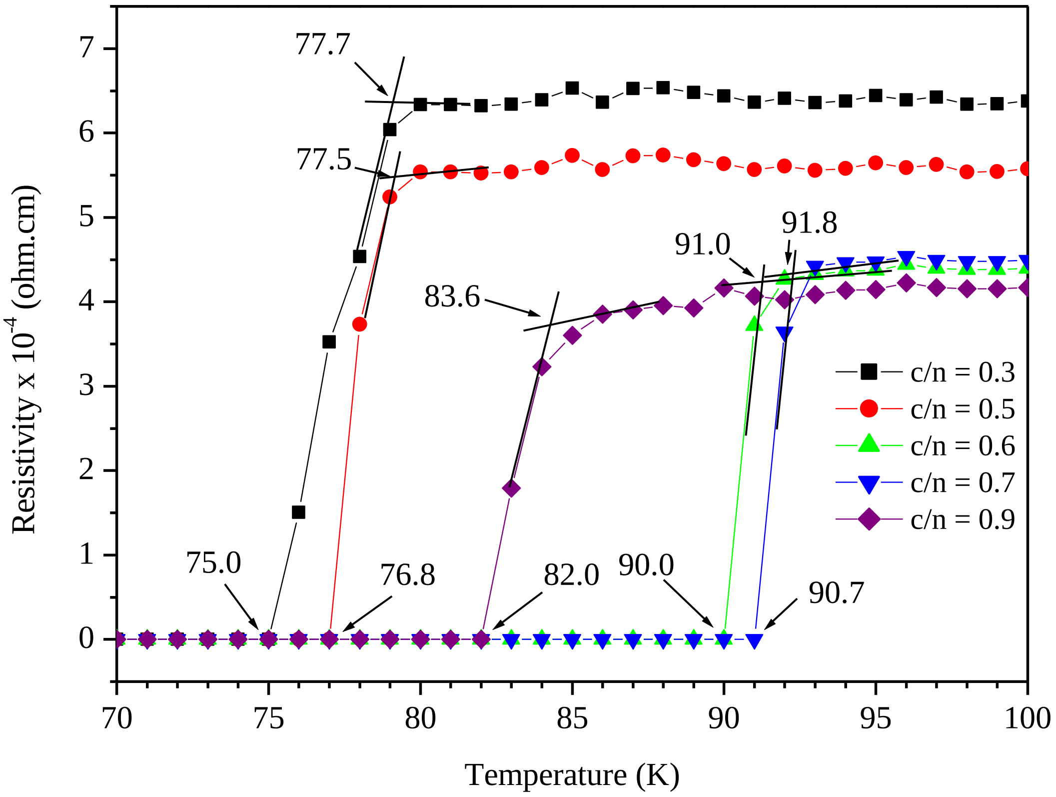

Figure 4.17: The T_C onset and T_C zero of the $YBa_2Cu_3O_{7-\delta}$ samples with different c/n values.

In Figure 4.17, T_C onset and T_C zero values of the samples are signified by black and blue arrows respectively. The T_C onset was increased from 77.5 to 91.8 K as c/n was increased from 0.3 to 0.7. On the other hand, T_C onset was decreased to 83.6 K in sample with c/n = 0.9. The T_C zero of the samples was also varied by the same pattern. It occurred that the transition widths were 2.7, 0.7, 1.0, 1.1 and 1.6 K for samples with c/n = 0.3, 0.5, 0.6, 0.7 and 0.9 respectively. Narrow transitions widths of each sample indicate that each sample were highly homogeneous (Erb et al., 1998). The highest T_C zero was achieved in sample having c/n = 0.7 followed by the sample having c/n = 0.6. This was due to high purity of $YBa_2Cu_3O_{7-\delta}$ with oxygen deficiencies at around 0.2. Existence of non-superconducting Y-Ba-O and Ba-Cu-O impurities in samples having c/n = 0.3, 0.5 and 0.9 obstructed superconducting current to flow at T_C zero for typical $YBa_2Cu_3O_{7-\delta}$ superconductor.

4.5 Discussions

The $YBa_2Cu_3O_{7-\delta}$ sample with c/n = 0.7 was found to have the best properties compare to other samples. Rapid decomposition of the gel occurred during auto-combustion reaction produced expected moles of Y_2O_3, $BaCO_3$ and CuO intermediate ashes. During calcination process, these intermediate ashes were reacted to form high purity $YBa_2Cu_3O_{7-\delta}$ compound. No impurity phase was detected in this sample as confirmed by elemental ratio. The crystallite and particle size of this sample was 52 nm and 100 nm, respectively. This sample possessed orthorhombicity of 0.0071 and the oxygen content was expected around 6.8. This sample exhibited T_C zero of 91.8 K with a significant sharp transition width which is greatly similar with pure $YBa_2Cu_3O_{7-\delta}$ superconductor reported by Wu et al. (1987), Xu et al. (2002) and Pathack et al. (2004).

The c/n = 0.6 was closest value to give stoichiometric reaction and produced the same properties of $YBa_2Cu_3O_{7-\delta}$ as the sample having c/n = 0.7. However, the concentration of citric acid was just sufficient with the concentration of nitrates gel and only relevant to synthesize $YBa_2Cu_3O_{7-\delta}$. Therefore, the auto-combustion reaction must be carefully controlled to avoid any loss of citric acid.

Instead, samples having c/n = 0.3, 0.5 and 0.9 were not able to synthesize highly pure $YBa_2Cu_3O_{7-\delta}$ sample. The decomposition reaction of the gels was occurred in many steps which yielded un-balanced mole of intermediate ashes which is in agreement with by Li et al. (2009). This produced impurities in these samples which resulted in the reduction of T_C.

CHAPTER 5

EFFECTS OF THE ADDITION OF Al_2O_3 NANOPARTICLES

In this chapter, the effects of the addition of $Al(NO_3)_3$ on decomposition characteristics of gel samples having c/n = 0.7 are studied. The structural, mechanical, superconducting and magnetic properties of Al_2O_3 added $YBa_2Cu_3O_{7-\delta}$ samples are thoroughly discussed.

5.1 Decomposition characteristics analysis

Decomposition characteristic of gel samples having x_{mol} = 0.00 and 0.02 are depicted by DTA and TG curves as shown in Figures 5.1 and 5.2, respectively.

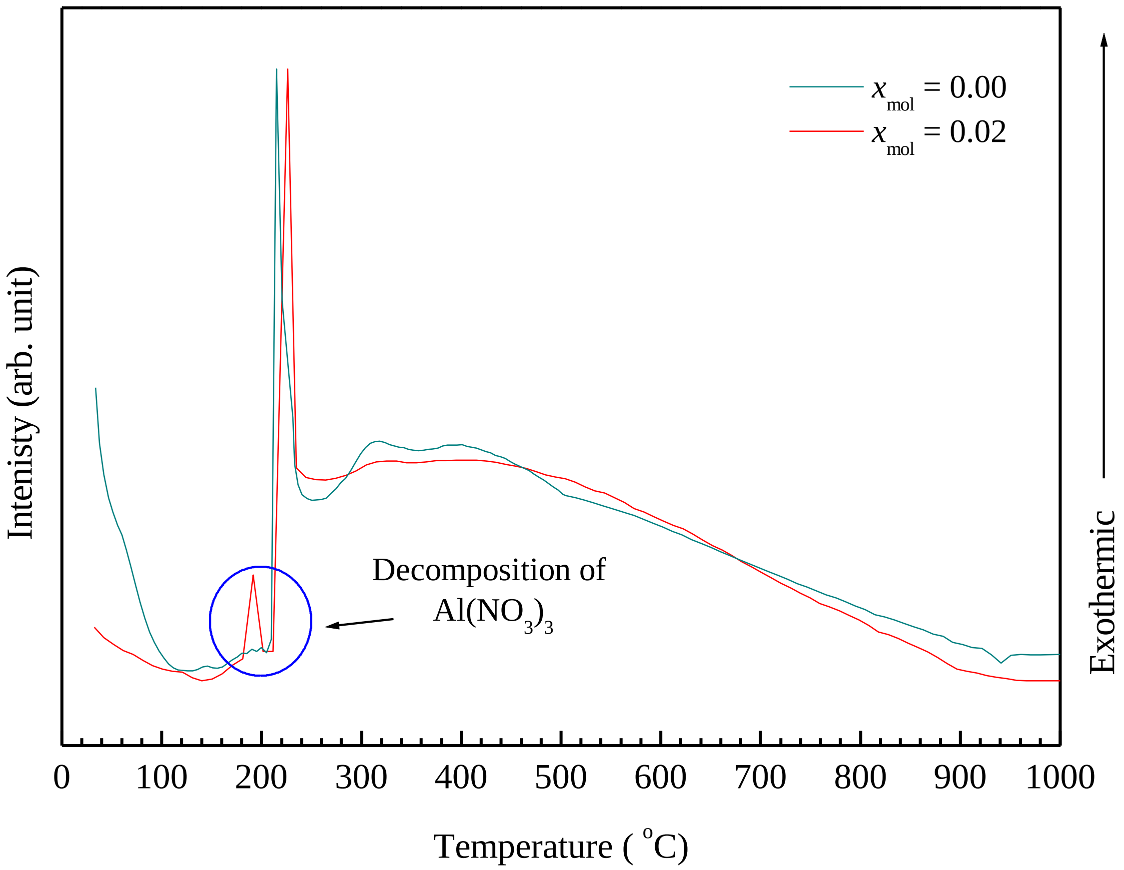

Figure 5.1: DTA curves of gel samples having x_{mol} = 0.00 and 0.02.

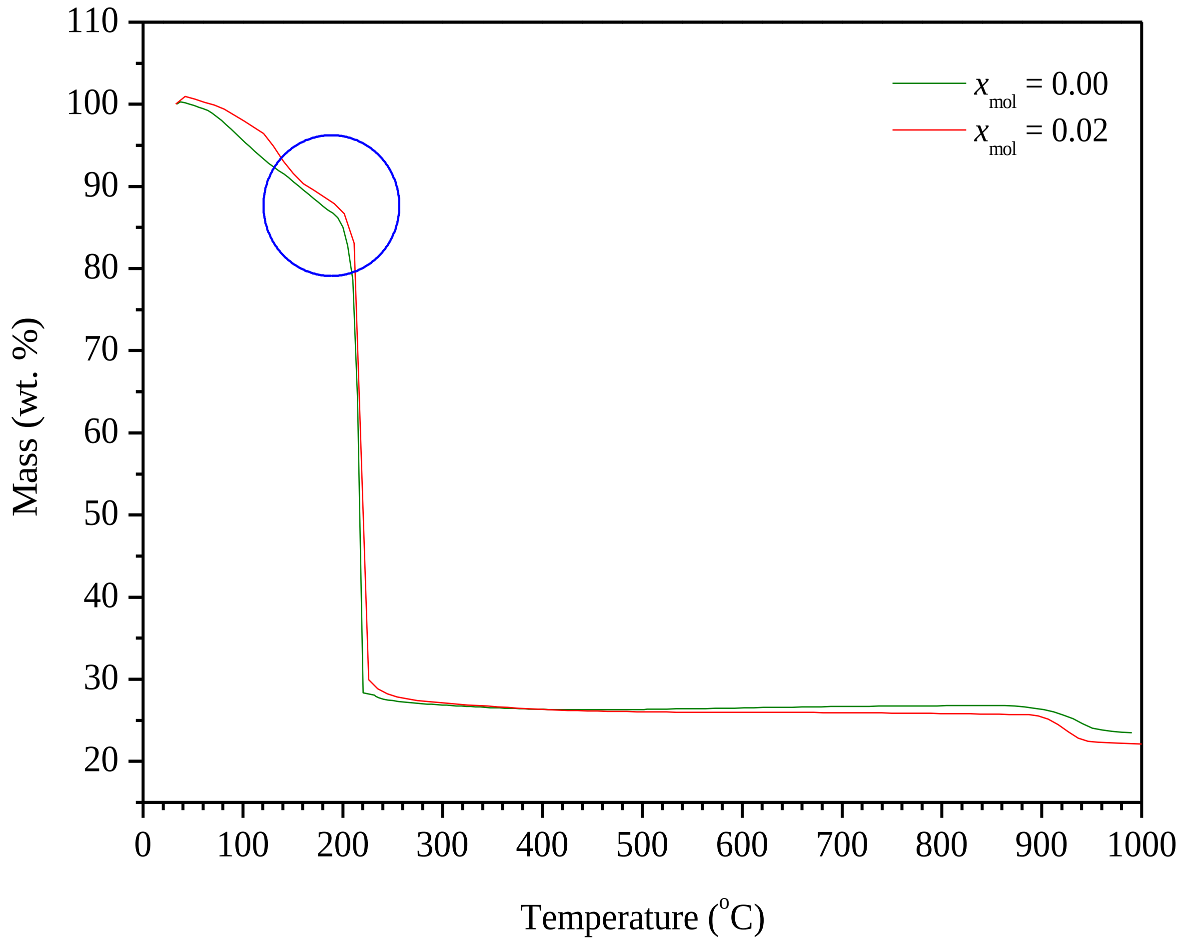

Figure 5.2: TG curves of gel samples having x_{mol} = 0.00 and 0.02.

Figure 5.1 shows a strong exothermic peak which occurred at around 220 °C for both samples. Furthermore, an additional exothermic peak was detected at 190 °C for gel sample having x_{mol} = 0.02. This relatively small peak is indicated by a circle on the figure. The TG curve of the gel sample having x_{mol} = 0.00 shows a reduction of mass at temperature range of 30 to 220 °C before rapid drop at around 230 °C (Figure 5.2). Then the sample was thermally stabilized until a small drop of mass was seen at 900 °C. On the other hand, an anomaly drop of mass was seen in TG curve at around 190 °C for gel sample with x_{mol} = 0.02. This anomaly is signified by a circle in the figure. Then the TG curve of this sample was sharply dropped at around 220 °C and stabilized until 900 °C followed by a minor drop.

By referring to the TG and DTA patterns, it appeared that the gel sample without Al_2O_3 nanoparticles (x_{mol} = 0.00) was decomposed by rapid decomposition reaction. As discussed in Chapter 4, mass of the gel sample was constantly dropped at temperature ranging from 30 to 220 °C by the dehydration of moisture. Decomposition of Y, Ba and Cu nitrate gel to Y_2O_3, $BaCO_3$ and CuO was occurred in a single step reaction as indicated by a sharp fall in mass followed by a strong exothermic peak occurred at 220 °C. The thermally stable plateau between 230 and 900 °C indicated the formation of a stable intermediate product. A small drop of mass at around 900 °C signified the formation of $YBa_2Cu_3O_{7-\delta}$.

The $Al(NO_3)_3$ added gel sample with x_{mol} = 0.02 was initially decomposed (additional step) at around 190 °C. This additional step was attributed due to the decomposition reaction of $Al(NO_3)_3$ to Al_2O_3 as suggested by Li et al. (2007). It is worth to mention that this peak was not presented in the DTA curve of gel sample having no Al_2O_3 nanoparticles (x_{mol} = 0.00). The gel lose was about 4 wt. % of mass during this reaction. Reaction between $Al(NO_3)_3$ and NH_4OH generated small fraction of NH_4NO_3 as shown in Equation 5.2. Thus the heat generated upon decomposition of NH_4NO_3 was minor and just enough to transform $Al(OH)_3$ to Al_2O_3. This reaction was indicated by the lower intensity of the exothermic peak at around 190 °C. Following the Pederson's reaction model, the reaction is shown in Equation (5.1).

$$6Al(NO_3)_3 + 5C_6H_8O_7 \rightarrow 3Al_2O_3 + 10H_2O + 9N_2 + 25CO_2 \qquad (5.1)$$

The main decomposition of Y, Ba and Cu nitrate gel was occurred at 226 °C after this reaction. Both decomposition reactions were occurred at different temperature for different composition of $Al(NO_3)_3$ as shown in Figure 5.3.

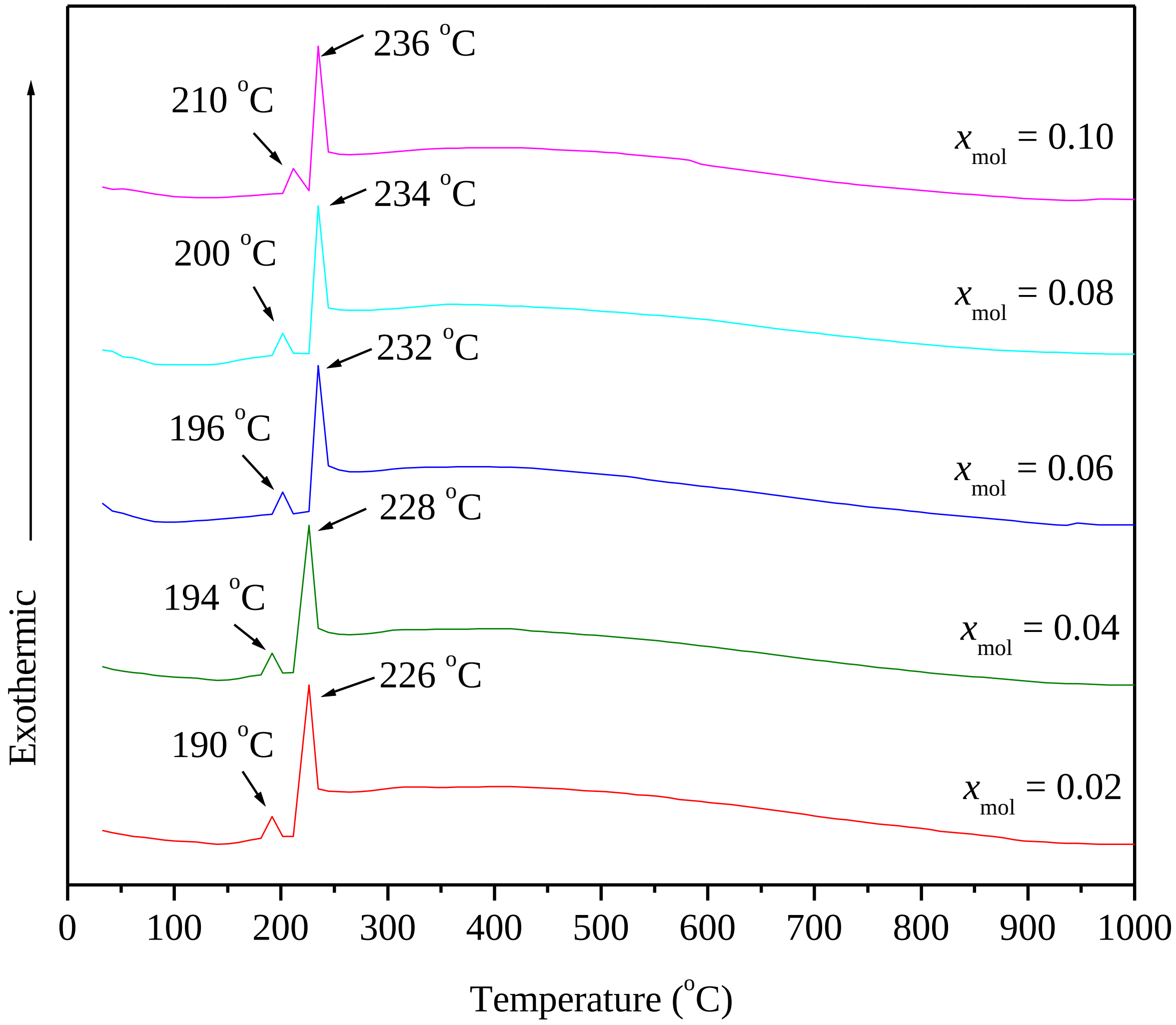

Figure 5.3: DTA curves of $Al(NO_3)_3$ added gel samples.

Figure 5.3 shows the DTA curves of the gel samples with different $Al(NO_3)_3$ composition. Each curve had two significant exothermic peaks. The first exothermic peak was occurred at temperature range of 190 to 210 °C while the second peak was occurred at temperature range of 226 to 236 °C. The intensity of the first peak was relatively small compare to the second peak and the intensity was increased with the addition of $Al(NO_3)_3$. However, the intensity of the second exothermic peak was decreased with the addition of $Al(NO_3)_3$ in the gel sample.

Meanwhile, the first exothermic peak was shifted from 190 – 194 °C, 194 –196 °C, 196 – 200 °C, and 200 – 210 °C for the addition of x_{mol} = 0.02, 0.04, 0.6, 0.08 and

0.10, respectively. While the second exothermic peak was shifted from 226 –228 °C, 228 –232 °C, 232 – 234 °C, and 234 – 236 °C for the addition of x_{mol} = 0.02, 0.04, 0.6, 0.08 and 0.10, respectively.

The first exothermic peak indicated the decomposition reaction of $Al(NO_3)_3$. Upon increasing the amount of $Al(NO_3)_3$ in the gel samples, the exothermic temperature and intensity of the peak was increased. This is much depended on the reaction between $Al(NO_3)_3$ and NH_4OH as shown in Equation (5.2).

$$Al\ (NO_3)_3 + NH_4OH \rightarrow Al(OH)_3 + NH_4NO_3 \qquad (5.2)$$

$$2\ Al\ (OH)_3 \rightarrow Al_2O_3 + 3H_2O \qquad (5.3)$$

It appeared that the gel sample with higher $Al(NO_3)_3$ addition generated higher amount of NH_4NO_3 which then deliberated more heat during decomposition reaction. Therefore gel sample with x_{mol} = 0.10 has the most intense exothermic peak compared with other samples. Moreover, decomposition reaction of higher amount of generated NH_4NO_3 required higher temperature thus the exothermic peak was shifted to be occurred at higher temperature. The generated heat is just sufficient to transform $Al(OH)_3$ into Al_2O_3 (Equation 5.3). Therefore, the Y, Ba, and Cu nitrates were not affected by this reaction.

The second exothermic peak indicated the decomposition of Y, Ba, and Cu nitrate. These peaks possessed higher exothermicity due to higher amount of Y, Ba, and Cu nitrate in the gel samples compared to $Al(NO_3)_3$. Thus it generated more NH_4NO_3 which then deliberated higher amount of heat during decomposition reaction. The decomposition reaction for each sample was occurred at different temperatures. Due to the presence of different amount of Al_2O_3 in the gel which was formed during the first decomposition reaction was the reason for different decomposition temperature of the nitrates. The heat which supposed to be used in the decomposition reaction of NH_4NO_3 was absorbed by this Al_2O_3. Therefore, the increment of Al_2O_3 in gel samples delayed the decomposition reaction of NH_4NO_3 and increased the exothermic temperature. This phenomenon was nearly similar as occurred in Y_2O_3 stabilized ZrO_2 reported by Singh et al. (2007). The intensity of the second exothermic peak was decreased with the increase of $Al(NO_3)_3$ since the citric acid used as fuel in the first decomposition reaction was increased. The citric acid left for the second decomposition was slightly lower in each sample thus the generated heat was decreased.

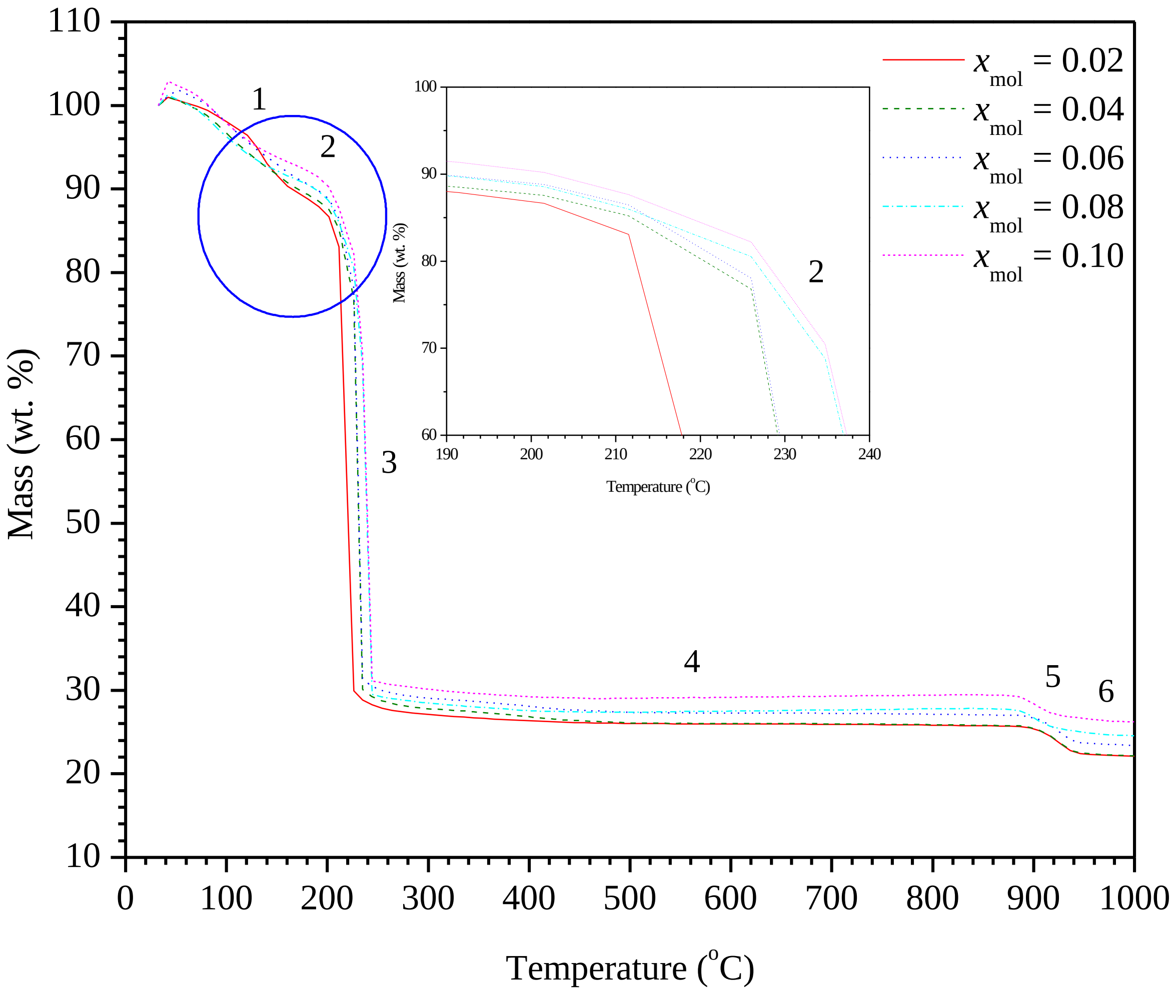

Figure 5.4: TG curve of $Al(NO_3)_3$ added gel samples. Inset shows TG curves in circle.

The TG curves of the gel samples having different composition of $Al(NO_3)_3$ is shown in Figure 5.4. The pattern of each curve was identical and classified into 6 steps as numbered in Figure 5.4 and listed in Table 5.1. About 3-11 % of mass was lost in the $Al(NO_3)_3$ added gel in between temperature ranging from 190 to 210 °C due to the decomposition of $Al(NO_3)_3$. This reaction was occurred at the early stage of heating after dehydration of the gel. Then a massive weight loss was occurred at temperature range of 220-240 °C due to the decomposition of Y, Ba and Cu nitrate. After this massive weight loss Y_2O_3, $BaCO_3$ and CuO ashes were stabilized until 900 °C and then formed $YBa_2Cu_3O_{7-\delta}$ and Al_2O_3 as indicated by 0.8 % of mass loss at around 900 – 920 °C.

Higher weight loss was observed in the gel containing higher amount of $Al(NO_3)_3$ due to the increased decomposition of $Al(NO_3)_3$. The higher amount of Al_2O_3 ashes were formed after this reaction and distributed in the gel sample which then increased its thermal stability. Therefore, the decrease of mass loss of the gel samples after decomposition reactions of Y, Ba, and Cu nitrate resulted with higher mass of intermediate product. However Al_2O_3 ashes stayed as it was and did not involve in any reaction upon formation of $YBa_2Cu_3O_{7-\delta}$ because it is very stable in that temperature range (Li et al., 2007). The existence of Al_2O_3 nanoparticles were emphasized by the final weight of the product as listed in Table 5.1 which occurred to be increased with $Al(NO_3)_3$ additions in gel samples.

Table 5.1. Reaction and weight loss of the $Al(NO_3)_3$ added gel samples at varied steps.

Step	Temperature (°C)	Reactions	Weight loss (wt. %)				
			Samples (x_{mol})				
			0.02	0.04	0.06	0.08	0.10
1	30 - 190	Water dehydration	13.35	14.8	13.55	19.47	17.81
2	190-220	Decomposition of $Al(NO_3)_3$	3.57	8.41	9.42	11.74	12.74
3	220-240	Decomposition of Y, Ba and Cu nitrate	53.16	46.71	45.70	39.29	38.30
4	240-900	Stabilization of intermediate product	-	-	-	-	-
5	900-920	Formation of $YBa_2Cu_3O_{7-\delta}$ + Al_2O_3;	0.82	0.88	0.84	0.74	0.75
			Final mass (wt. %)				
6	920-950	Growth of Al_2O_3 added $YBa_2Cu_3O_{7-\delta}$	21.10	22.16	23.42	24.58	26.23

5.2 Structural properties of Al_2O_3 added $YBa_2Cu_3O_{7-\delta}$

XRD pattern of $YBa_2Cu_3O_{7-\delta}$ and Al_2O_3 nanoparticles added $YBa_2Cu_3O_{7-\delta}$ samples were shown in Figure 5.5. Each XRD pattern was identical with significant peaks occurred for polycrystalline $YBa_2Cu_3O_{7-\delta}$. Intensity of these peaks was varied by the composition of Al_2O_3.

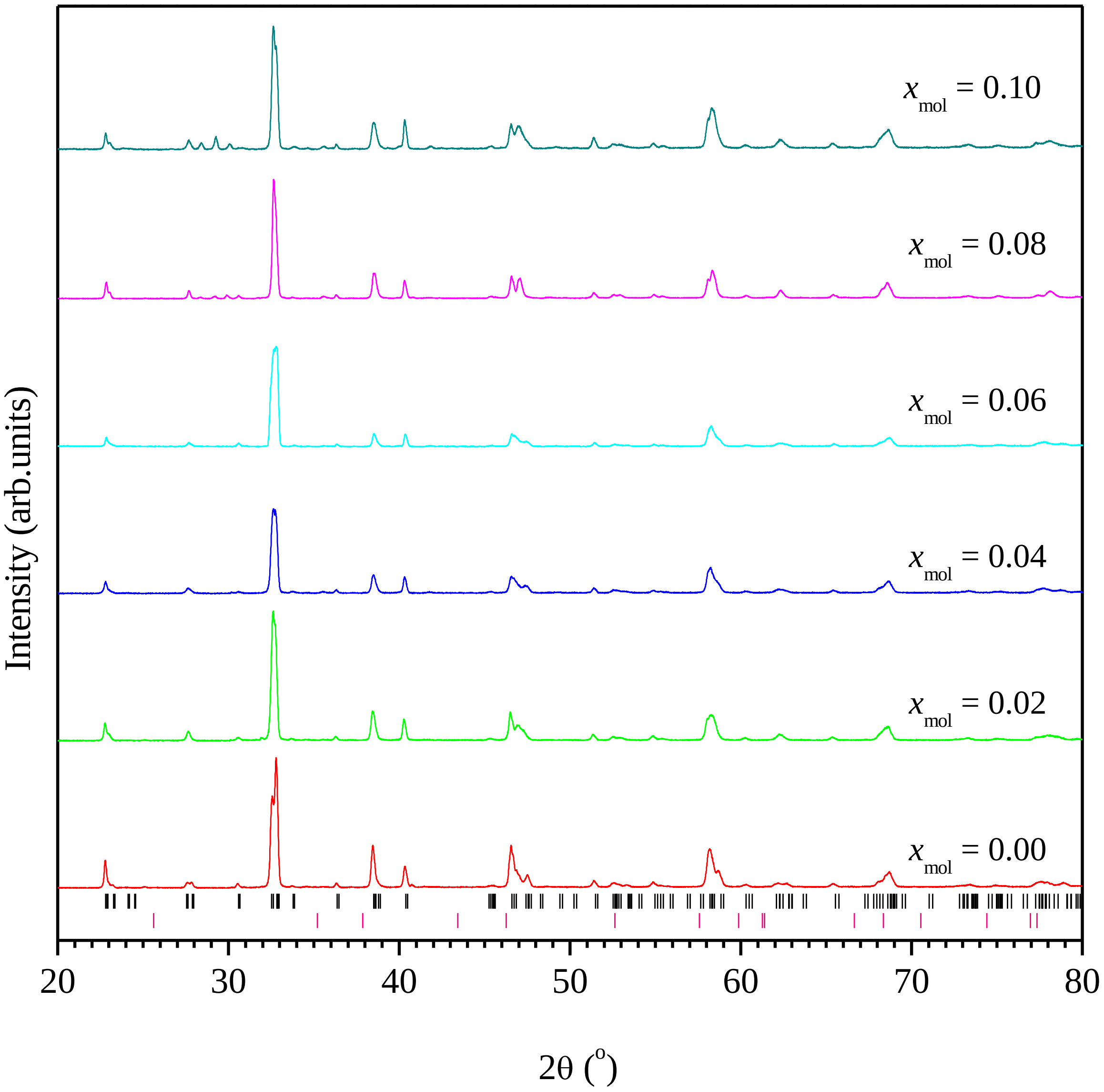

Figure 5.5: XRD pattern of $YBa_2Cu_3O_{7-\delta}$ and Al_2O_3 nanoparticles added $YBa_2Cu_3O_{7-\delta}$ samples. Black and pink bars at bottom show Bragg diffraction pattern for $YBa_2Cu_3O_{7-\delta}$ and Al_2O_3 respectively.

The XRD patterns revealed that each sample yielded polycrystalline $YBa_2Cu_3O_{7-\delta}$ as it most dominant structure. Increased amount of Al_2O_3 in the sample has altered the structural parameter of $YBa_2Cu_3O_{7-\delta}$ thus affecting the intensity peak.

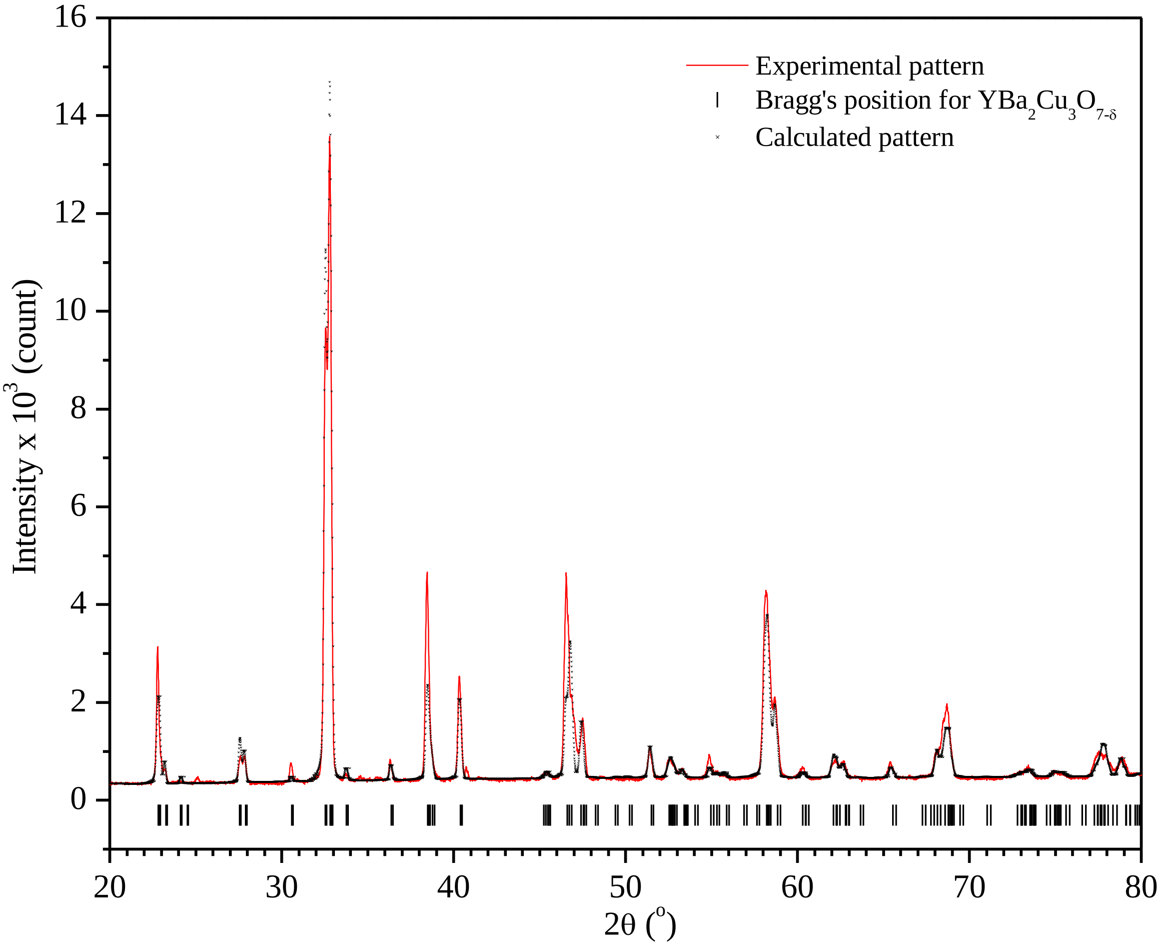

Figure 5.6: Refined XRD pattern of sample without Al_2O_3 nanoparticles ($x_{mol} = 0.00$).

Figure 5.6 shows the refined XRD pattern of the sample having $x_{mol} = 0.00$ with intensity differences line and Bragg's diffraction position for $YBa_2Cu_3O_{7-\delta}$ and Al_2O_3 phase. It is revealed that this sample contained polycrystalline pure $YBa_2Cu_3O_{7-\delta}$ phase since all significant peaks were assigned to Bragg's diffraction position of $YBa_2Cu_3O_{7-\delta}$. Thus, no evidence of impurity phase was yielded in the sample. The differences of intensity were attributed from the alteration of the structural parameters of the sample (Cava et al., 1990). From this refinement, it was measured that the $YBa_2Cu_3O_{7-\delta}$ phase in this sample possessed the lattice parameters of *a* = 3.823 Å, *b* = 3.873 Å and *c* = 11.681 Å. This provided the orthorhombicity value of 0.00763 for this sample. It was also calculated that the crystallite size of this sample was 45.50 nm. The intensity differences lines among the various compositions of Al_2O_3 nanoparticles added $YBa_2Cu_3O_{7-\delta}$ samples are shown in Figure 5.7.

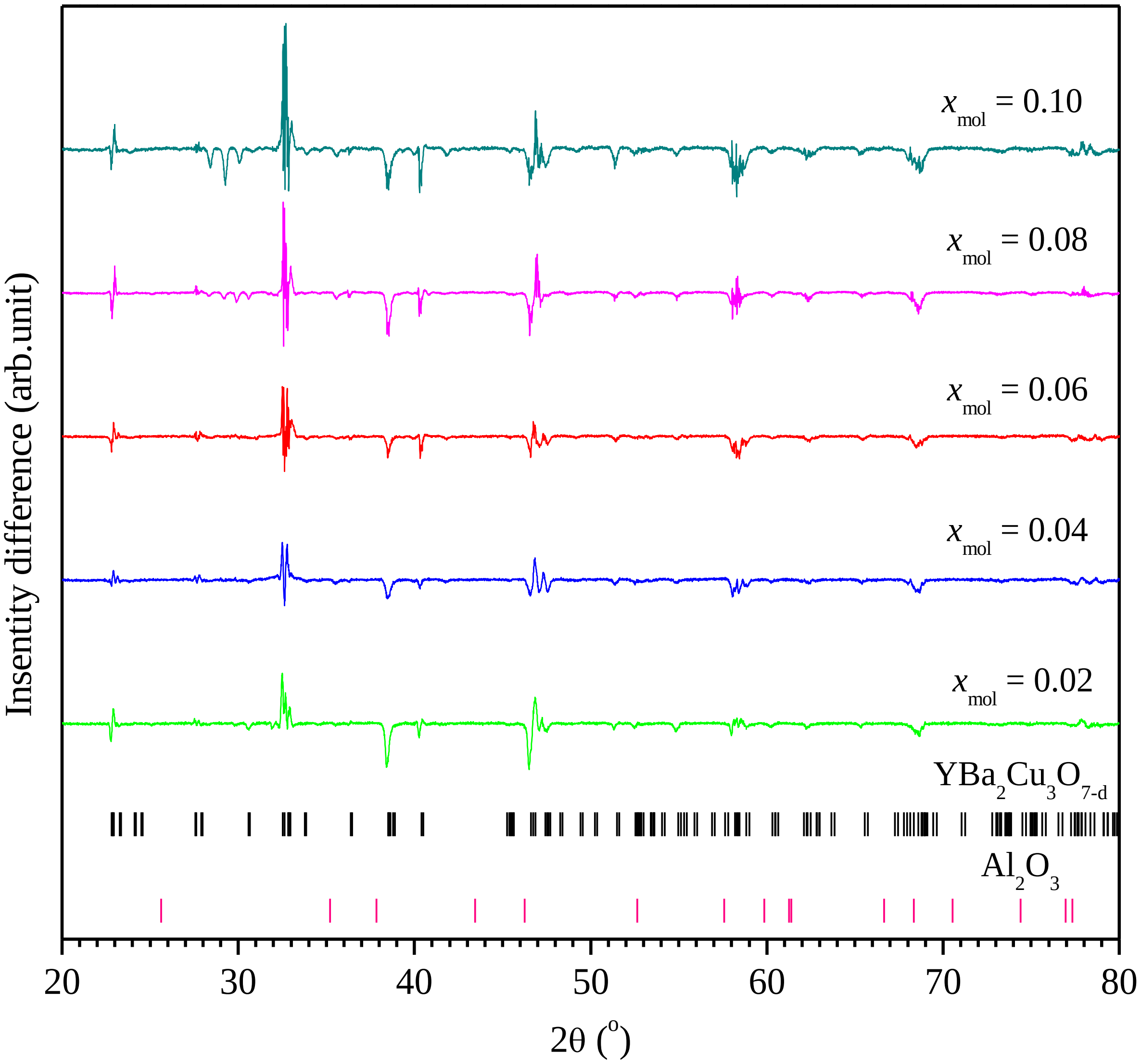

Figure 5.7: Intensity difference patterns for various composition of Al_2O_3 nanoparticles added $YBa_2Cu_3O_{7-\delta}$ samples.

In Figure 5.7, smooth intensity difference lines with few minor peaks were observed. It appeared that each minor peak was assigned to Bragg's diffraction position of $YBa_2Cu_3O_{7-\delta}$. This evidence confirmed the existence of polycrystalline $YBa_2Cu_3O_{7-\delta}$ phase as dominant structure in each sample. Intensity of these minor peaks was varied from sample to sample due to the alteration of the structural parameters of $YBa_2Cu_3O_{7-\delta}$ by the addition of Al_2O_3 nanoparticles. The existence of Al_2O_3 was unable to confirm in the samples due to having no significant peak in the XRD pattern. This could be due to the low intensity of Al_2O_3 peaks. Therefore it is difficult to be differentiated from the background peaks. In samples with x_{mol} = 0.02, 0.04, and 0.06, smooth lines at un-assigned 2θ angles indicate that these samples yielded no impurity. Instead, impurity might be existed in samples for the samples containing higher amount of Al_2O_3 such as x_{mol} = 0.08 and 0.10, since few peaks which were not assigned for $YBa_2Cu_3O_{7-\delta}$ or Al_2O_3 detected at around $2\theta = 29°$.

The Al_2O_3 crystalline phase in the samples was yielded from Al_2O_3 ashes through calcination process as shown in Equation (5.4).

$$Al_2O_3 \text{ (ashes)} \rightarrow Al_2O_3 \text{ (crystalline)} \tag{5.4}$$

Formation of the crystalline Al_2O_3 was reported to be occurred at 850 °C (Li et al., 2007) which was before the formation of $YBa_2Cu_3O_{7-\delta}$. The crystalline Al_2O_3 is highly stable even at higher temperature up to 1200 °C. Therefore, it remained inert and did not involve in the formation reaction of $YBa_2Cu_3O_{7-\delta}$ at 900 °C. These two phases were remained separated during the sintering process at 950 °C followed by heat treatment at 500 °C. The XRD pattern for Al_2O_3 ashes and crystalline Al_2O_3 are shown in Figures 5.8 and 5.9, respectively.

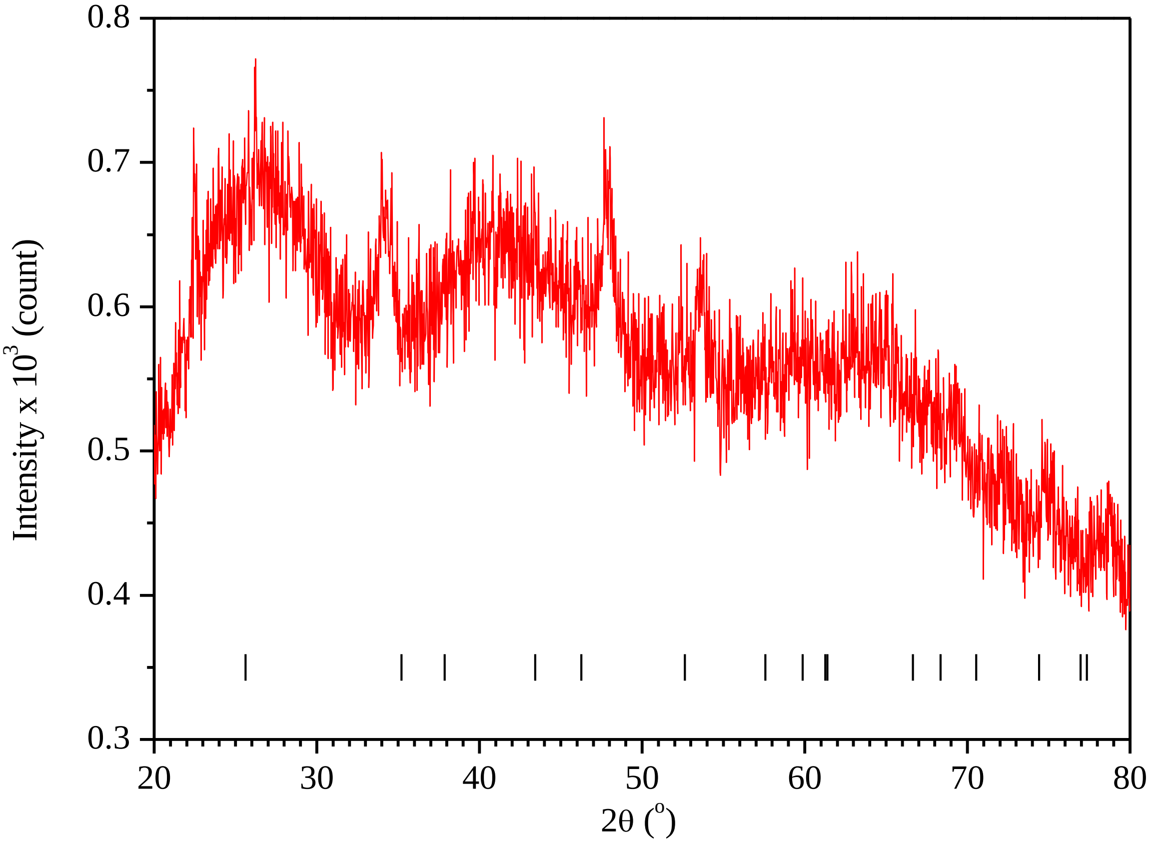

Figure 5.8: XRD pattern of Al_2O_3 ashes.

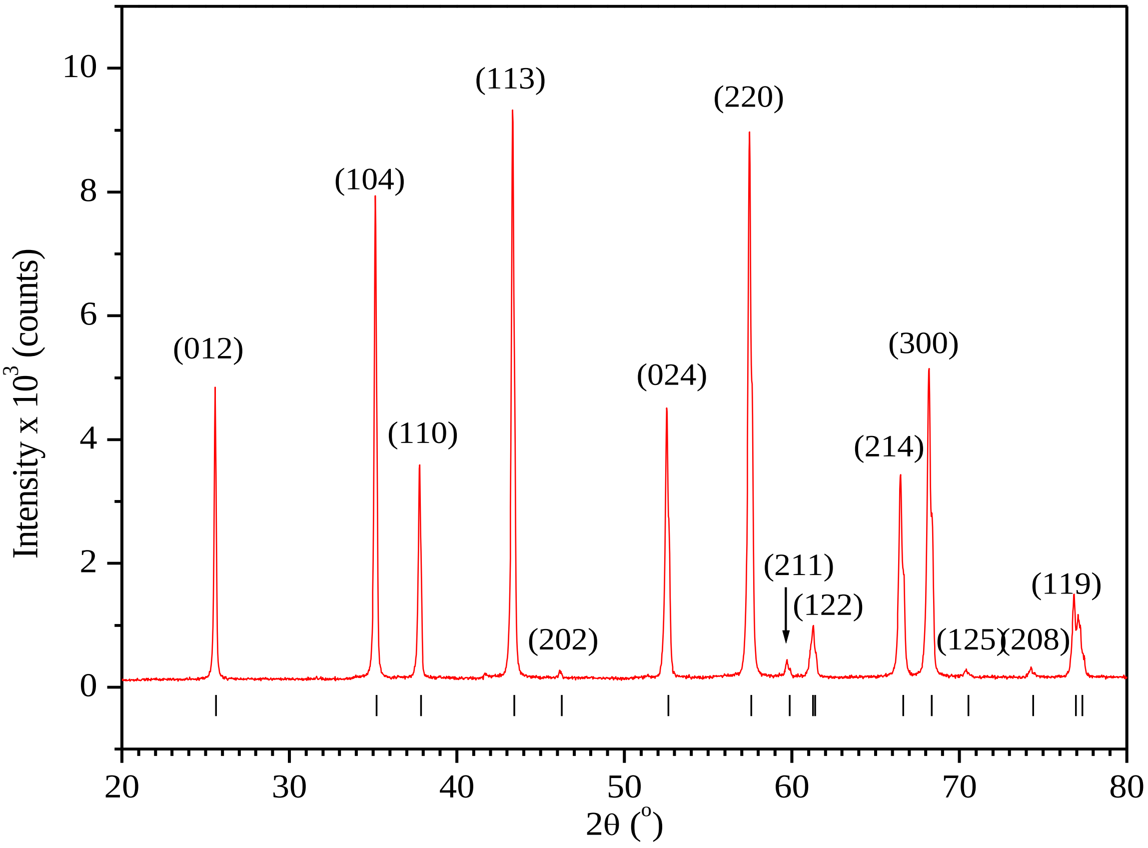

Figure 5.9: XRD pattern of crystalline Al_2O_3 after calcined at 900 °C for 1h.

Transformation of Al_2O_3 ashes to crystalline Al_2O_3 resulted in strong XRD peaks (Figure 5.9). However, no Al_2O_3 peaks were detected in the XRD or the intensity difference patterns as shown in Figure 5.7. This could be due to two factors: firstly, the low amount of yielded Al_2O_3 and secondly, the highly dominant crystalline $YBa_2Cu_3O_{7-\delta}$ phase. The Al_2O_3 yielded in the samples were very small which was ≤ 1.0 mol %. Thus it was suggested that the intensity of Al_2O_3 peaks would be hundred times lower than the $YBa_2Cu_3O_{7-\delta}$ peaks. In this circumstance, the Al_2O_3 peaks were disappeared in the noise background peaks. Furthermore, the $YBa_2Cu_3O_{7-\delta}$ phase yielded in the samples was highly crystalline and diffracted higher intensity of X-ray. Huge difference between the highest and lowest intense peaks made Al_2O_3 peaks invisible in the XRD patterns. Hence, the impurity peak appeared at angle of $2\theta = 29°$ in the $x_{\text{mol}} > 0.06$ sample (Figure 5.7) was assigned to Ba-Cu-O phase. As discussed in Section 4.2, this type of impurity occurred due to the imbalance ratio of Y_2O_3, $BaCO_3$, CuO ashes obtained from the incomplete decomposition reaction. Addition of Al_2O_3 at $x_{\text{mol}} > 0.06$ altered the decomposition behaviour of $YBa_2Cu_3O_{7-\delta}$ and produced ashes having slightly different composition. Upon calcination, the Ba-Cu-O impurity was formed together with Al_2O_3 and $YBa_2Cu_3O_{7-\delta}$ phases. The formation of BaCuO phase was significant in sample with $x_{\text{mol}} = 0.10$ as the peaks assigned to BaCuO phase can be easily detected on its XRD pattern (Figure 5.5). Formation of impurity phase in this sample can be attributed to existence of higher amount of Al_2O_3 which changed the decomposition behaviour therefore resulted with large unbalance ratio of expected ashes

Although the peaks of Al_2O_3 were difficult to detect, existence of Al_2O_3 in each sample yet can be proven by observing the affected peaks of $YBa_2Cu_3O_{7-\delta}$. The intensity differences patterns for $YBa_2Cu_3O_{7-\delta}$ peaks were increased as Al_2O_3 composition in the samples was increased. This characteristic occurred due to the fact that Al_2O_3 influenced the structural parameters of $YBa_2Cu_3O_{7-\delta}$ including the lattice constants and crystallite sizes. The *a* and *b* lattice constants, orthorhombicity, *c* lattice constant and crystallite sizes of the samples were shown in Figures 5.10, 5.11, 5.12 and 5.13, respectively.

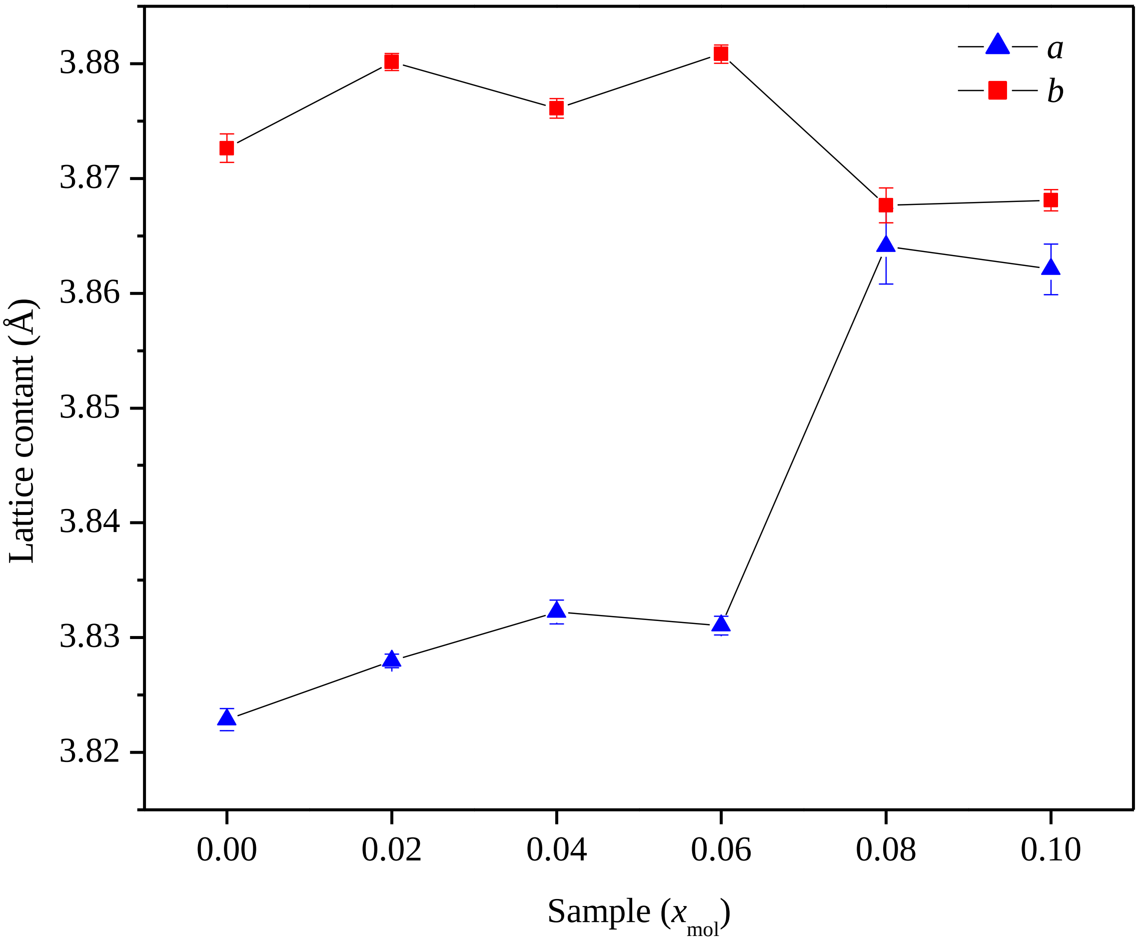

Figure 5.10: The *a* and *b* lattice constants of the samples. Error bars show standard deviation of lattice constant value.

Figure 5.10 shows *a* and *b* lattice constants of the $YBa_2Cu_3O_{7-\delta}$ and Al_2O_3 added $YBa_2Cu_3O_{7-\delta}$ samples. The *a* lattice constant was observed to increase with the addition of Al_2O_3. Samples with x_{mol} = 0.02, 0.04 and 0.06 possessed consistent value of *a* lattice constant with 3.830 Å which appeared close to the pure $YBa_2Cu_3O_{7-\delta}$. While, samples with x_{mol} = 0.08 and 0.10 possessed higher *a* lattice constant having average value of 3.860 Å with wider standard deviation. Nevertheless, the *b* lattice constant of Al_2O_3

added $YBa_2Cu_3O_{7-\delta}$ samples were not much different with pure $YBa_2Cu_3O_{7-\delta}$ sample. It occurred that the *b* lattice constant of each sample was in the range of 3.865 to 3.880 Å. Both of these lattice constants with different value of orthorhombicity are shown in Figure 5.11.

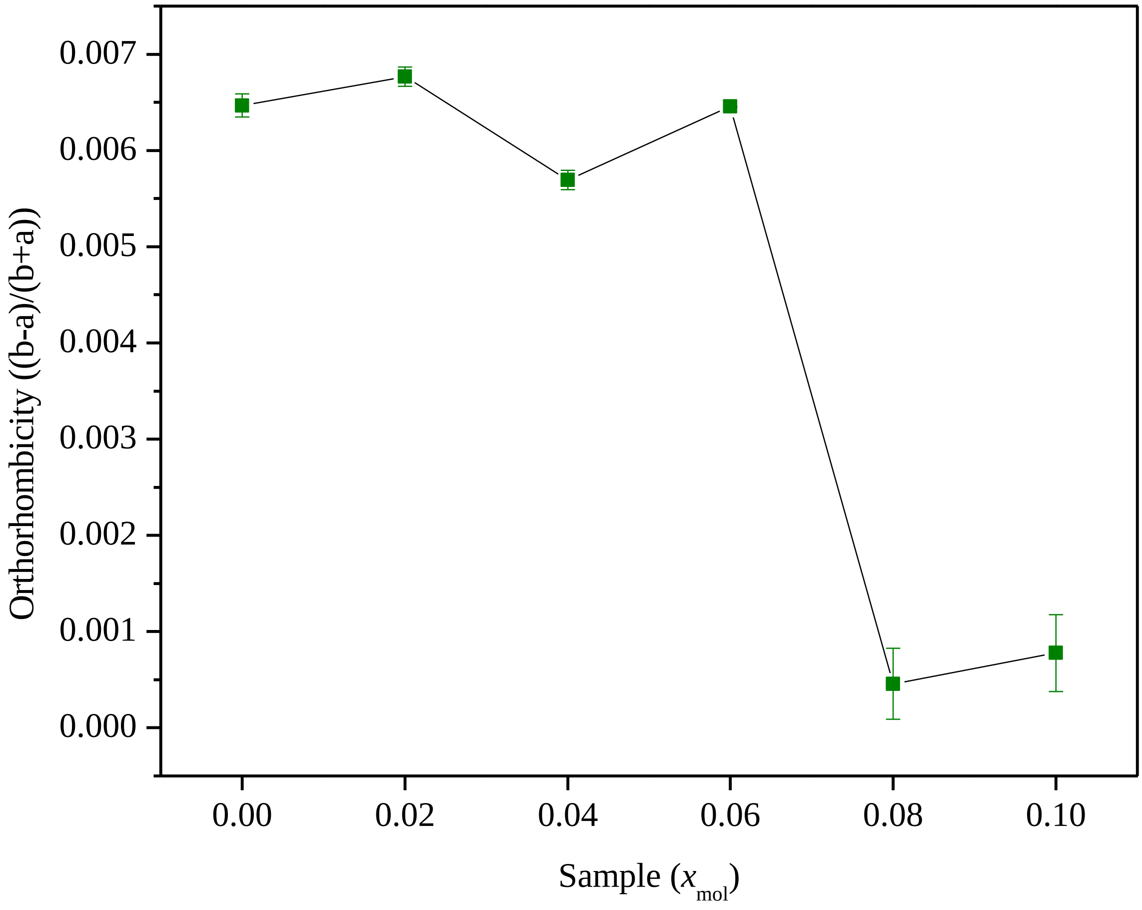

Figure 5.11: Orthorhombicity of un-added and Al_2O_3 added $YBa_2Cu_3O_{7-\delta}$ samples. Error bars show standard deviation of orthorhombicity.

In Figure 5.11, it can be clearly seen that the orthorhombicity of the Al_2O_3 added $YBa_2Cu_3O_{7-\delta}$ samples with x_{mol} = 0.02, 0.04 and 0.06 was consistent at around 0.006. These values were almost similar with the orthorhombicity value of pure $YBa_2Cu_3O_{7-\delta}$. The orthorhombicity value was suddenly dropped to below 0.001 for samples with x_{mol} = 0.08 and 0.10. The orthorhombic structure of the sample was preserved and did not transform to tetragonal structure even though the orthorhombicity value was achieving zero. On the other hand, the *c* lattice constant of the samples shown in Figure 5.12 was also varied by the addition of Al_2O_3.

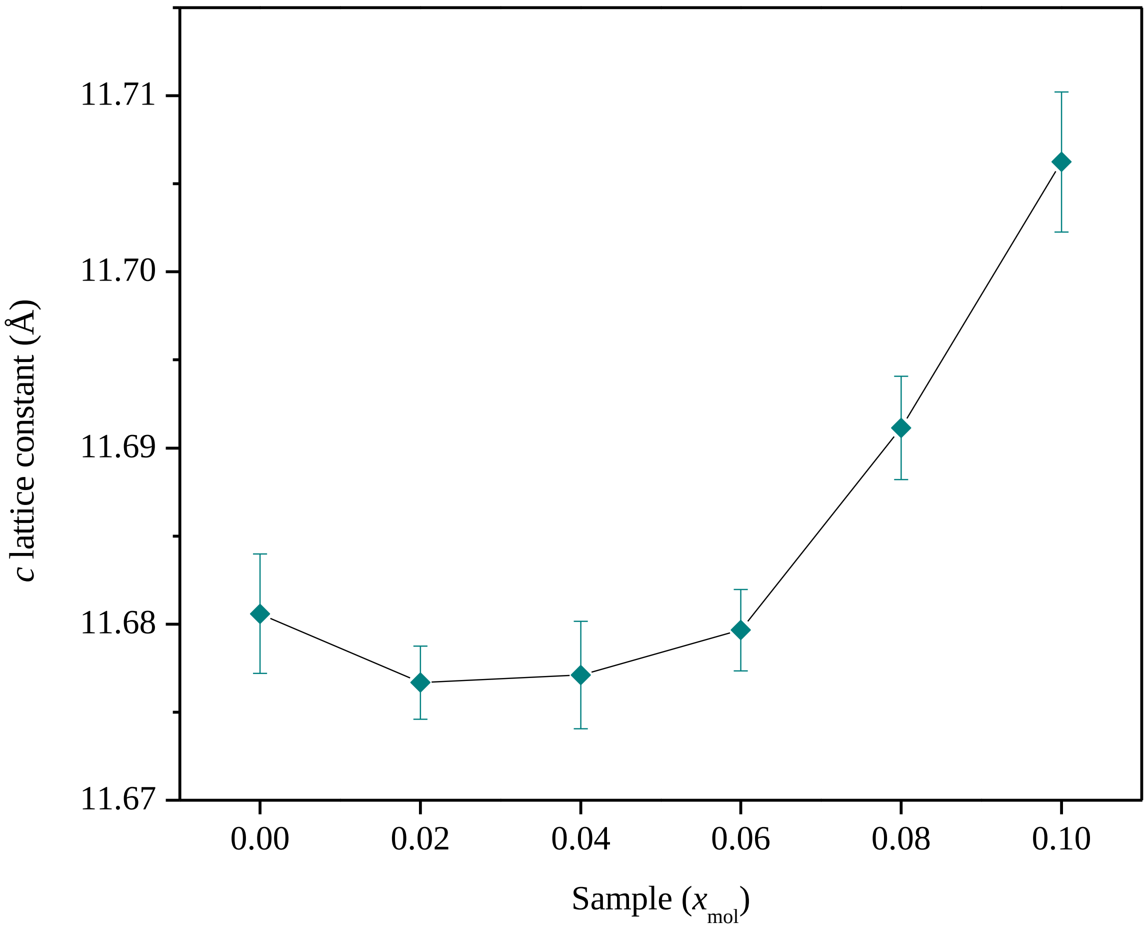

Figure 5.12: The *c* lattice constants of the samples. Error bars show standard deviation of *c* lattice constant.

It is observed in Figure 5.12 that the *c* lattice constant for samples with x_{mol} = 0.00, 0.02, 0.04 and 0.06 is around 11.680 Å. The value was increased to 11.690 Å and 11.705 Å for samples with x_{mol} = 0.08 and 0.10 respectively. Each value is followed by wide standard deviation.

Lattice constants of Al_2O_3 added $YBa_2Cu_3O_{7-\delta}$ samples were affected due to the addition of Al_2O_3. The effect was minor in samples with $x_{mol} \leq 0.06$ but apparent in samples with $x_{mol} \geq 0.08$. In samples with $x_{mol} \leq 0.06$, Al_2O_3 was believed to exist as separate phase and uniformly dispersed. Thus, it did not directly affect the $YBa_2Cu_3O_{7-\delta}$ phase. However, in samples with $x_{mol} \geq 0.10$, the Al_2O_3 phase might be involved with the $YBa_2Cu_3O_{7-\delta}$ structure. This was attributed to the fact that higher amount of yielded Al_2O_3 could be agglomerated to develop Al^{3+} ion rich spots. At the sintering temperature, the Al^{3+} ion could be possibly incorporated into the $YBa_2Cu_3O_{7-\delta}$ structure to partially replace Y^{3+} ion and thus resulted in the increment of *c* lattice constant. Upon this point, the oxygen content in $YBa_2Cu_3O_{7-\delta}$ was also re-adjusted to provide stoichiometric balance to the compound. This adjustment resulted in the increment of *a* lattice constant.

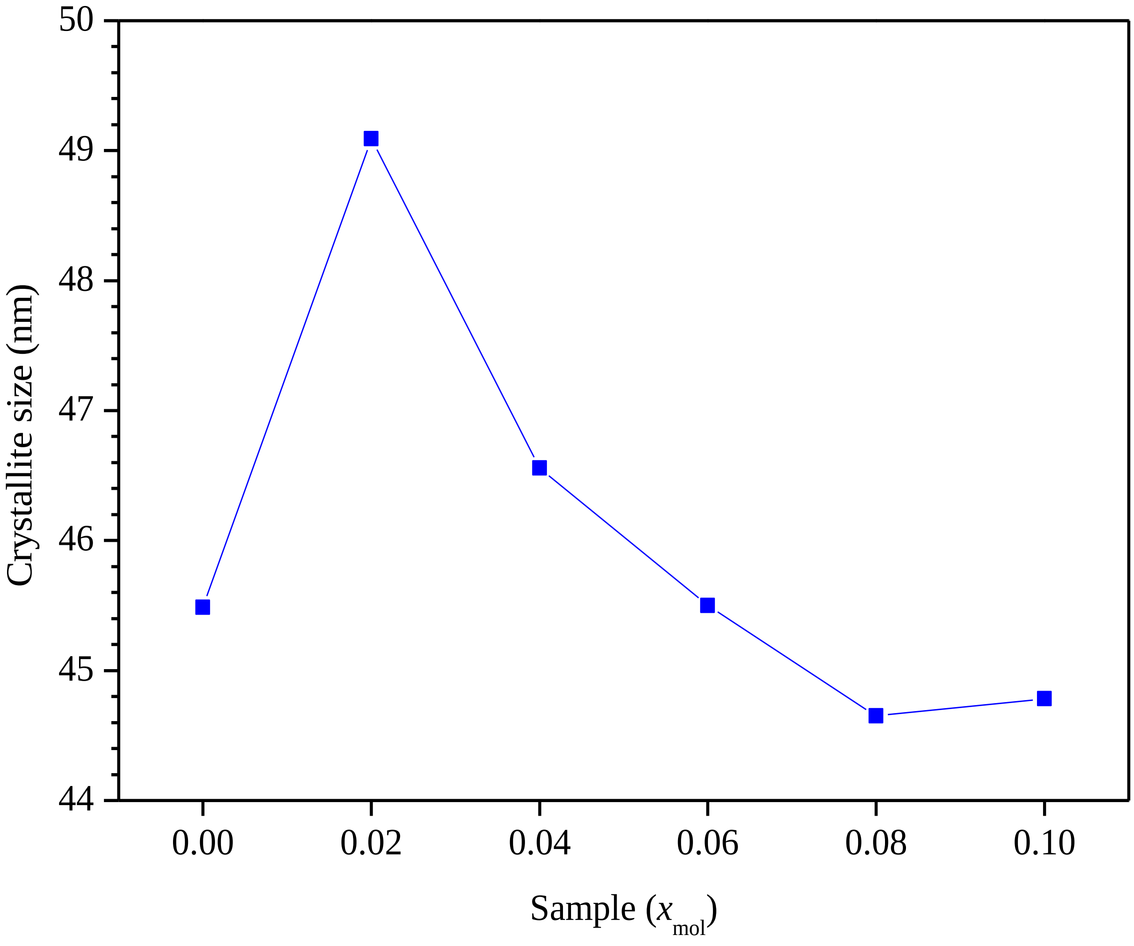

Figure 5.13: Crystallite sizes of un-added and Al_2O_3 added $YBa_2Cu_3O_{7-\delta}$ samples.

Crystallite sizes of the samples were calculated from the selected XRD peak using Debye-Scherer formula as shown in Figure 5.13. Pure $YBa_2Cu_3O_{7-\delta}$ sample with x_{mol} = 0.00 had crystallite size about 45.5 nm. It was increased to 49 nm in sample x_{mol} = 0.02. Then it was again decreased to 46.4, 45.5, 44.6 and 44.7 nm in samples with x_{mol} = 0.04, 0.06, 0.08 and 0.10, respectively. These changes could be attributed from two factors; which are higher grain growth of $YBa_2Cu_3O_{7-\delta}$ phase and existence of thermally stable Al_2O_3 phase in the samples. As discussed in Section 5.1, lower exothermicity was occurred during the decomposition reaction of Y, Ba and Cu nitrate gel as the Al_2O_3 ashes was increased in the sample where this type of reaction produced slightly bigger size of Y_2O_3, $BaCO_3$ and CuO ashes. During calcination step, these ashes less amount of $YBa_2Cu_3O_{7-\delta}$ grains were nucleated due to slower reaction rate. Another possible reason could be the heat consumption by Al_2O_3 ash to yield Al_2O_3 crystal. The fewer amounts of $YBa_2Cu_3O_{7-\delta}$ grains were capable to grow to bigger grain as sufficient heat and space were provided during heat treatment. Thus the crystallite size of $YBa_2Cu_3O_{7-\delta}$ in samples with $x_{mol} \leq 0.06$ was bigger compare to sample with x_{mol} = 0.00. Simultaneously, the Al_2O_3 crystal existed after calcination process impeded the grain growth of $YBa_2Cu_3O_{7-\delta}$ during heat treatment. In sample with $x_{mol} \leq 0.06$, the effect was minor because the Al_2O_3 was believed to be uniformly dispersed. However, the major affect was seen in samples with $x_{mol} > 0.06$ as higher amount of Al_2O_3 was possibly agglomerated. This may restrain further growth of $YBa_2Cu_3O_{7-\delta}$ grains hence produced smaller crystallite sizes. The crystallite sizes of $YBa_2Cu_3O_{7-\delta}$ in each samples was less than 50 nm. The Al_2O_3 added $YBa_2Cu_3O_{7-\delta}$ samples were structurally orthorhombic. Though the existence of Al_2O_3 phase was unable to confirm; however, significant affects can be observed on structure of $YBa_2Cu_3O_{7-\delta}$. Addition of Al_2O_3 in samples with $x_{mol} \leq 0.06$ brought only slight change in structural parameter.

5.3 Microstructure and EDX of Al_2O_3 added $YBa_2Cu_3O_{7-\delta}$

Microstructure of Al_2O_3 added $YBa_2Cu_3O_{7-\delta}$ samples are shown in Figures 5.13 – 5.17.

Figure 5.13: FESEM image of sample with $x_{mol} = 0.02$.

Figure 5.13 shows sample with $x_{mol} = 0.02$ consisted of two types of particulate microstructures. There were dominant particles with size ranging from 100 to 300 nm and nanoparticles with size about 10 nm. It was believed that the dominant and nanosized particles represent $YBa_2Cu_3O_{7-\delta}$ and Al_2O_3, respectively. $YBa_2Cu_3O_{7-\delta}$ particle was consisted of many $YBa_2Cu_3O_{7-\delta}$ grains thus possessed bigger size compared to the crystallite size. Though, these particles were connected with each other yet it was remained in low compaction. Large gaps among the $YBa_2Cu_3O_{7-\delta}$ particles can be seen in Figure 5.13. Further observation of this image revealed that Al_2O_3 nanoparticles were well distributed on the $YBa_2Cu_3O_{7-\delta}$ grains.

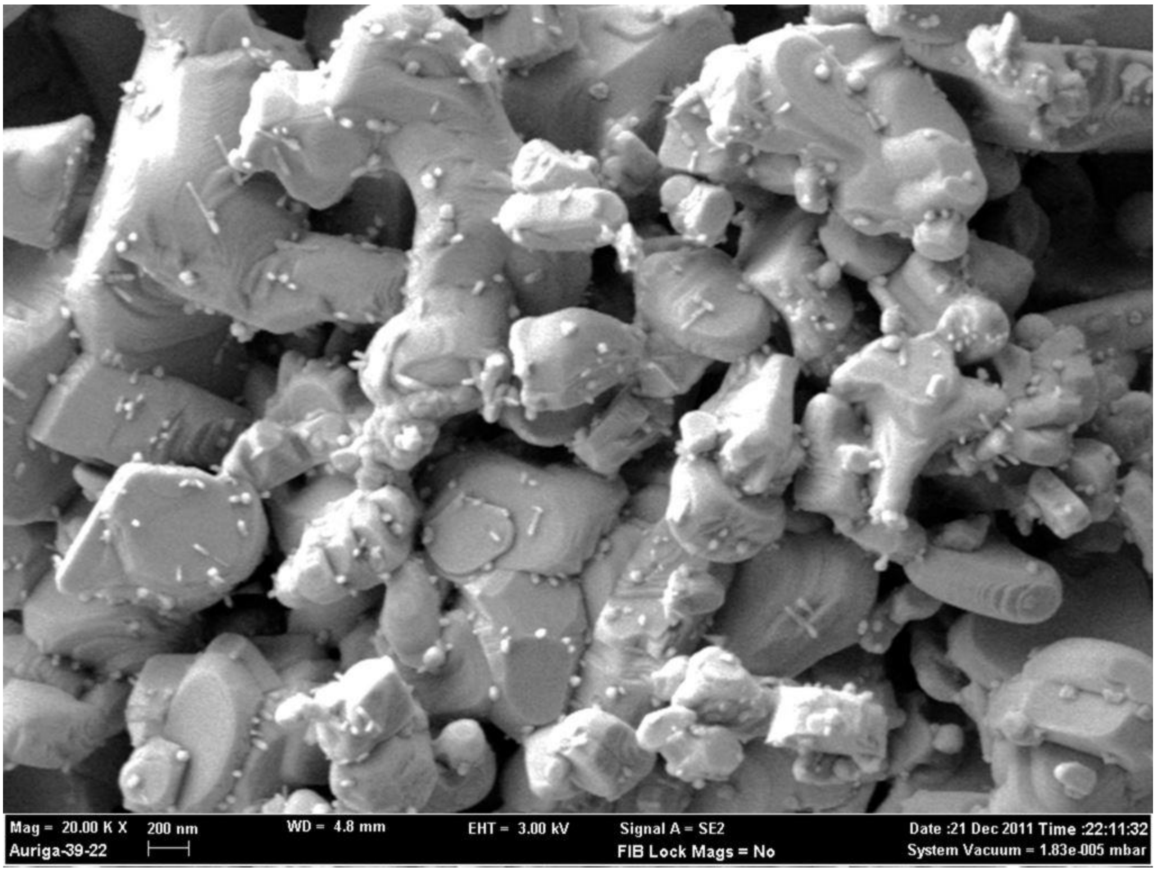

Figure 5.14: Microstructure image of sample with x_{mol} = 0.04.

In Figure 5.14, $YBa_2Cu_3O_{7-\delta}$ compound was observed to yield as dominant particles structure with size range from 100 to 300 nm. These particles were also consisted of many grains thus have bigger sizes compared to theirs crystallite size. $YBa_2Cu_3O_{7-\delta}$ particles of this sample possessed non-uniform shape with sharp edges. Therefore the connectivity between each particle was comparatively low due to higher degree connection angle. Larger gaps were formed between $YBa_2Cu_3O_{7-\delta}$ particles. These particles co-existed with Al_2O_3 nanoparticles with size about 10 nm which was distribute on the $YBa_2Cu_3O_{7-\delta}$ grains.

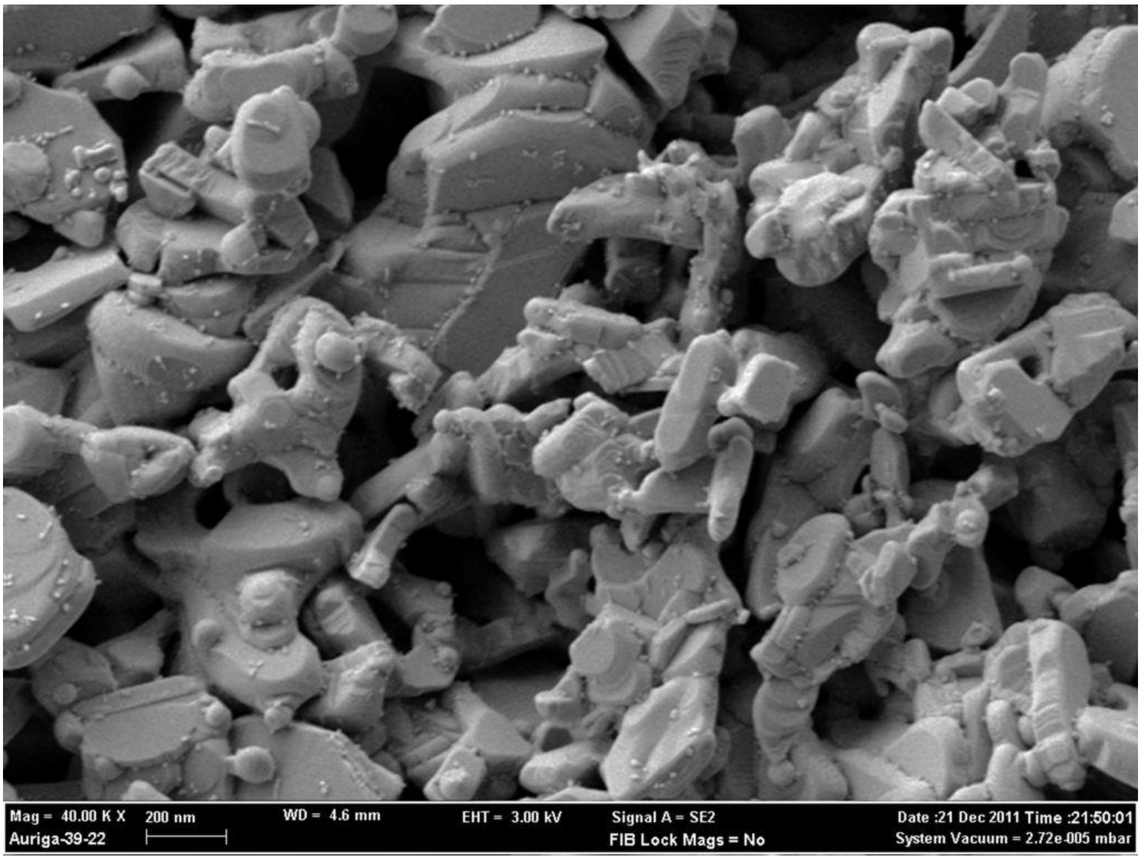

Figure 5.15: FESEM image of sample with $x_{\mathrm{mol}} = 0.06$.

Figure 5.15 shows the morphology of the $YBa_2Cu_3O_{7-\delta}$ sample with $x_{\mathrm{mol}} = 0.06$. The $YBa_2Cu_3O_{7-\delta}$ particles were observed to have orthorhombic-like structure with sizes ranged from 50 to 200 nm. It appeared that some of these particles were formed of single crystal of $YBa_2Cu_3O_{7-\delta}$ since the smallest size of the particles observed in this figure is almost same with the crystallite size. On the other hand, other particles were consisted of many $YBa_2Cu_3O_{7-\delta}$ grains thus yielded bigger particle size. $YBa_2Cu_3O_{7-\delta}$ particles had nearly uniform shape and size yet with sharper edges. This phenomenon results in poor connectivity among the particles hence developed larger gaps. Al_2O_3 nanoparticles having size of 10 nm were uniformly distributed on the grains of $YBa_2Cu_3O_{7-\delta}$. Increased amount of Al_2O_3 in this sample results in high visibility of the nanoparticles.

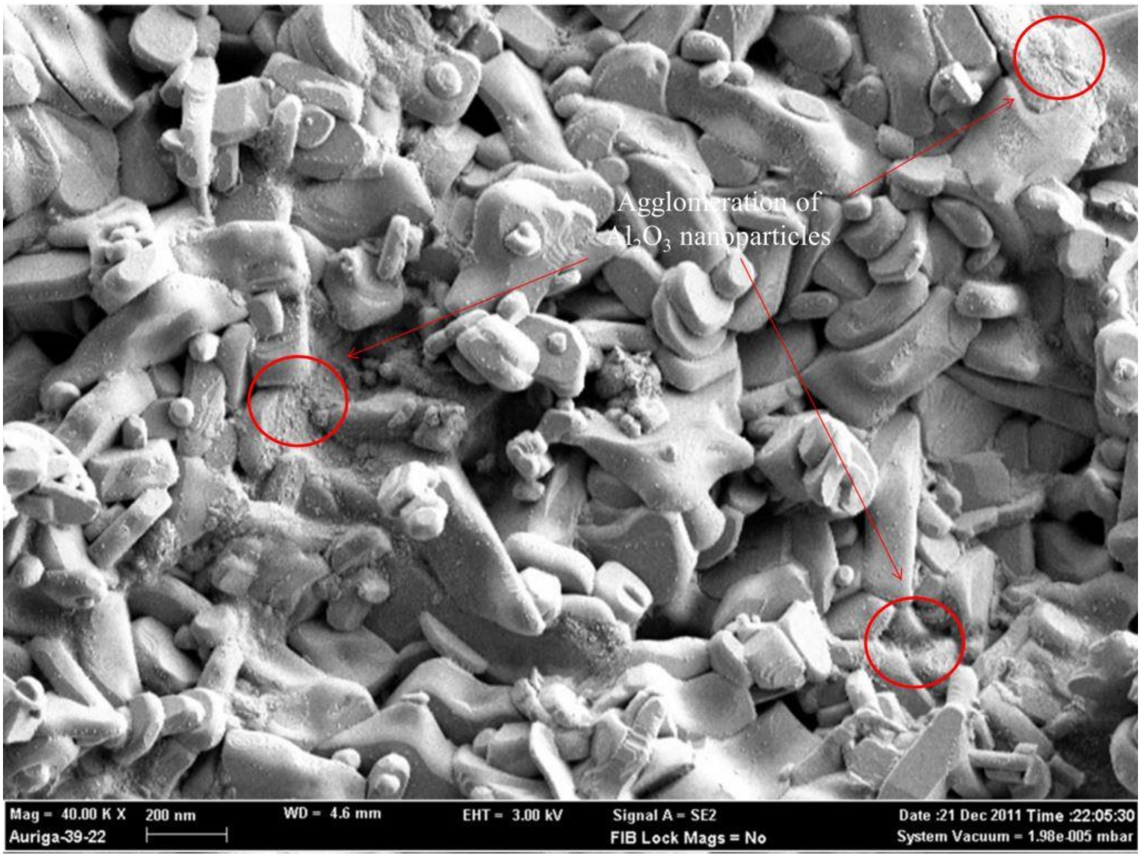

Figure 5.16: FESEM image of sample with $x_{\mathrm{mol}} = 0.08$.

Morphology of sample with $x_{\mathrm{mol}} = 0.08$ is shown in Figure 5.16. It revealed the existence of $YBa_2Cu_3O_{7-\delta}$ particles with sizes ranged from 50 to 200 nm. Variation of the sizes was attributed from single or multi $YBa_2Cu_3O_{7-\delta}$ grains in the particle. These particles were observed to have smooth edges and were connected with each other to form low pores and denser sample. In this figure, Al_2O_3 nanoparticles having particle size of 10 nm were only detected at certain part of $YBa_2Cu_3O_{7-\delta}$ microstructure. The nanoparticles were observed to agglomerate at $YBa_2Cu_3O_{7-\delta}$ inter-particles.

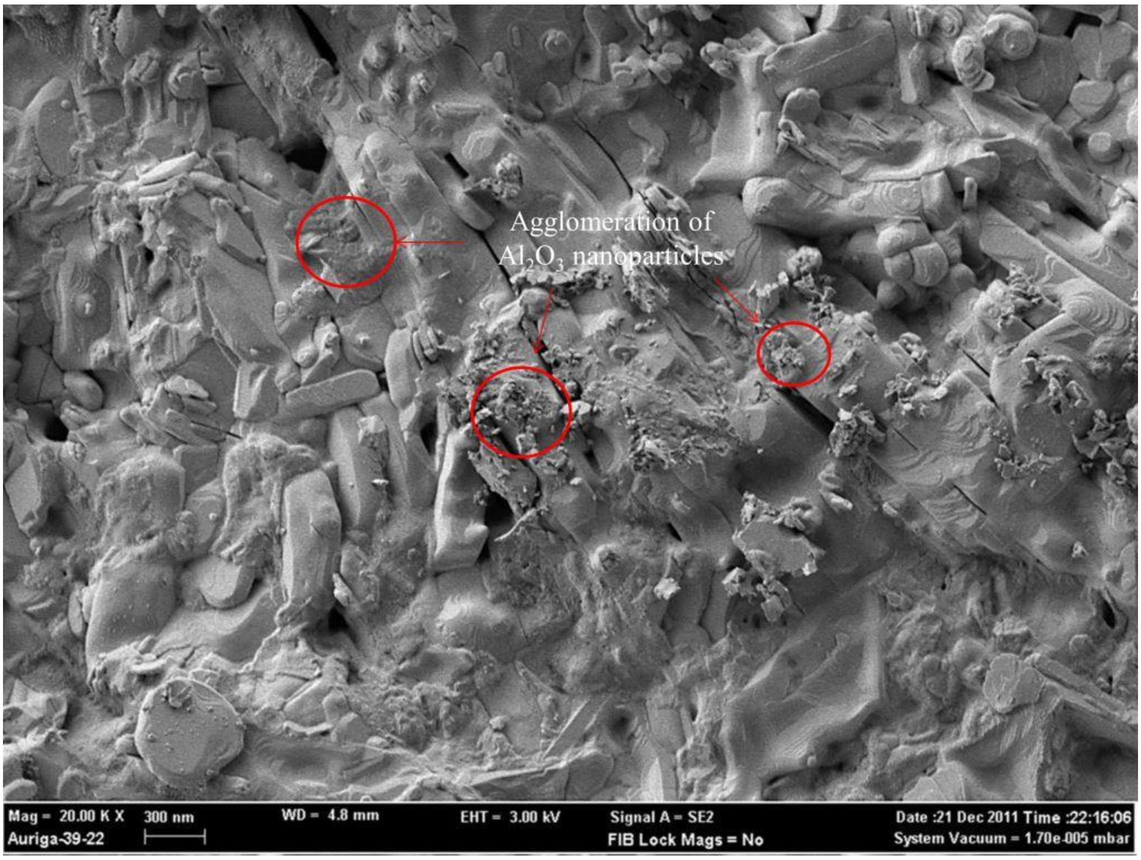

Figure 5.17: FESEM image of sample with $x_{\mathrm{mol}} = 0.10$.

Figure 5.17 shows the morphology of sample with $x_{\mathrm{mol}} = 0.10$. It was observed that the sample had molten-like microstructure. $YBa_2Cu_3O_{7-\delta}$ particles were connected and linked together thus formed a sample with higher density. Each particle was difficult to identify individually. It was estimated that $YBa_2Cu_3O_{7-\delta}$ particles possessed sizes ranging from 200 to 400 nm which might be consisted of many $YBa_2Cu_3O_{7-\delta}$ grains. On other hand, Al_2O_3 nanoparticles having size of 10 nm were observed to be highly agglomerated at the center of micrograph. It is believed that Al_2O_3 nanoparticles were covered by the molten $YBa_2Cu_3O_{7-\delta}$ structure in the other parts of the sample.

The EDX area and spot analysis for each sample was taken for the whole micrograph and pointing on nanoparticles as it is shown in Figure 5.18 and 5.19, respectively.

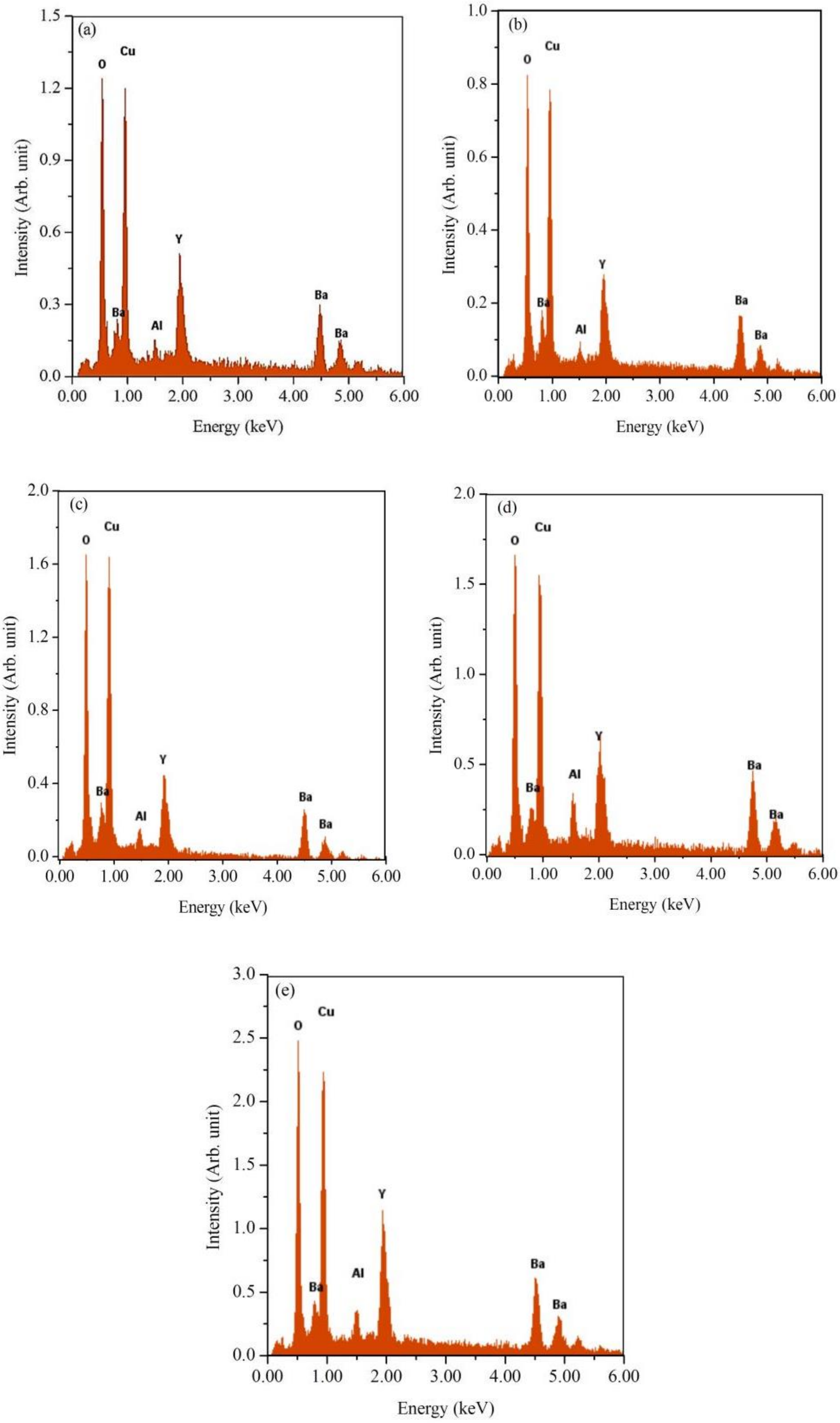

Figure 5.18: EDX area analysis for Al_2O_3 added $YBa_2Cu_3O_{7-\delta}$ samples; (a) $x_{mol} = 0.02$, (b) $x_{mol} = 0.04$, (c) $x_{mol} = 0.06$, (d) $x_{mol} = 0.08$ and (e) $x_{mol} = 0.10$.

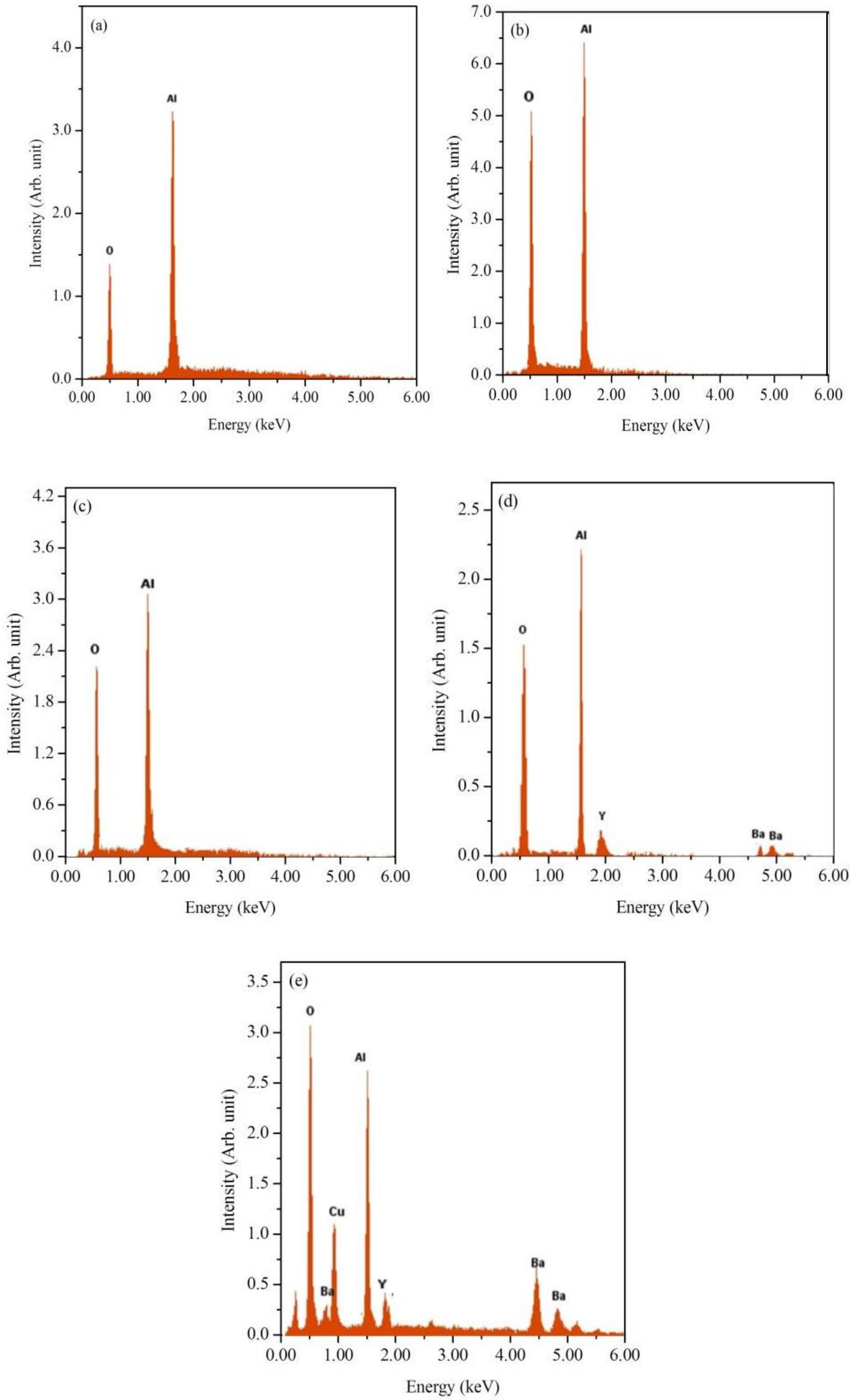

Figure 5.19: EDX spot analysis pointed on nanoparticles; (a) x_{mol} = 0.02, (b) x_{mol} = 0.04, (c) x_{mol} = 0.06, (d) x_{mol} = 0.08 and (e) x_{mol} = 0.10.

Table 5.2: Elemental analysis of $YBa_2Cu_3O_{7-\delta}$ structure and Al_2O_3 nanoparticles in each Al_2O_3 added $YBa_2Cu_3O_{7-\delta}$ samples.

Sample (x_{mol})	EDX analysis (Atomic %)					Estimated Formula
	Main Particles				Nanoparticle	
	Y	Ba	Cu	Al	Al	
0.02	8.03	16.24	24.01	0.11	41.13	$YBa_2Cu_3O_{7-\delta}$+ Al_2O_3
0.04	8.05	17.33	24.15	0.20	40.75	$YBa_{2.2}Cu_3O_{7-\delta}$+ Al_2O_3
0.06	8.08	16.58	23.69	0.29	40.55	$YBa_2Cu_3O_{7-\delta}$+ Al_2O_3
0.08	7.86	18.17	24.79	0.56	40.40	$Y_{1-x}Al_xBa_{2.2}Cu_{2.9}O_{7-\delta}$ + Al_2O_3
0.10	7.73	18.44	23.85	0.98	40.92	$Y_{1-x}Al_xBa_{2.1}Cu_3O_{7-\delta}$ + Al_2O_3

EDX patterns in Figures 5.18 and 5.19 confirm that the samples consisted of $YBa_2Cu_3O_{7-\delta}$ and Al_2O_3 phases. It was revealed that the atomic ratio of Y, Ba, and Cu elements of the main particle for each sample was nearly 1:2:3. Thus, it indicated the formation $YBa_2Cu_3O_{7-\delta}$ phase. This spectra was consisted of very low fraction of Al (below 1 %) attributed to the existence of Al_2O_3 nanoparticles. Further EDX analysis pointed on nanoparticles provided the evidence of Al_2O_3 in each sample. In samples with $x_{mol} \leq 0.06$, only Al and O were detected by EDX spot analysis on nanoparticles. Hence, it proved that Al_2O_3 nanoparticles were successfully synthesized and distributed in the samples. Al and O elements were also highly dominant in the samples with $x_{mol} > 0.06$ yet with other elements. Existence of these other elements at this structure may be attributed due to molten $YBa_2Cu_3O_{7-\delta}$ phase which covering Al_2O_3 nanoparticles. It was estimated that the atomic ratio of these elements in each sample were achieving 2:3 which is consistent with the atomic formula of Al_2O_3 phase.

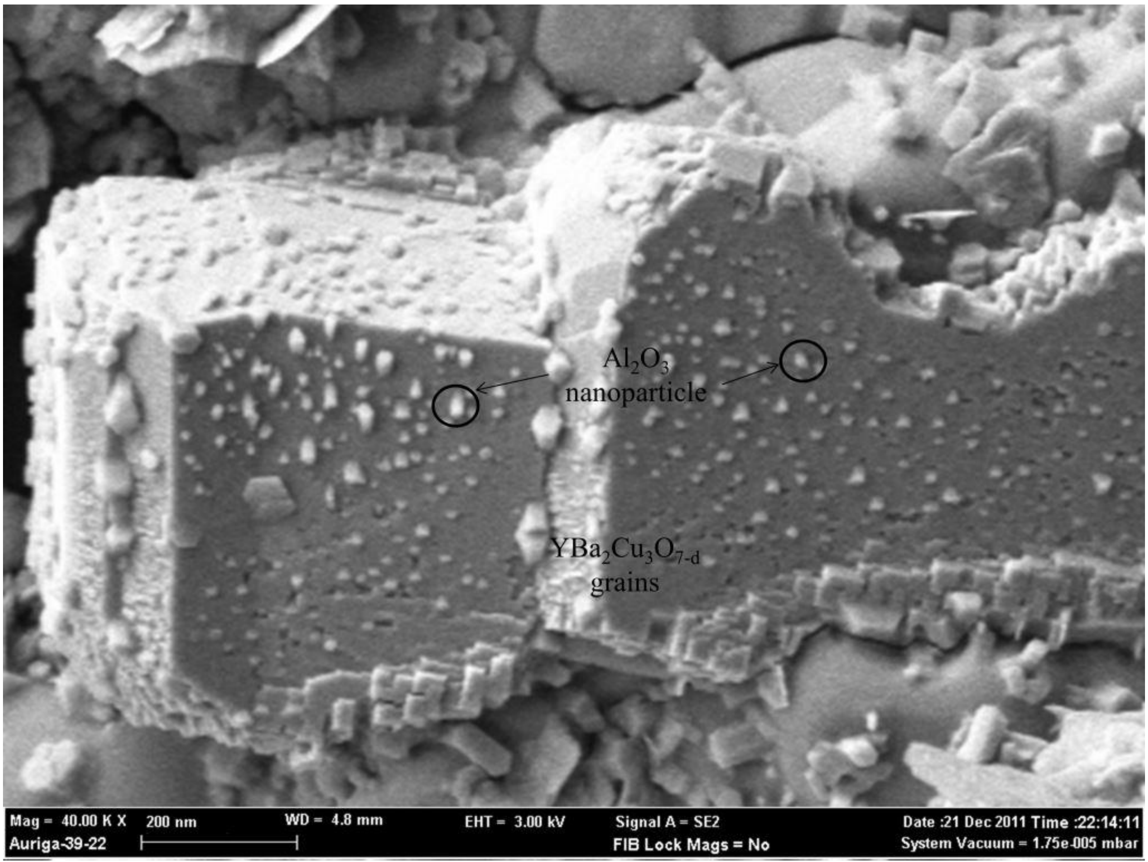

Figure 5.20: Microstructure of the intersection of $YBa_2Cu_3O_{7-\delta}$ for sample with $x_{mol} = 0.06$.

Microstructures of the Al_2O_3 added $YBa_2Cu_3O_{7-\delta}$ samples were varied by the composition of Al_2O_3. In samples with $x_{mol} = 0.02$, 0.04 and 0.06, the $YBa_2Cu_3O_{7-\delta}$ was existed as orthorhombic-like particles which consisted of both single and multi-crystal structure. The single crystal particles were much smaller compared with the multi-crystal particles thus gave a large range of particle sizes. Each of the $YBa_2Cu_3O_{7-\delta}$ particle contained well dispersed Al_2O_3 nanoparticles as shown in Figure 5.20. From these evidences, it could be suggested that Al_2O_3 nanoparticles for these compositions were more likely acted as reinforcing particle rather than to incorporate in $YBa_2Cu_3O_{7-\delta}$ structure. At higher amount addition of Al_2O_3 nanoparticles such as, samples with x_{mol} = 0.08 and 0.10, sort of melting was occurred at inter $YBa_2Cu_3O_{7-\delta}$ particles. Al_2O_3 nanoparticles which supposed to be distributed on the grains were instead agglomerated at the grain boundaries of $YBa_2Cu_3O_{7-\delta}$. It was believed that these agglomerated Al_2O_3 nanoparticles and $YBa_2Cu_3O_{7-\delta}$ were reacted together during sintering temperature. This reaction altered the microstructure of the sample by connecting particles resulting in improved connectivity. The reaction which might occur between agglomerated Al_2O_3 nanoparticles and $YBa_2Cu_3O_{7-\delta}$ structure was the incorporation of Al^{3+} to replace Y^{3+} site as shown Equation (5.5).

$$x\,\mathrm{Al} + YBa_2Cu_3O_{7-\delta} \rightarrow Y_{1-x}Al_xBa_2Cu_3O_{7-\delta} \qquad (5.5)$$

Agglomeration of Al_2O_3 nanoparticles developed higher density of Al^{3+} ions at sintering temperature, which might diffuse into the $YBa_2Cu_3O_{7-\delta}$ structure and replaced a fraction of Y^{3+} site. The replacement is visible in EDX analysis, as higher amount of Al was detected in $YBa_2Cu_3O_{7-\delta}$ as well as Y at Al_2O_3 nanoparticles. In these samples, the Al_2O_3 nanoparticles were acted as reinforcing element and improved the connectivity among the particles.

5.4 Analysis of microhardness

Microhardness of $YBa_2Cu_3O_{7-\delta}$ and Al_2O_3 added $YBa_2Cu_3O_{7-\delta}$ samples is shown in Figure 5.21.

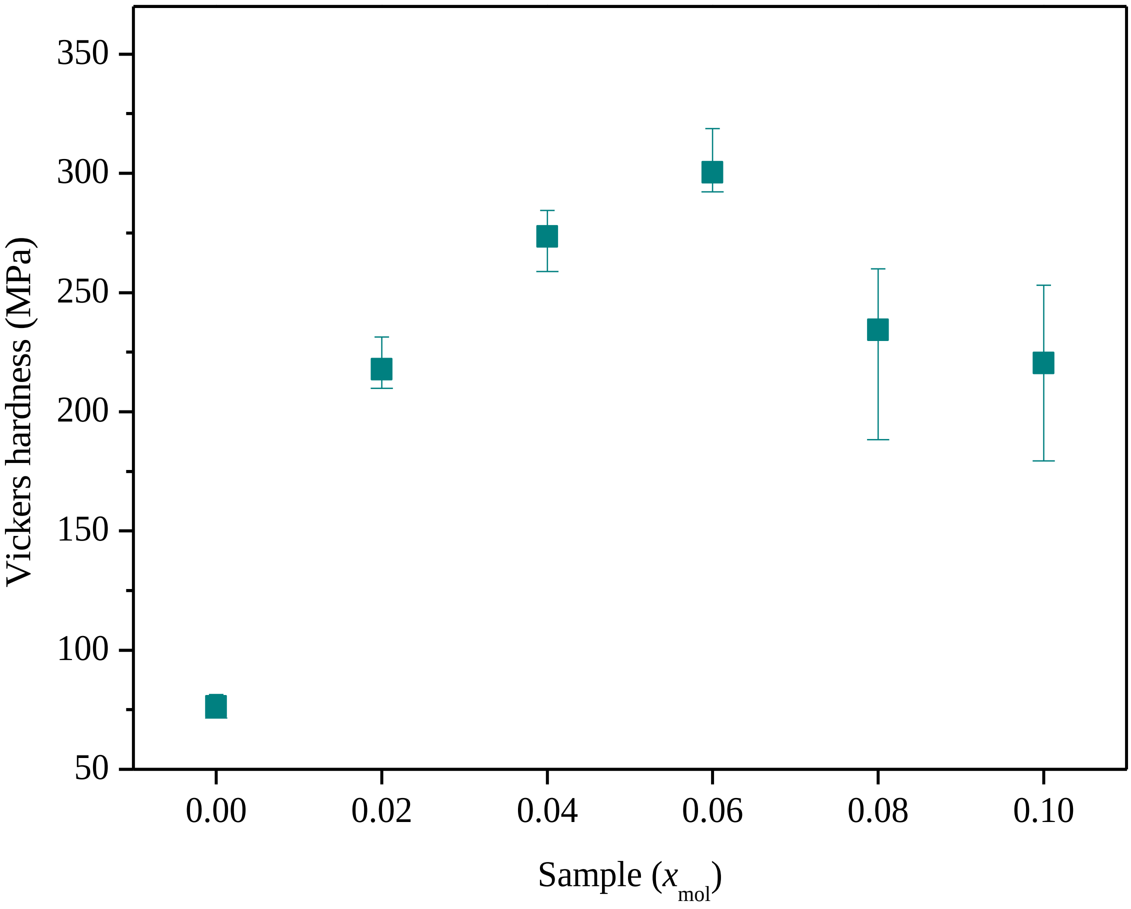

Figure 5.21: Vickers microhardness of un-added and Al_2O_3 added $YBa_2Cu_3O_{7-\delta}$ samples.

It can be observed that the microhardness of un-added $YBa_2Cu_3O_7$ sample with x_{mol} = 0.00 was about 80 Mpa. An obvious increase of microhardness up to 220 MPa was observed by the addition of Al_2O_3 in sample with x_{mol} = 0.02. The microhardness kept increasing as the concentration of Al_2O_3 nanoparticles were increased and achieved the highest value of 300 MPa in sample with x_{mol} = 0.06. Then the microhardness were decreased to 230 then to 220 Mpa by further increase of Al_2O_3 nanoparticles for the samples with x_{mol} = 0.08 and 0.10, respectively. It is notable that the microhardness for sample with $x_{mol} \leq 0.06$ was increased with low standard deviation while microhardness for samples with $x_{mol} > 0.06$ came with larger standard deviations.

Variation of microhardness can be related with the strengthening mechanism provided by the reinforcement by the nanoparticles was intensely discussed by Ohji et al. (2002). This mechanism was applicable in the present case since Al_2O_3 nanoparticles were successfully yielded as distinct phase in the $YBa_2Cu_3O_{7-\delta}$ samples. Al_2O_3 nanoparticles are known as hard material which is capable to interact with dislocations in $YBa_2Cu_3O_{7-\delta}$ grains and consequently, prevent the dislocations movements during indentation. In addition, well distribution of Al_2O_3 nanoparticles in the samples achieved by auto-combustion reaction resulted in uniform microhardness. The hardening mechanism was maximized in sample with $x_{mol} = 0.06$ as more dislocation movements were restricted by more numbers of Al_2O_3 nanoparticles.

Further increment of Al_2O_3 with $x_{mol} > 0.06$ caused the Al_2O_3 nanoparticles to be agglomerated at $YBa_2Cu_3O_7$ inter-particles. Hence, the microhardness was increased at that particular region only. Meanwhile, the microhardness at the inner part of $YBa_2Cu_3O_7$ grains remained low because it was not reinforced by Al_2O_3 nanoparticles. The dislocations within the $YBa_2Cu_3O_{7-\delta}$ particles were allowed to move during indentation In addition, Zhang et al. (2007) suggested that the decrease of microhardness was due to the alteration of $YBa_2Cu_3O_{7-\delta}$ structure by Al^{3+} ions which introduced ductility. These resulted in a broad range of microhardness value as depicted by longer error bars in samples with $x_{mol} = 0.08$ and 0.10.

5.4 Electrical resistivity and critical temperature (T_C) analysis

Temperature dependence resistivity of each sample is shown in Figure 5.22.

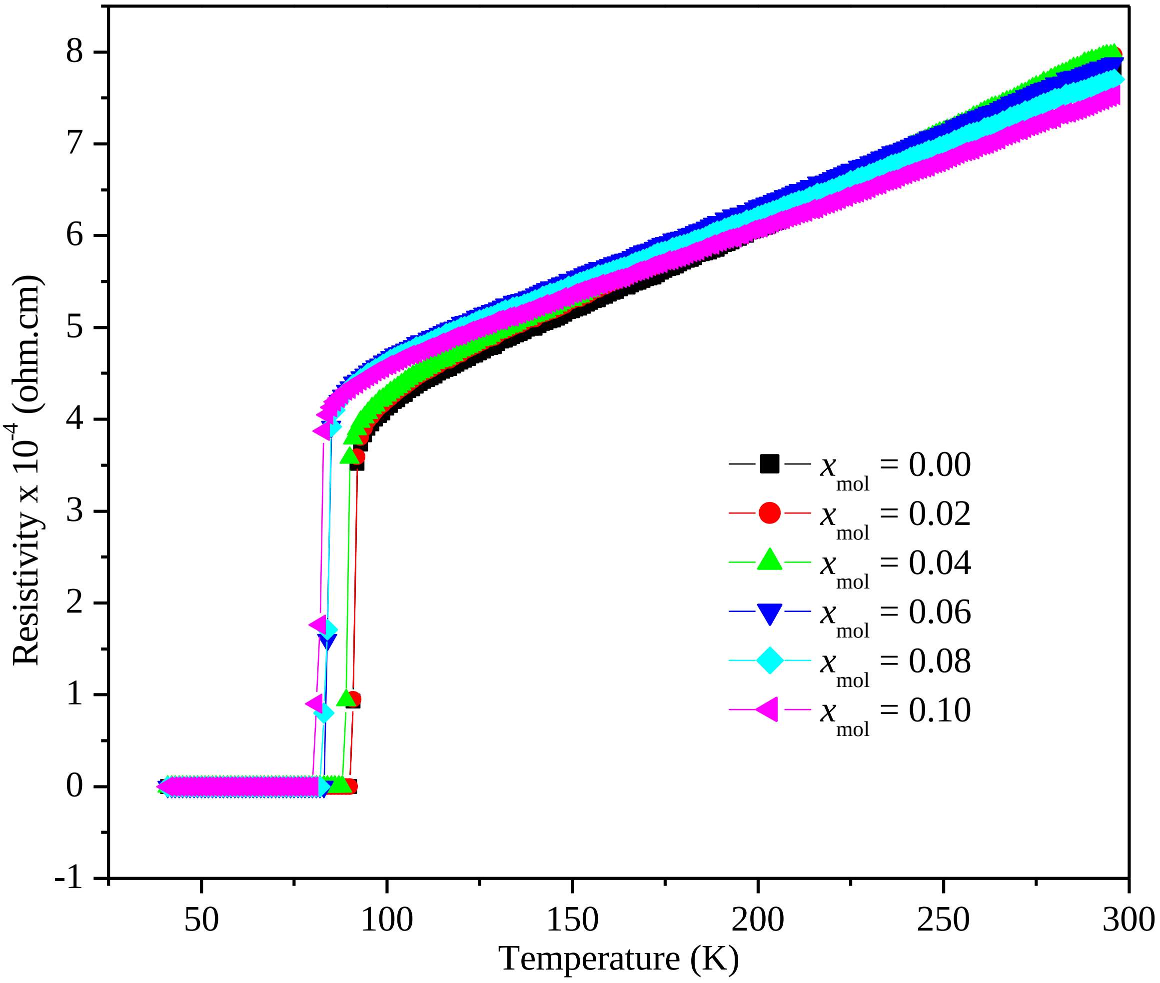

Figure 5.22: Temperature dependence resistivity of un-added and Al_2O_3 added $YBa_2Cu_3O_{7-\delta}$ samples.

In this figure each sample achieved zero electrical resistance by the same pattern. At 300 K, resistivity of the samples was around 0.8 mΩ. It constantly reduced as the temperature was decreased and suddenly dropped to zero at respective T_C onset. This rapid drop was occurred with a narrow temperatures width. From this decrement pattern, it was revealed that each sample behaved like metallic material before transforming to superconducting material after T_C onset. Close observation at the transition temperatures was shown in Figure 5.23.

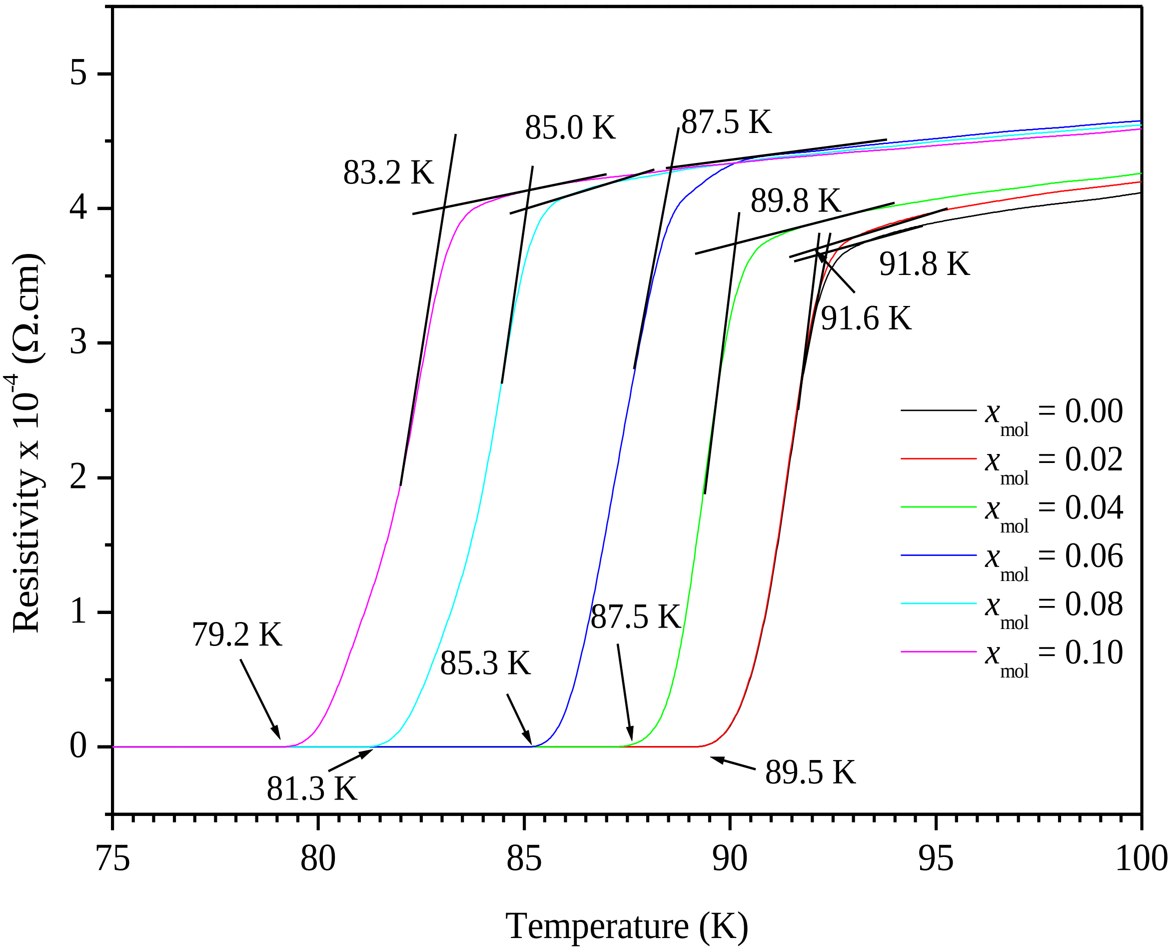

Figure 5.23: Critical temperatures of un-added and Al_2O_3 added $YBa_2Cu_3O_{7-\delta}$ samples.

Figure 5.23 shows the T_C onset and T_C zero of the samples. It was observed that both T_Cs were decreased with increasing the content of Al_2O_3 nanoparticles. T_C onset for sample with x_{mol} = 0.02 is 91.6 K which appeared to be slightly lowered compared to the pure $YBa_2Cu_3O_{7-\delta}$ sample. Yet, both of these samples possessed similar T_C zero of 89.5 K. The T_C onset for samples with x_{mol} = 0.04, 0.06, 0.08 and 0.10 were 89.8 to 86.5 to 85.0 to 83.2 K, respectively while their T_C zero were 87.5, 84.3, 81.3 and 79.2 K, respectively. The samples with $x_{mol} \leq 0.06$ were observed to have narrow transition temperature widths with value < 3 K. Instead samples with $x_{mol} > 0.06$ have wider transition temperature widths which are more than 3 K. Although the T_C zero of Al_2O_3 added $YBa_2Cu_3O_{7-\delta}$ samples had a decreasing pattern but in all cases it remained above the liquefy temperature of nitrogen (77 K).

From the results of the temperature dependence resistivity relationship of each sample, it was determined that the T_C of $YBa_2Cu_3O_{7-\delta}$ superconductor was reduced due to two factors. Firstly, the introduction of Al_2O_3 nanoparticles as non-superconducting material in the samples and secondly, the alteration of $YBa_2Cu_3O_{7-\delta}$ lattice by the incorporated Al ion. Al_2O_3 nanoparticles are known as non-superconducting material which forbids superconducting electron to pass through. Existence of Al_2O_3 nanoparticles on the $YBa_2Cu_3O_{7-\delta}$ grains thus obstructed superconducting electrons to flow smoothly. In order to surpass those obstacles and to achieve ideal flowing condition, the superconducting electrons were required lower temperature (Pathack et al., 2007). Furthermore, though this factor lowers the T_C but the superconducting transition width remained narrow. The samples rapidly achieved the state of zero resistance after the obstacles were surpassed. This effect was minimized if the Al_2O_3 nanoparticles were well distributed as in samples with $x_{mol} \leq 0.06$ which in agreement with Antal et al. (2007). The T_Cs for sample with $x_{mol} = 0.02$ was similar with the pure $YBa_2Cu_3O_{7-\delta}$ sample. It continuously decreased by 2 K with the increment of each 0.02 mol of Al_2O_3 nanoparticles until $x_{mol} = 0.06$. On the other hand, T_Cs for sample with $x_{mol} > 0.06$ were obviously decreased due to the agglomeration of Al_2O_3 nanoparticles and involved with the secondary factor. Agglomeration of Al_2O_3 nanoparticles at $YBa_2Cu_3O_{7-\delta}$ inter-particles has created high density of Al^{3+} region. As discussed in Sections 5.2 and 5.3, Al^{3+} ion was believed to diffuse into $YBa_2Cu_3O_{7-\delta}$ structure at the particles boundaries during sintering and heat treatment process. This was followed by the alteration of $YBa_2Cu_3O_{7-\delta}$ structure where Al^{3+} ion replaced a fraction of Y site. The oxygen deficiencies and orthorhombicity of samples were significantly affected by the incorporation of Al^{3+} into the Y sites. Higher oxygen content and lower orthorhombicity thus resulted in the degradation of superconductivity and obvious lowering of the T_C value with wider transition width Mellekh et al. (2007).

5.5 Magnetic hysteresis and critical current density (J_C) analysis

Field dependent magnetization, M-H hysteresis loops for $YBa_2Cu_3O_{7-\delta}$ and Al_2O_3 added $YBa_2Cu_3O_{7-\delta}$ samples measured at 5 and 77 K are shown in Figures 5.24 and 5.25, respectively.

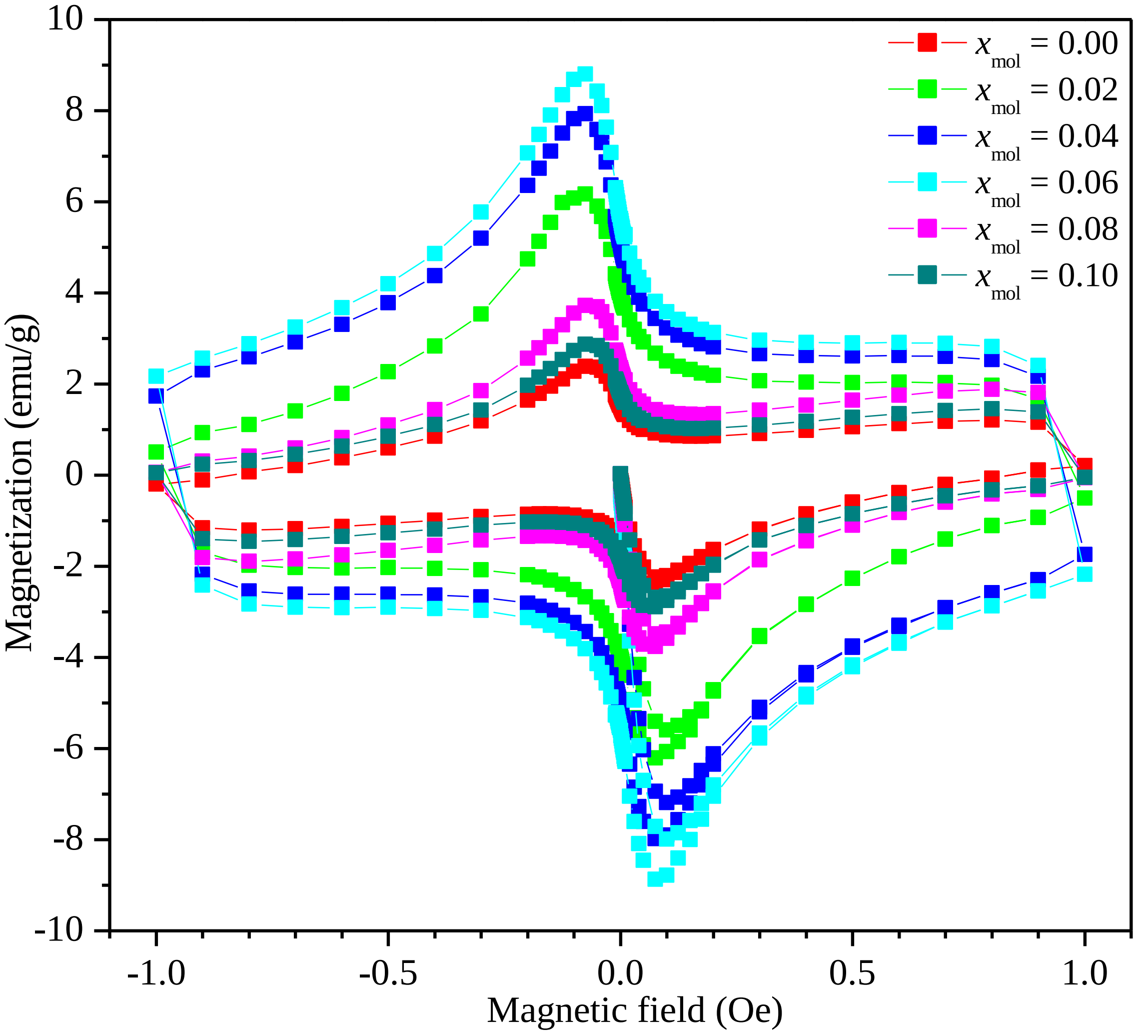

Figure 5.24: Field dependent magnetization, M-H hysteresis loop of un-added and Al_2O_3 added $YBa_2Cu_3O_{7-\delta}$ samples at 5 K.

In Figure 5.24, it is observed that each sample had fish tail-shaped M-H hysteresis loops at 5 K. The loops were existed with significant gaps at forward and reverse magnetic fields. It was seen that the loop of $YBa_2Cu_3O_{7-\delta}$ was altered by the addition of Al_2O_3 nanoparticles additions. The magnetization gaps were significantly wider for samples with x_{mol} = 0.02 and 0.04 and maximized in sample with x_{mol} = 0.06 where the loop became 4 times larger than the loop of pure $YBa_2Cu_3O_{7-\delta}$ sample. Then the M-H hysteresis loops were reduced by further addition of Al_2O_3 in samples with x_{mol} = 0.08 and 0.10. Magnetization gaps for these samples were narrower yet slightly wider compared to pure $YBa_2Cu_3O_{7-\delta}$ sample.

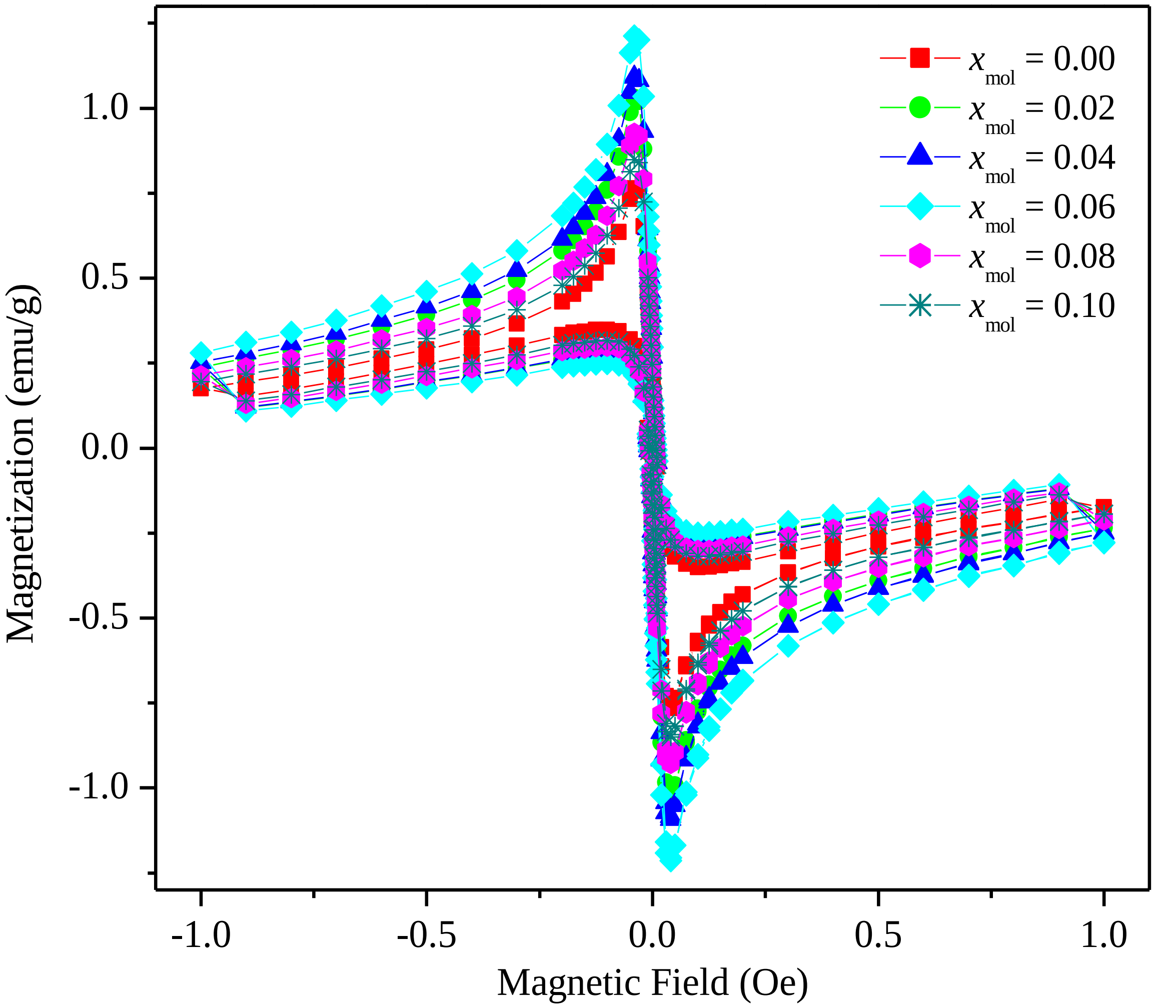

Figure 5.25: Field dependent magnetization, M-H hysteresis loop of un-added and Al_2O_3 added $YBa_2Cu_3O_{7-\delta}$ samples at 77 K.

Figure 5.25 shows the M-H hysteresis loop of each sample with slimmer pattern at 77 K. The magnetization gaps were narrower at applied magnetic field of -1.0 and 1.0 Oe. The loop size was increased with the addition of Al_2O_3 nanoparticles even though the increment was small. Sample with x_{mol} = 0.06 had the largest loop. With further increment of Al_2O_3 with x_{mol} = 0.08 and 0.10, the loop size was decreased. However, the loops of these samples were larger compared with the pure $YBa_2Cu_3O_{7-\delta}$ sample.

Based on results from field dependent magnetization M-H hysteresis loop of each sample, it was determined that all samples were capable to store and repel infiltrated magnetic flux at $T < T_C$ zero. This ability is one of the most important characteristics of superconducting material and controlled by the operating temperature and existence of pinning centre materials (Krabbes et al., 2008). At 5 K, where $T << T_C$ zero, higher amount of magnetic flux can be stored in the samples thus produced larger gap at forward and reverse magnetic field. However, at 77 K where $T \leq T_C$ zero, the loops were slimmer due to lack of trapped flux. These phenomena was attributed to increase the H_{C1} value at lower temperature as shown in Equation (2.1); hence, increase the ability of sample to contain larger flux before the superconductivity brake down.

On the other hand, addition of Al_2O_3 nanoparticles in $YBa_2Cu_3O_{7-\delta}$ samples also improved the ability to trap magnetic field thus resulted in larger M-H hysteresis loops. In samples with $x_{\mathrm{mol}} \leq 0.06$, higher amount of flux were trapped. Wider magnetization gap of M-H hysteresis loop of these samples indicated the increase of irreversible magnetic fluxes in the samples as suggested by Bean model. It was believed that well distribution of Al_2O_3 nanoparticles in samples with $x_{\mathrm{mol}} \leq 0.06$ pinned the magnetic fluxes from wiped out during reverse magnetic field. The pinning force was continued to increase as the amount of Al_2O_3 nanoparticles were increased which was maximized in sample with $x_{mol} = 0.06$.

Instead, samples with $x_{mol} \geq 0.08$ were only able to contain smaller amount of irreversible flux and just slightly higher than pure $YBa_2Cu_3O_{7-\delta}$ sample. Although these samples were synthesized with higher amount of Al_2O_3 composition, the trapped fluxes stayed lower. This was attributed to the fact that most of the Al_2O_3 in these samples were existed as agglomerated nanoparticles. Magnetic flux was only pinned if the size of the nanoparticles had similar coherence length of $YBa_2Cu_3O_{7-\delta}$ (Zhang et al., 2007). Therefore, the nanoparticles must have the size below 50 nm to pin the flux effectively. However, it appeared that the Al_2O_3 nanoparticles was agglomerated and formed larger particles thus unable to pin most of the fluxes. The increased amount of Al_2O_3 agglomerated in sample with $x_{mol} = 0.10$ resulted in the lowest irreversible trapped flux compared with other Al_2O_3 added $YBa_2Cu_3O_{7-\delta}$ samples.

The effects of Al_2O_3 nanoparticles seemed more apparent for the field dependent magnetic J_C graph. Magnetic J_C of $YBa_2Cu_3O_{7-\delta}$ and Al_2O_3 added $YBa_2Cu_3O_{7-\delta}$ samples at 5 and 77 K are shown in Figures 5.26 and 5.27 respectively.

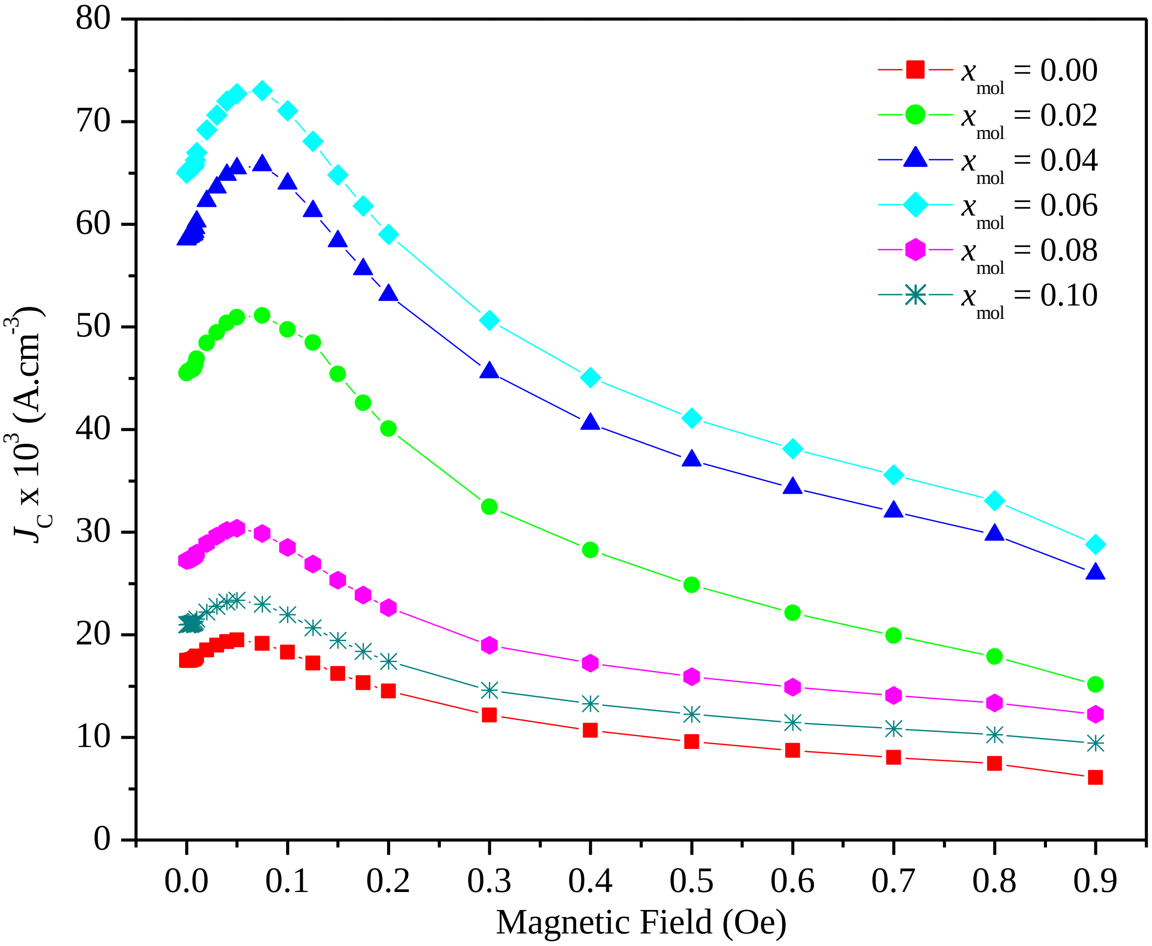

Figure 5.26: Magnetic J_C of un-added and Al_2O_3 added $YBa_2Cu_3O_{7-\delta}$ samples at 5 K.

In Figure 5.26, it is observed that the J_Cs for pure $YBa_2Cu_3O_{7-\delta}$ sample were lowest for the applied magnetic fields in the range from 5 to 20 k A·cm^{-3}. It was significantly increased in Al_2O_3 added samples. The J_Cs in samples with x_{mol} = 0.02 and 0.04 were in the range of 17 to 50 k A·cm^{-3} and 30 to 65 k A·cm^{-3}, respectively. It was maximized in the sample containing 0.06 mol where the J_C value was quadrupled compared with pure $YBa_2Cu_3O_{7-\delta}$ and it was in the range from 40 to 80 k A·cm^{-3} at verified magnetic field. The J_Cs were decreased with further addition of Al_2O_3 nanoparticles in samples with x_{mol} = 0.08 and 0.10. It appeared that the J_Cs of each sample were decreased when the applied magnetic field was increased. The J_Cs for samples with x_{mol} = 0.02, 0.03 and 0.06 were decreased with steeper slope compared to samples with x_{mol} = 0.00, 0.08 and 0.10.

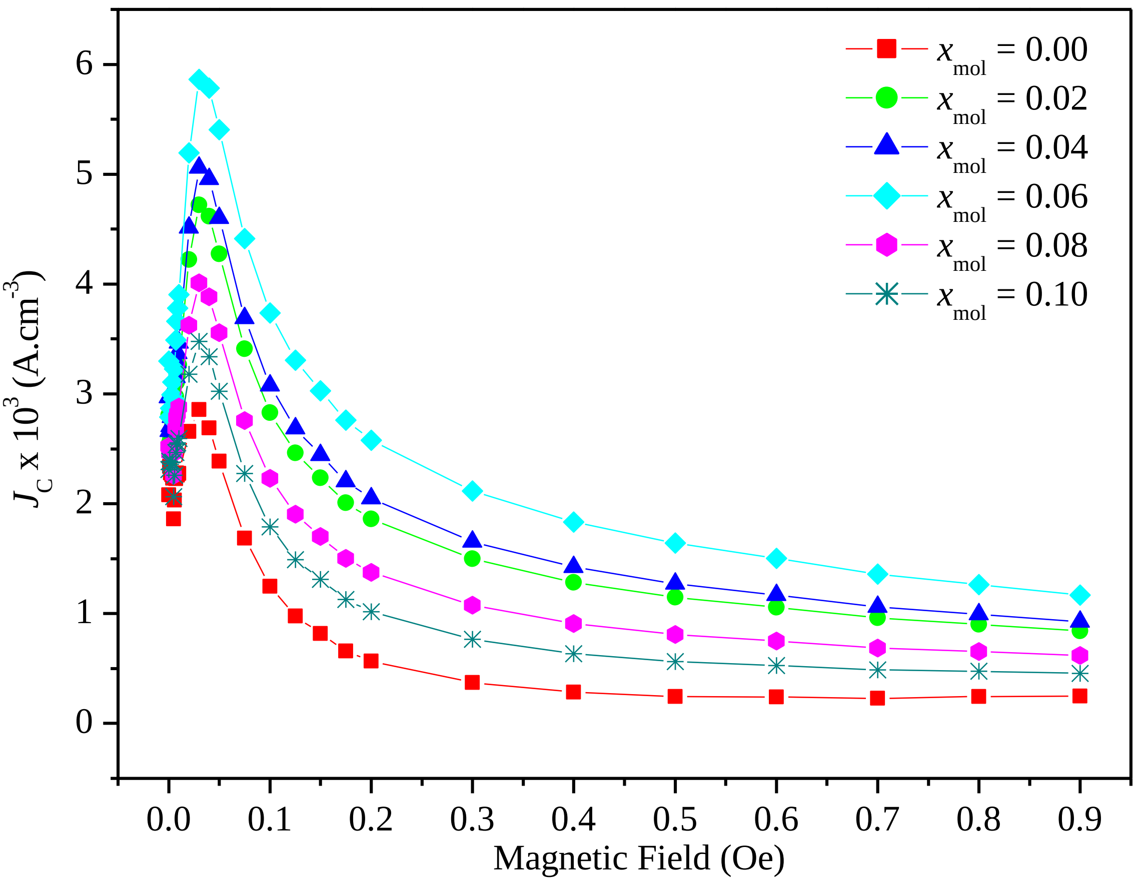

Figure 5.27: Magnetic J_C of un-added and Al_2O_3 nanoparticles added $YBa_2Cu_3O_{7-\delta}$ samples at 77 K.

Figure 5.27 shows the magnetic J_C of each sample at 77 K where the J_C was observed to decrease as the applied magnetic field was increased. The J_Cs of pure $YBa_2Cu_3O_{7-\delta}$ sample were decreased from it highest value of 3 A·cm^{-3} then stabilized at 0.5 k A·cm^{-3}. This decrement pattern was similar for each Al_2O_3 added sample but with higher J_Cs. The J_Cs for samples with x_{mol} = 0.02, 0.04 and 0.06 were significantly increased. The highest J_C at 77 K was about 6 k A·cm^{-3} achieved by sample with x_{mol} = 0.06 is much higher compare to other Al_2O_3 added $YBa_2Cu_3O_{7-\delta}$ reported by Mellekh et al., (2007), Moutalibi et al. (2009) and Albis et al. (2011). Addition of Al_2O_3 nanoparticles by this amount doubled the J_C of pure $YBa_2Cu_3O_{7-\delta}$ sample. On the other hand, J_Cs for samples with x_{mol} = 0.08 and 0.10 were slightly higher than the pure $YBa_2Cu_3O_{7-\delta}$ sample though with higher Al_2O_3 nanoparticles content.

The J_C observed at zero magnetic field of each sample is shown in Figure 5.28. The sample with x_{mol} = 0.06 possessed the highest J_C followed by x_{mol} = 0.04, 0.02, 0.08, 0.10 and 0.00.

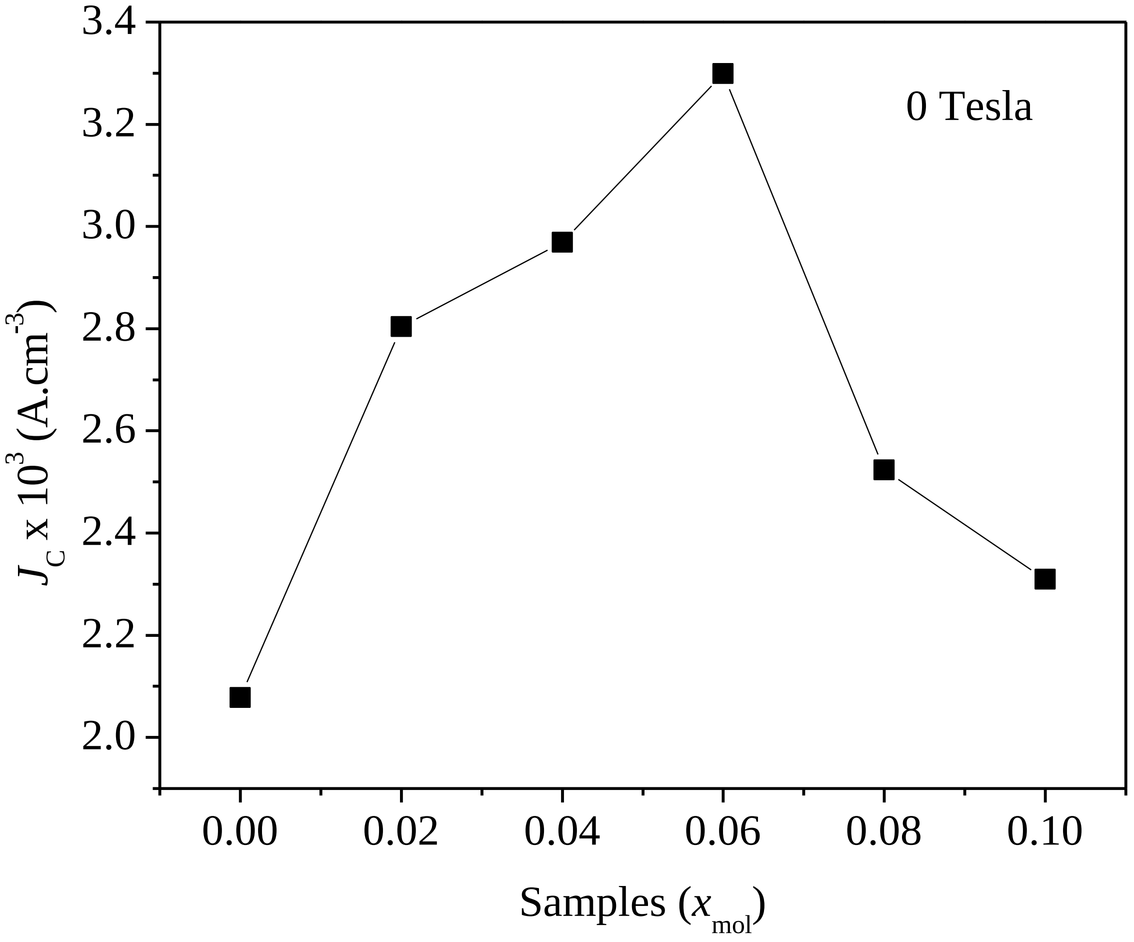

Figure 5.28: J_C of un-added and Al_2O_3 added $YBa_2Cu_3O_{7-\delta}$ samples at 77K.

Magnetic J_C in the Al_2O_3 added $YBa_2Cu_3O_{7-\delta}$ samples were enhanced as more magnetic fluxes were prevented to move. By referring to the field dependent magnetization M-H hysteresis loop, these fluxes were irreversible thus unable to be cancelled out during forward and reverse magnetic field. These infiltrated fluxes was strongly pinned by Al_2O_3 nanoparticles thus allowed higher density of electrical current to flow in the samples without exceeding the Lorentz force, F_L.

In samples with $x_{\mathrm{mol}} \leq 0.06$, well distributed Al_2O_3 nanoparticles efficiently pinned the fluxes and significantly increased the magnetic J_C. While the J_C was lowered in samples with $x_{\mathrm{mol}} \geq 0.08$ due to the fact that the agglomerated Al_2O_3 nanoparticles was not capable to efficiently pin the fluxes. However, the J_C of these samples was remained higher compared to the pure $YBa_2Cu_3O_{7-\delta}$ sample which can be attributed from two mechanisms. Firstly, the existence of Al_2O_3 nanoparticles which stayed well distributed and secondly, the improved connectivity among the grain boundaries (Mellekh et al., 2007). Though most of the Al_2O_3 nanoparticles of these samples were agglomerated, there must be small amount of nanoparticles which existed individually and capable to trap the fluxes. As for the second factor, agglomeration of Al_2O_3 nanoparticles developed a molten-like structure at the inter-grain of $YBa_2Cu_3O_{7-\delta}$. This structure was linked and connected with each and every grain with low angle boundaries hence eased the electrical current to flow through the grains and thus the J_C was increased (Gurevich et al., 1998). However, the effect of this mechanism was minor since serious weak link existed in polycrystalline $YBa_2Cu_3O_{7-\delta}$ sample.

5.6 Discussions

The Al_2O_3 nanoparticles were yielded into $YBa_2Cu_3O_{7-\delta}$ superconductor through citrate-nitrate auto-combustion reaction. The $Al(NO_3)_3$ added precursor gel was decomposed by two distinct reactions where the Al_2O_3 ashes was firstly produced at around 200 °C followed by Y_2O_3, BaO and CuO ashes at around 240 °C. These amorphous ashes were transformed to crystalline structure during calcination process. After this process, Al_2O_3 was existed as thermally stable phase which did not involve in further formation of $YBa_2Cu_3O_{7-\delta}$ phase.

The formation of Al_2O_3 phase in the samples was not solidly confirmed as it assigned peaks in the XRD pattern were very small and indistinguishable with background peaks. However, alterations of $YBa_2Cu_3O_{7-\delta}$ structure of each sample, especially in samples with $x_{mol} \geq 0.08$ might be evidence of the existence of Al_2O_3 phase. Though the $YBa_2Cu_3O_{7-\delta}$ structure was altered but the orthorhombicity of each sample was preserved. The samples were determined to have polycrystalline structure with crystallite size around 50 nm. From microstructural observation, it occurred that Al_2O_3 was existed as nanoparticles and well distributed in $YBa_2Cu_3O_{7-\delta}$ samples with $x_{mol} \leq 0.06$. Instead it was agglomerated and able to supply Al^{3+} ion to the Y sites of $YBa_2Cu_3O_{7-\delta}$ in samples with $x_{mol} \geq 0.08$. Existence of Al_2O_3 nanoparticles and diffusion of Al^{3+} ion into $YBa_2Cu_3O_{7-\delta}$ structure was confirmed by EDX analysis.

The samples with $x_{mol} \leq 0.06$ possessed higher microhardness compare with other samples due to well distribution of Al_2O_3 nanoparticles. These nanoparticles prevented the dislocation movement at inter and intra $YBa_2Cu_3O_{7-\delta}$ grains. As for the incorporation of $x_{mol} \geq 0.08$ Al into the $YBa_2Cu_3O_{7-\delta}$ structure introduced ductility.

The T_C was decreased in Al_2O_3 added samples due to the existence of non-superconducting nanoparticles in $YBa_2Cu_3O_{7-\delta}$ which hindered the superconductivity. However the decrement was minimized if the Al_2O_3 nanoparticles were well distributed in the sample. Well distribution of Al_2O_3 nanoparticles was optimized in sample with $x_{mol} = 0.06$ and enhanced the magnetic J_C to double of pure $YBa_2Cu_3O_{7-\delta}$ by the strongly pinned the magnetic fluxes. Grain-boundaries quality improvement by agglomerated Al_2O_3 was another possible reason for enhanced J_C, however, serious weak link was existed in polycrystalline sample.

CHAPTER 6

CONCLUSIONS AND FUTURE WORKS

6.1 Conclusions

The conclusions are made based on the results and discussions in Chapter 4 and Chapter 5 which achieved the objectives stated in Chapter 1. It is detailed as following:

1. *Effects of citrate-nitrate ratio.*

The $YBa_2Cu_3O_{7-\delta}$ superconductor was successfully synthesized via citrate-nitrate auto-combustion reaction. Selection of c/n = 0.7 resulted in complete decomposition of precursor gel thus produced purer $YBa_2Cu_3O_{7-\delta}$ phase. This sample possessed higher T_C zero at around 91.2 K. Extremely higher or lower c/n compared to this value produced impurities in $YBa_2Cu_3O_{7-\delta}$ sample which resulted in reduction of T_C.

2. *Effects of the addition of Al_2O_3 nanoparticles.*

Al_2O_3 particles with size around ~10 nm were successfully synthesized and evenly distributed on superconducting $YBa_2Cu_3O_{7-\delta}$ via citrate-nitrate auto-combustion reaction. Combustion characteristics were nearly similar for each gel samples where two exothermic peaks were detected attributed from the decomposition of $Al(NO_3)_3$ to Al_2O_3 and Y, Ba, Cu nitrates to Y_2O_3, $BaCO_3$ and CuO. Calcination of these oxides yielded $YBa_2Cu_3O_{7-\delta}$ and Al_2O_3 phase in the samples. Increased amount of Al_2O_3 nanoparticles in the samples improved the properties of $YBa_2Cu_3O_{7-\delta}$. Sample with x_{mol} = 0.06 had the optimum mechanical, superconducting and magnetic properties. The microhardness of this sample was about 300 MPa. It possessed slightly lower T_C zero of

85.3 K but the highest J_C of 6 k A·cm^{-2} at 77 K compared with pure $YBa_2Cu_3O_{7-\delta}$ sample. With this composition, existence of well distributed Al_2O_3 nanoparticles did not affect the T_C in much extent but obviously increased the J_C by pinning the fluxes as a contribution of second phase particles mechanism. Further increased of Al_2O_3 composition to x_{mol} = 0.10 resulted in agglomeration of nanoparticles. These agglomerated Al_2O_3 nanoparticles were unable to act as efficient pinning centre material.

6.2 Future works

The success of this research works can be continued with further investigations on the effects of Al_2O_3 nanoparticles towards other properties of the samples. These investigations will help to further understand the mechanisms of superconducting properties of $YBa_2Cu_3O_{7-\delta}$ by the addition of nanoparticles. For evaluating the bonding among the atoms of the gel and synthesized samples, the suggested techniques could be Raman spectroscopy and Fourier Transform Infrared (FTIR) analsysis. The permittivity and permeability measurement could be used to evaluate its optical properties. Another mechanical characterization such as ductility test is important to evaluate the ability of this composite structure to be pressed and stretched into thin cable. In addition, transport analysis of the samples is good improvisation to investigate the capability of carrying current density at inter grains.

On the continuum of using citrate-nitrate auto-combustion reaction, other nanoparticles could be synthesized into $YBa_2Cu_3O_{7-\delta}$ to act as efficient pinning centre materials. On the other hand, Al_2O_3 nanoparticles could be yielded into other superconductor matrix. The suggested nanoparticles are ZrO_2 and SiO_2. This is due to thermal stability of these oxides at higher temperature and capability to synthesize in nanometer size. While suggested superconductor matrixes are YBa-Cu-O and BiSrCuO variants since these types of superconductor have higher T_C and comparable properties with $YBa_2Cu_3O_{7-\delta}$.

REFERENCES

Albiss B. A., Al-Rawashdeh N., Jabal A. A., Gharaibeh M., Obaidat I. M., Hasan (Qaseer) M. K., & Azez K. A. (2010). Polycrystalline $YBa_2Cu_3O_{7-\delta}$ with Nano-sized Al_2O_3 Inclusions. *Journal of Superconductor Novel Magnetism*, 23, 1333-1340.

Antal V., Kaˇnuchov´a M., Sefˇcikov´a M., Kov´aˇc J., Diko P.,Eisterer M., H¨orhager N., Zehetmayer M., Weber H. W., & Chaud X. (2009). Flux pinning in Al doped TSMG YBCO bulk superconductors, *Superconductor Science and Technology*, 22, 1-7.

Aranson I. S., & Kramer L. (2002). The world of the complex Ginzburg-Landau equation. *Reviews of Modern Physics,* 74, 99-143.

Aruna S. T., Muthuraman M., & Patil K. C. (1999). Synthesis and properties of Ni-YSZ cermet: anode material for solid oxide fuel cells. *Solid State Ionics*, 111, 45-51.

Aruna S. T. & Mukasyan A. S. (2008). Combustion synthesis and nanomaterials. *Current Opinion in Solid State and Materials Science*, 12, 44–50.

Azzouz F. B., Zouaoui M., Mellekh A., Annabi M., Tendeloo G. V., & Ben Salem M. (2007). Flux pinning by Al-based nanoparticles embedded in YBCO: A transmission electron microscopic study. *Physica C: Superconductivity and its applications,* 455, 19-24.

Baldha G. J., Shaikh I. A., Kuberkar D. G., Bhalodia J. A., Joshi U. S., & Kulkarn R. G. (1995). Enhanced flux pinning and critical currents by Hf and Hf-Ca substitution in $YBa_2Cu_3O_{7-\delta}$. *Cryogenics,* 35, 61-65.

Banerjee S., & Devi P. S. (2007). Effect of citrate to nitrate ratio on the decomposition characteristics and phase formation of alumina. *Journal of Thermal Analysis and Calorimetry,* 90, 699–706.

Bardeen J., Cooper L. N., & Schrieffer J. R.. (1957). Microscopic theory of superconductivity. *Physical Review*, 106, 162–164.

Beans C. P. (1964). Magnetization of high-field superconductor. *Reviews of Modern Physics*, 31-39.

Beyers R., Ahn B. T., Gorman G., Lee V. Y., Parkin S. S. P., Ramirez M. L., Roche K. P., Vazquez J. E., Gür T. M., & Huggins R. A. (1989). Oxygen ordering, phase separation and the 60-K and 90-K plateaus in $YBa_2Cu_3O_x$. *Nature*, 340, 619-621.

Bhaduri S., Zhou E. & Bhaduri S.B. (1996). Auto ignition processing of nanocrystalline α-Al_2O_3 *Nanostructucture Material,* 7, 487-496.

Bhargava, A., Mackinnon, Ian D. R., Yamashita, T., & Page, D. (1995) Bulk manufacture of YBCO powders by coprecipitation. *Physica C: Superconductivity and its applications,* 241, 53-62.

Bhattacharya D., Pathak L.C., Mishra S. K., Sen D., & Chopra K.L. (1990). Pyrophoric synthesis technique for multicomponent high-temperature superconductors. *Applied Physics Letters*. 57, 2145.

Bowen C. R. & Derby B. (1996). The formation of TiC/Al_2O_3 microstructures by self-propagating high-temperature synthesis reaction. *Journal of Material Sciences*, 31, 3791–3803.

Brecht E., Schmahl W. W., Miehe G., Rodewald M., Fuess H., Andersen N. H., Hangmann J., Wolf T. T. (1996). *Physica C: Superconductivity and its applications,* 265, 53-66.

Cava R. J., Hewat A. W., Hewat E. A., Batlog B., Marezio M., Rabe K. M., Krajewski J. J., Peck W. F., & Rupp L. W. (1990). Structural anolmalies, oxygen ordering and superconductivity in oxygen deficient $Ba_2YCu_3O_x$. *Physica C: Superconductivity and its applications,* 165, 419-433.

Celebi S., Ozturk A.,Karaca I., & Kolemen U. (2000). The effect of potassium doping on resistive transitions and transport critical current of bulk YBCO high-Tc superconductors. *Turkey Journal of Physic*, 24, 567-576.

Chandradass J., & Kim K. H. (2009). Effect of acidity on the citrate-nitrate combustion synthesis of alumina-zirconia composite powder. *Metal Material International*, 15, 1039-1043.

Conder K. (2001). Oxygen diffusion in the superconductors of the YBa-Cu-O family: isotope exchange measurements and models. *Materials Science and Engineering*, R32, 41-102.

Crabtree G. W., Kwok W. K., Paulius L. M., Petrean A. M., Olsson R. J., Karapetrov G., Tobos V., & Moulton W. G. (2000). The effect of disorder on the critical points in the vortex phase diagram of YBCO. *Physica C: Superconductivity and its applications*, 332, 71-79.

Cyrot M. (1973). Ginzburg-Landau theory for superconductors, *Reports in Progress Physics*, 36, 103.

Deutscher G. & Bok J. (1993), Short coherence length superconductors and the Fermi velocity paradox, *Chinese Journal of Physics*, 31, 6-H.

Dew-Hughes D. (1974). Flux pinning mechanisms in type II superconductors. *Philosophical Magazine*, 30, 293.

Dew-Hughes D. (2001). The critical current of superconductors: an historical review. *Low Temperature Physics*, 27 (9-10), 713-722.

Erb A., Genoud J. Y., Walker E., & Flukiger R. (1998). Improvements in crystal growth and crystal homogeneity and its impact on physics. *Journal of Physics and Chemistry of Solids* 59, 2180-2184.

Flippen R. B., Askew T. R., Fendrich J. A., & Vanderbeek C. J. (1995). Surface flux pinning in $YBa_2Cu_3O_{7-\delta}$. *Physical Review B*, 52, 9882–9885.

Foltyn S. R., Civale L., MacManus-Driscoll J. L., Jia Q. X., Maiorov B., Wang H., Maley M. (2007). Materials science challenges for high-temperature superconducting wire. *Nature Materials*, 6, 631-642.

Giri R., Awana V. P. S., Singh H. K., Tiwari R.S., Srivastava O. N., Gupta A., Kumaraswamy B. V., & Kishan H. (2005). Effect of Ca doping for Y on structural/microstructural and superconducting properties of $YBa_2Cu_3O_{7-d}$. *Physica C: Superconductivity and its applications*, 419, 101-108.

Goswami R., Holtz R. l., Rupich M. W., & Spanos G. (2007). Formation of nanoparticles and defects in $YBa_2Cu_3O_{7-d}$ prepared by the metal organic deposition process. *Scripta Materialia*, 57, 797–800.

Grami M. E., & Munir Z. A. (1989). Effect of porosity on the combustion synthesis of titanium nitride. *Journal of American Ceramic Society*, 73, 1235-1239.

Gurevich A., & Pashitskii E A. (1998). Current transport through low-angle grain boundaries in high-temperature superconductors. *Physical Review B*, 57, 13878-13893.

Gyorgy E. M., Van-Dover R. B., Jackson K. A., Schneemeyer L. F., & Waszczak J. V. (1989). Anisotropic critical currents in $Ba_2YCu_3O_7$ analyzed using an extended Bean model. *Applied Physics Letters*, 55, 283-288.

Hakuta Y., Nagai N., Suzuki Y. H., Kodaira T., Bando K. K., Takashima H., & Mizukami F. (2013). Preparation of α-alumina nanoparticles with various shapes via hydrothermal phase transformation under supercritical water conditions. *IOP Conference Series: Materials Science and Engineering*, 47, 1-4.

He Z. H., Habisreuther T., Bruchlos G., Litzkendorf D., & Gawalek W. (2001). Investigation of microstructure of textured YBCO with addition of nanopowder SnO_2. *Physica C: Superconductivity and its applications*, 356, 272-284.

Hoke D. A., Kim D. K., LaSalvia J. C. & Meyers M. A. (1996). Combustion synthesis/dynamic densification of a TiB-SiC composite. *Journal of American Ceramic*, 79, 177-182.

Hon Y. M., Fung K. Z., & Hon M. H. (2001). Synthesis and characterization of Li1+δMn2-δO4 powders prepared by citric acid gel process. *Journal of European Ceramic Society*, 21, 515-522.

Ibrahim D.M., Khalil T. & Mostafa A.A. (1999). Densification of alumina produced by urea formaldehyde sol–gel polymeric route. *Ceramic International*, 25, 273.

Izumi F., & Momma K. (2007). Three-dimensional visualization in powder diffraction. *Solid State Phenomenon*, 130, 15-20.

Jain S. R., Adiga K. C., & Pai V. R. (1981). A New Approach to Thermochemical Calculations of Condensed Fuel-Oxidizer Mixtures. *Combustion Flame* 40, 71-79.

Juarez R. E., Lamas D. G., Lascalea G. E., & WalsoÈe de Reca N. E. (2000). Synthesis of nanocrystalline zirconia powders for TZP ceramics by a nitrate citrate combustion route. *Journal of the European Ceramic Society*, 20, 133-138.

Kani H., Awano K., Kodama M., & Takagi Y. (1991). Sol-Gel Synthesis and Sintering of Y-Ba-Cu-O Powder. *Ceramic Transaction*, 561.

Kishio K., Shimoyama J., Hasegawa T., Kitazawa K., & Fueki K. (1987). Determination of Oxygen Nonstoichiometry in a high-Tc superconductor $Ba_2YCu_3O_{7-d}$. *Japan Journal of Applied Physics*, 26, L1228-1230.

Kordas G. (1990). Sol-gel processing of ceramic superconductors. *Journal of Non Crystalline Solids,* 46, 436 – 442.

Krabbes G., Fuchs G., Canders W.R., May H., & Palka R. (2006). High temperature superconductor bulk materials. Weinheim: Wiley-VCH GmbH & Co. KGaA.

Kumar P., Pillai V., & Shah D. O. (1993). Preparation of $YBa_2Cu_3O_{7-x}$ superconductors by oxalate coprecipitation. *Journal of Materials Science Letters*, 12, 162–164.

Lee S. H., & Choi Y. (2009). Effect of oxide dopants on the superconducting properties of YBCO superconductor. *Physica B* ,404, 734–736.

Lei L., Zhao G., Xu H., Wu N., & Chen Y. (2011). Influences of Y_2O_3 nanoparticle additions on the microstructure and superconductivity of YBCO films derived from low-fluorine solution. *Materials Chemistry and Physics*, 127, 91–94.

Li J., Wu Y., Pan Y., & Guo J. (2007). Alumina precursors produced by gel combustion. *Ceramics International*, 33, 361–363.

Li J., Wu Y., Pan Y., & Guo J. (2007). Influence of citrate-to-nitrate ratio on the thermal behavior and chemical environment of alumina gel. *Ceramics International*, 33, 735–738.

Liu Z. G., Ye L. L., Guo J. T. Li G. S. & Hu Z. Q. (1995). Self propagating high-temperature synthesis of TiC and NbC by mechanical alloying. *Journal of Materials Research*, 10, 3129–3135.

London, F., & London H. (1935). The electromagnetic equations of the Supraconductor. *Proceedings of the Royal Society A: Mathematical, Physical and Engineering Sciences,* 149 (866), 71.

Langhorn J.B. (1996) Flux Pinning by Platinum and Rhodium in High Temperature Superconductors. *Platinum Metals Review*, 40, 64-69.

Mamalis A. G. (2000). Manufacturing of bulk high-T superconductors. *International Journal of Inorganic Materials*, 2, 623–633.

Manoharan S. S., & Patil K. C. (1992) Combustion synthesis of metal chromite powders. *Journal of American Ceramic Society*, 75 1012-1015.

Marinsek M., Kemperl J., Likozar B., & Macek J. (2008). Temperature profile analysis of the citrate-nitrate combustion system. *Indian Engineering Chemical Research*, 47, 4379–4386.

Matsushita T. (2007).Flux pinning in superconductors. Springer-Verlag Berlin Heidelberg.

Meissner W., & Ochsenfeld R. (1933). Ein neuer Effekt bei Eintritt der Supraleitfähigkeit. *Naturwissenschaften*, 21 (44), 787–788.

Mekasuwandumrong O., Pavarajarn V., Inoue M. & Praserthdam P. (2006). Preparation and phase transformation behavior of χ-alumina via solvothermal synthesis. *Material Chemistry and Physics*, 100, 445.

Mellekh A., Zouaoui M., Azzouz F.B., Annabi M., & Salem F.B. (2006). Nano-Al_2O_3 particle addition effects on $YBa_2Cu_3O_y$ superconducting properties. *Solid State Communication*, 140, 318–323.

Mellekh A., Zouaoui M., Azzouz F.B., Annabi M., & Salem F.B. (2007). Effect of nanometer Al_2O_3 addition on structural and transport properties of $YBa_2Cu_3O_{7-d}$. *Physica C: Superconductivity and its applications*, 460–462, 426–427.

Mirjalili F., Hasmaliza M., & Abdullah L. C. (2010). Size-controlled synthesis of nano α-alumina particles through the sol-gel method. *Ceramics International*, 36, 1253-1257.

Mishra S.K., & Pathak L.C. (2005). A review on the synthesis of Y–Ba–Cu-oxide powder. *Superconductor Science and Technology*, 18, R67–R89.

Momma K. & Izzumi F. (2011). VESTA 3 for three-dimensional visualisation of crystal, volumetric and morphology data, *Journal of Applied Crystallography*, 44, 1272-1276.

Moore J. J., & Feng H. J. (1995). Combustion synthesis of advanced materials: Part I. reaction parameters. *Progress in Materials Science*, 39, 243-273.

Moore J. J., & Feng H. J. (1995). Combustion synthesis of advanced materials: Part II. Classification, applications and modelling. *Progress in Materials Science*, 39, 275-316.

Moutalibi N. & M'chirgui A. (2009). Embedding of insulating nano-inclusions in Y-123 superconductor as pinning centers: The influence of size. *Physica C: Superconductivity and its applications*, 469, 95-101.

Moutalibi N., & M'chirgui A. (2007). Improved flux pinning behavior in bulk YBCO achieved by nano-alumina addition. *Journal of Physics: Conference Series 97*, 012284.

Mueller K. A. & Bednorz J.G. (1986). Possible high T_C superconductivity in the Ba-La-Cu-O system. *Zeitschrift für Physik B*, 189–193.

Murakami M., Fujimoto H., Gotoh S., Yamaguchi K., Koshizuka N., & Tanaka S. (1991). Flux pinning due to nonsuperconducting particles in melt processed YBa-Cu-O superconductors. *Physica C: Superconductivity and its applications*, 185-189, 321-326.

Murakami M., Yamaguchi K., Fujimoto H., Nakamura N., Taguchi T., Koshizuka N., & Tanaka S. (1992). Flux pinning by non-superconducting inclusions in melt-processed YBa-Cu-O superconductors. *Cryogenics*, 32, 930-935.

Murakami. M. (1992). Processing of bulk YBa-Cu-O. *Superconductor Science and Technology* 5, 185-203.

Ohji T., Jeong Y. K., Choa Y. H., & Niihara K. (1998). Strengthening and toughening mechanisms of ceramic nanocomposites, *Journal of American Ceramic Society*, 81, 1453-1458.

Onnes, H. K. (1911). The resistance of pure mercury at helium temperatures. *Communication Physics Lab. Univ. Leiden 12*, 120.

Ossandon J. G., Thompson J. R., Christen D. K., Sales B. C., Kerchner H. R., Thompson J. O., Sun Y. R., Lay K. W., & Tkaczyk J. E. (1992). Influence of oxygen deficiency on the superconducting properties of grain-aligned $YBa_2Cu_3O_{7-d}$. *Physical Review B*, 45 (21), 534-547.

Ozturk K., Celik S., Cevik U., & Yanmaz E. (2007). The effect of Gd diffusion-doped on structural and superconducting properties of $YBa_2Cu_3O_{7-x}$ superconductors. *Journal of Alloys and Compounds*, 433, 46–52.

Pathak L. C., Mishra S. K., Bhattacharya D., & Chopra K. L. (2004). Synthesis and sintering characteristics of Y–Ba–Cu-oxide superconductors. *Materials Science and Engineering B*, 110, 119–131.

Pathak L. C., Singh T. B., Das S., Verma A. K., & Ramachandrarao P. (2002). Effect of pH on the combustion synthesis of nano-crystalline alumina powder. *Materials Letters*, 57, 380–385.

Peng T, Liu X., Dai K., Xiao J., & Song H. (2006). Effect of acidity on the glycine–nitrate combustion synthesis of nanocrystalline alumina powder. *Materials Research Bulletin*, 41, 1638-1641.

Piriyawong V., Thongpool V., Asanithi P., & Limsuwan P. (2012). Preparation and characterization of alumina nanoparticles in deionized water using laser ablation technique, *Journal of Nanomaterials*, 1-6.

Plesch G., Van Driessche I., Cigáň A., Maňka J., Hoste S., & Kliment J. (2001). Magnetic properties of superconducting $YBa_2Cu_3O_{7-\delta}$/Ag composites prepared by various techniques. *Measurement Science Review*, 1, 33-36.

Raveau B., Michel C., Hervieu M. & Provost J. (1988). Crystal chemistry of perovskite superconductors. *Physica C: Superconductivity and its applications*, 3, 153-155.

Reid C. B., Forrester J. S., Goodshaw H. J., Kisi E. H., & Suaning G. J. (2008). A study in the mechanical milling of alumina powder. *Ceramics International*, 34, 1551-1556.

Roslan A.S. (2004). Introduction to superconductivity in metals, alloys & cuprates. Tanjung Malim: Universiti Pendidikan Sultan Idris.

Rupp B.,Wong J., Holt J. B., & Waide P. (1994). The solid combustion synthesis of small $REBa_2Cu_3O_x$ samples (RE=Y, Er). *Journal of Alloys and Compounds*, 209, 25-33.

Seeley Z., Choi Y. J., & Bose S. (2009). Citrate–nitrate synthesis of nano-structured titanium dioxide ceramics for gas sensors. *Sensors and Actuators B*, 140, 98–103.

Sen D., Ghatak S. K., Chopra K. L., & Bhattacharya D. (1991). Critical current density and magnetic behaviour of superconducting $YBa_2Cu_{3+y}O_{7-d}$: Ag_x composite. *Journal of Physical Condensed Matter*, 3, 1181-1187.

Sharma D.A., Basu R. N., & Maiti H. S. (1992). Control of Cation Stoichiometry During Preparation of $YBa_2Cu_3O_x$ Superconductor By The Oxalate Precipitation Technique. *Journal of Material Science Letter,* 11, 122-124.

Shi, J. L., Deguchi, Y., & Sakabe, Y. (2005). Relation between grain growth, densification and surface diffusion in solid state sintering - a direct observation. *Journal of Materials Science,* 40 (21), 5711.

Singal R. K. (2011). A comparative study of Pr substitution at Y and Ba sites in $YBa_2Cu_3O_{7-\delta}$. *Materials Letters,* 65, 825-827.

Siegrist T., Schneemeyer L. F., Waszczak, J. V., Singh N. P., Opila R. L., Batlogg B., Rupp L. W., & Murphy D. W (1987). Aluminum substitution in $Ba_2YCu_3O_7$, *Physical Review B,* 36, 8365-8369.

Singh K. A., Pathak L. C., & Roy S. K. (2007). Effect of citric acid on the synthesis of nano-crystalline yttria stabilized zirconia powders by nitrate–citrate process. *Ceramics International*, 33, 1463–1468.

Siva Kumar V., Kelekanjeri G., Carter W. B. & Hampikian J. M. (2006). Deposition of α-alumina via combustion chemical vapor deposition. *Thin Solid Films,* 515, 1905.

Skakle J. M. S. (1998). Crystal chemical substitutions and doping of $YBa_2Cu_3O_x$ and related superconductors. *Materials Science and Engineering*, R23, 1-40.

Takao Y., Awano M., & Takagi H. (1999). Synthesis of $YBa_2Cu_3O_{7-x}$ composite superconductor by the spray drying method. *Journal of Materials Research,* 7, 2942-2947.

Tarascon J. M. & Bagley B. G. (1989). Oxygen stoichiometry and the high Tc superconducting oxides. *Materials Research Society Bulletin*, 14, 53-57.

Tinkham M. (1957). Penetration depth, susceptibility, and nuclear magnetic resonance in finely devided superconductors. *Physical Review*, 110, 26-29.

Tokumoto M., Ihara H., Matsubara T., Hirabayashi M., Terada N., Oyanagi H., Murata K., & Kimura Y. (1987). *Japan Journal of Applied Physics*, 26, 1565.

Toniolo J. C., Lima M. D., Takimi A. S & Bergmann C. P. (2005). *Materials Research Bulletin,* 40, 561.

Vipulanandan, & Li F. (2003). Production and Characterization of YBCO Nanoparticles. *IEEE Transactions on Applied Superconductivity*, 13, 2.

Wang X. & Lu G. (2005). Preparation of high thermal-stabile alumina by reverse microemulsion method. *Material Chemistry and Physics*, 90, 225.

Wu L, & Chu P. (1987). Superconductivity at 93 K in a new mixed-phase Y-Ba-Cu-O compound system at ambient pressure. *Physical Review Letters*, 908–910.

Xu X. L., Guo J. D., Wang Y. Z., & A. Sozzi. (2002). Synthesis of nanoscale superconducting YBCO by a novel technique. *Physica C: Superconductivity and its applications*, 371, 129-132.

Yana Q. Z., Sua X. T., Huang Z. Y., & Gea C. C. (2006). Sol–gel auto-igniting synthesis and structural property of cerium-doped titanium dioxide nanosized powders. *Journal of the European Ceramic Society*, 26, 915–921.

Yeoh L.M., & Shukor R.A. (2008). The study on various wet chemistry technique on $YBa_2Cu_3O_{7-\delta}$ superconducting oxides powder preparation. *Journal of Non-Crystalline Solid*, 354, 4043-4048.

Zhang J. L., & Evetts J. E. (1993). Zirconium doping of $YBa_2Cu_3O_{7-d}$ ceramic superconductor. *Chinese Journal of Physics*, 31, 6-11.

Zhang J., Liu F., Cheng G., Liu J., Cao S., & Liu Z. (1995). Electron structure and vacancy properties and Al-substitution dependence of the positron lifetime in Y 1: 2: 3 superconducting ceramics. *Physica Letter A*, 201, 70-76.

Zhou L., Chen S. K., Wang K. G., Wu X. Z., Zhang P. X., Feng Y., Wen H. H., & Li S. L. (2002). Preparation of enhanced Jc YBCO bulks by powder melting process with a combination of submicron 211 precursor and Pt addition. *Physica C: Superconductivity and its applications*, 371, 62-68.

Zou X. W., & Zhang H. (2000). Improved J_c properties of Na-doped MTG YBCO. *Materials Letters*, 42, 171–174.

LIST OF PUBLICATIONS

Academic Journals

1. **Mohd Shahadan Mohd Suan**, Mohd Rafie Johan, Tat Chua Siang (2012). Synthesis of $Y_3Ba_5Cu_8O_{18}$ superconductor powder by auto-combustion reaction: Effects of citrate–nitrate ratio, Physica C 480 (2012) 75–78.

2. **Mohd Shahadan Mohd Suan**, Mohd Rafie Johan (2013). Synthesis of Al_2O_3 nanoparticles highly distributed in $YBa_2Cu_3O_7$ superconductor by citrate–nitrate auto-combustion reaction, Physica C 492, 49–54.

3. **Mohd Shahadan Mohd Suan**, Mohd Rafie Johan (2014). Microhardness of Al_2O_3 nanoparticles added $YBa_2Cu_3O_7$ superconductor prepared using auto-combustion reaction, Materials Research Innovations.

Conference Proceedings

1. **Mohd Shahadan Mohd Suan**, Nor Liza Hawari, Mohd Rafie Johan (2011) Effects of Al_2O_3 Nanoparticles on YBCO Superconductor Prepared Using Pyrophoric Reaction, IEEE International Conference on Applied Superconductivity and Electromagnetic Devices, Sydney Australia.

2. Nor Liza Hawari, **Mohd Shahadan Mohd Suan**, Mohd Rafie Johan (2011) Structural and Morphological Studies of YBCO Doped with α-CNTs. Proceedings of 2011 IEEE International Conference Applied Superconductivity and Electromagnetic Devices, Sydney, Australia.

3. **Mohd Shahadan Mohd Suan**, Mohd Rafie Johan (2013) Microhardness of Al_2O_3 nanoparticles added $YBa_2Cu_3O_7$ superconductor prepared using auto-combustion reaction. Proceedings of International Conference on Science and Engineering of Materials, Kuala Lumpur, Malaysia.

Conference Presentations

1. Effects of Al_2O_3 Nanoparticles on YBCO Superconductor Prepared Using Pyrophoric Reaction, IEEE International Conference on Applied Superconductivity and Electromagnetic Devices, Sydney Australia.

2. Microhardness of Al_2O_3 nanoparticles added $YBa_2Cu_3O_7$ superconductor prepared using auto-combustion reaction. Proceedings of International Conference on Science and Engineering of Materials, Kuala Lumpur, Malaysia.

APPENDIX A1 – REFINED XRD PATTERNS (**x_{mol}** = 0.00 and 0.02)

Refined XRD patterns of samples with x_{mol} = 0.00 used in Figure 5.7:

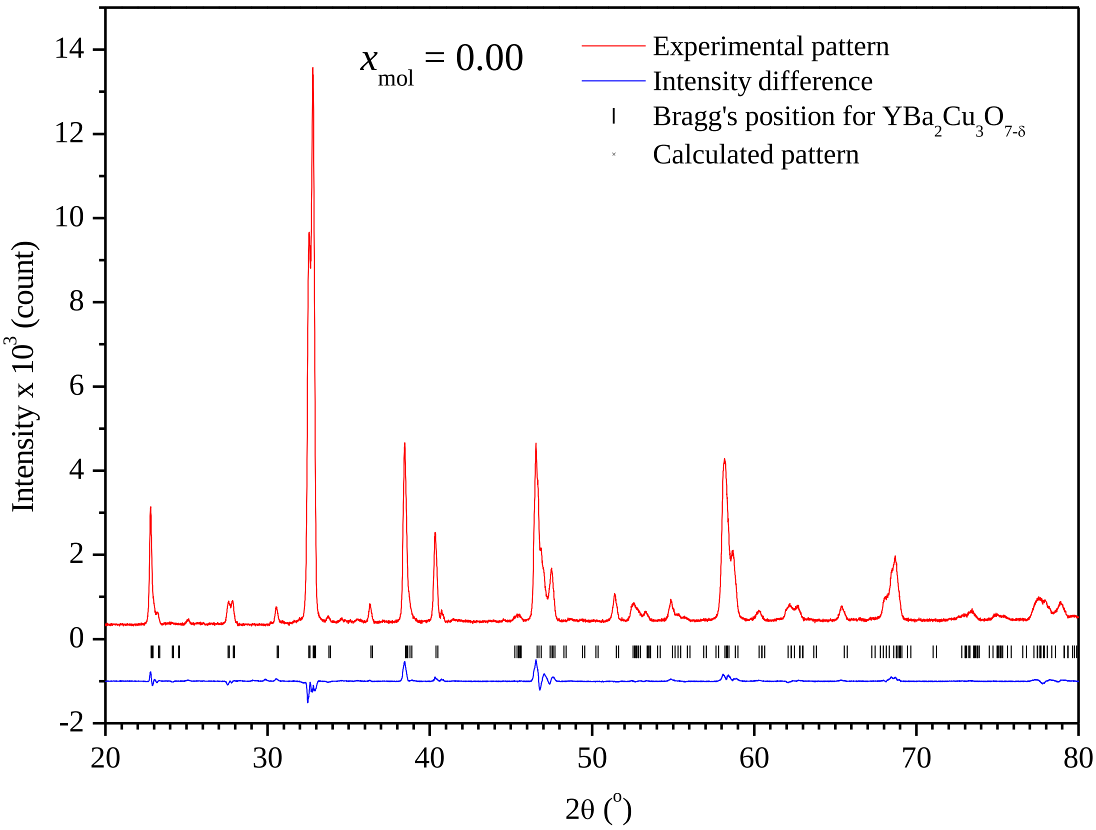

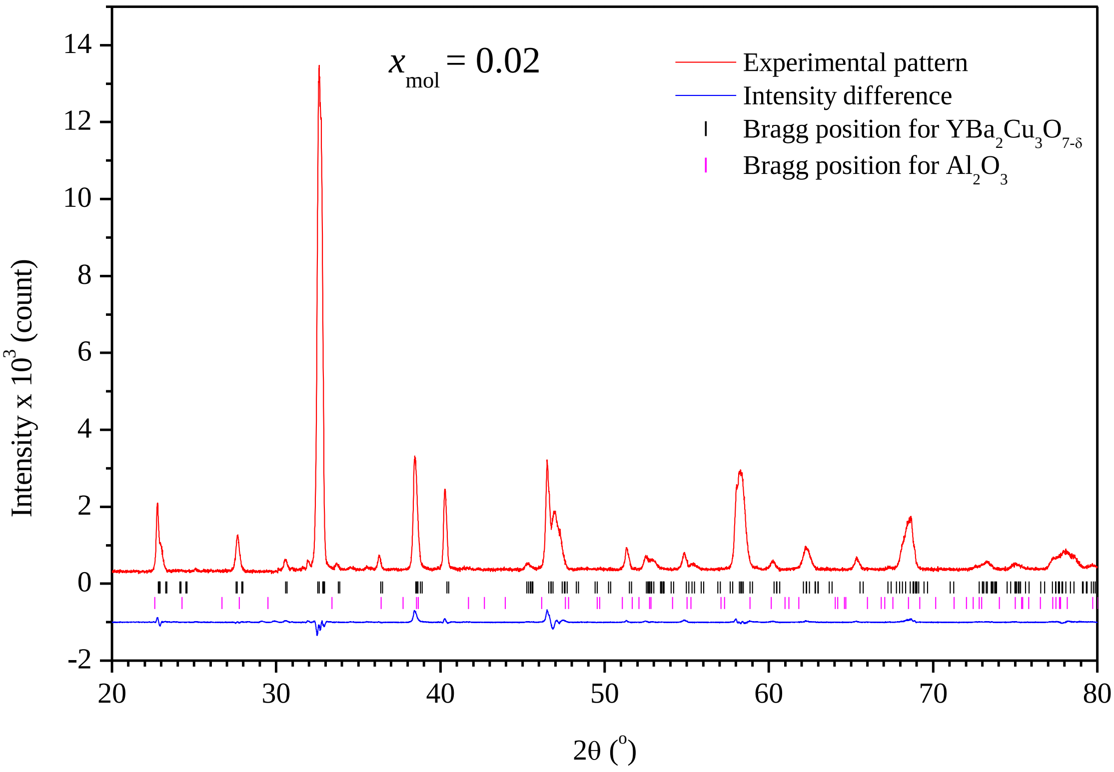

APPENDIX A2 – REFINED XRD PATTERNS (x_{mol} = 0.04 and 0.06)

Refined XRD patterns of samples with x_{mol} = 0.00 used in Figure 5.7:

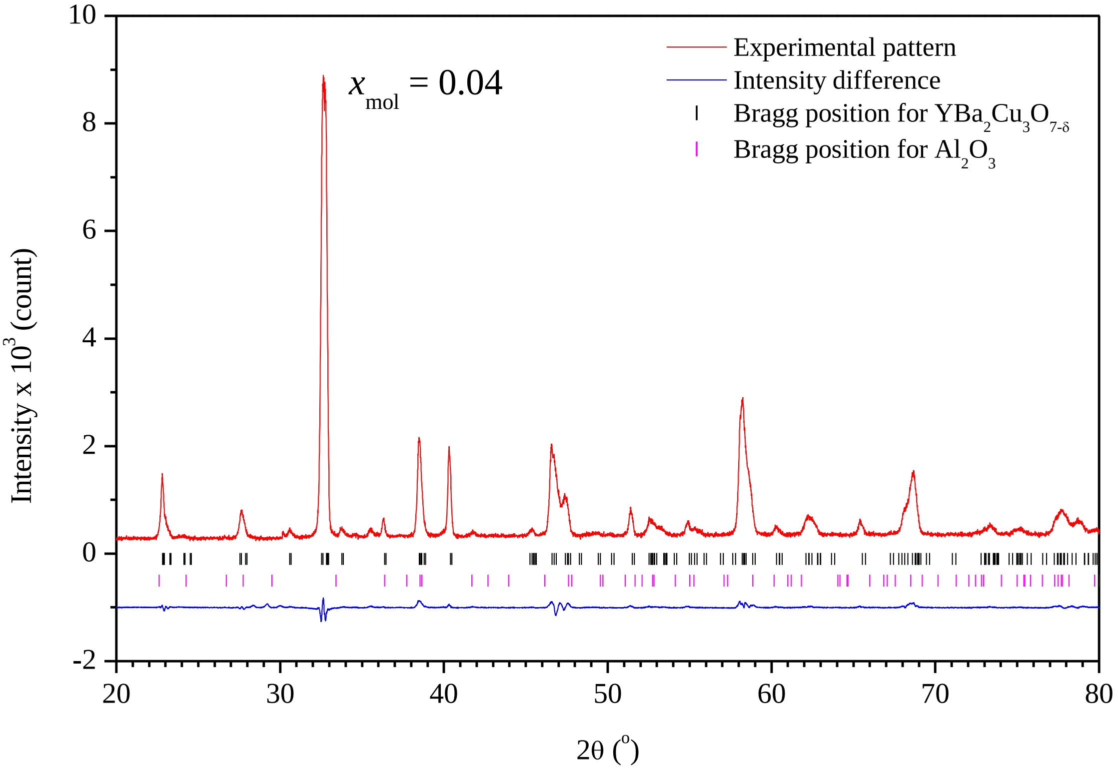

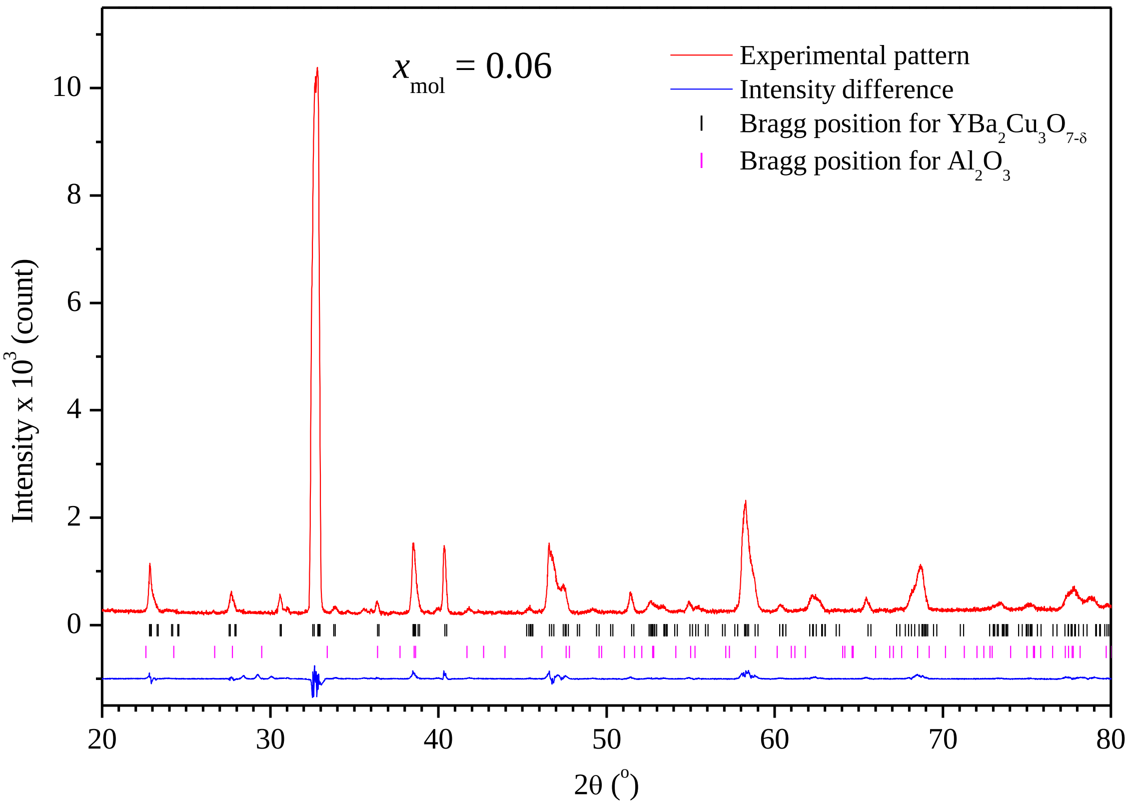

APPENDIX A3 – REFINED XRD PATTERNS (x_{mol} = 0.04 and 0.06)

Refined XRD patterns of samples with x_{mol} = 0.00 used in Figure 5.7: